Check for updates

JGR Solid Earth

RESEARCH ARTICLE
10.1029/2024JB030213

Alteration's Control on Frictional Behavior and the Depth of the Ductile Shear Zone in Geothermal Reservoirs in Volcanic Arcs

Barnaby Fryer[1], Florian Jermann[1,2], Patricia Patrier[3], Bruno Lanson[4], Stanislav Jelavic[4], Gabriel Meyer[1], Stephen E. Grasby[5], and Marie Violay[1]

[1]Laboratory of Experimental Rock Mechanics, École Polytechnique Fédérale de Lausanne, Lausanne, Switzerland, [2]Currently Affiliated With BTG Büro für Technische Geologie AG, Sargans, Switzerland, [3]Département Géosciences, Université de Poitiers, Poitiers, France, [4]University Grenoble Alpes, USMB, CNRS, IRD, UGE, ISTerre, Grenoble, France, [5]Geological Survey of Canada, Calgary, AB, Canada

Key Points:

- Collective phyllosilicate content controls the first-order friction behavior of andesitic samples from geothermal fields in volcanic arcs
- Negative frictional healing is observed and thought to be related to the presence of expandable clays
- The transition to a ductile shear zone in volcanic-arc settings is influenced by alteration's control on frictional strength

Supporting Information:

Supporting Information may be found in the online version of this article.

Correspondence to:

B. Fryer,
barnaby.fryer@geoazur.unice.fr

Citation:

Fryer, B., Jermann, F., Patrier, P., Lanson, B., Jelavic, S., Meyer, G., et al. (2025). Alteration's control on frictional behavior and the depth of the ductile shear zone in geothermal reservoirs in volcanic arcs. *Journal of Geophysical Research: Solid Earth*, *130*, e2024JB030213. https://doi.org/10.1029/2024JB030213

Received 23 AUG 2024
Accepted 16 JAN 2025

Author Contributions:

Conceptualization: Barnaby Fryer, Gabriel Meyer, Marie Violay
Data curation: Barnaby Fryer, Florian Jermann
Formal analysis: Barnaby Fryer, Florian Jermann, Patricia Patrier, Bruno Lanson, Stanislav Jelavic
Funding acquisition: Marie Violay
Investigation: Barnaby Fryer, Florian Jermann, Patricia Patrier, Bruno Lanson, Stanislav Jelavic, Gabriel Meyer, Stephen E. Grasby, Marie Violay
Methodology: Barnaby Fryer
Project administration: Marie Violay
Resources: Patricia Patrier, Stephen E. Grasby, Marie Violay

© 2025. The Author(s).
This is an open access article under the terms of the Creative Commons Attribution License, which permits use, distribution and reproduction in any medium, provided the original work is properly cited.

Abstract The majority of geothermal energy is produced in tectonically active volcanic-arc regions due to their high geothermal gradients. Reservoirs in these settings are often stratified with smectite/kaolinite-, illite-, and chlorite-rich zones, in order of increasing depth and temperature. Eighteen andesitic core and surface samples were taken from five geothermal fields in the Lesser-Antilles and Cascade volcanic arcs. The collected samples have experienced various degrees of alteration and can be considered, in their ensemble, to be representative of the previously mentioned alteration zones. The influence of the alteration was assessed through biaxial rate-and-state friction experiments on prepared gouge. The samples were each tested at 10, 30, and 50 MPa normal stress in both nominally dry and nominally wet conditions. While significant water-induced frictional-strength reduction was observed, phyllosilicate content dominates frictional behavior, with increased phyllosilicate content reducing frictional strength, promoting velocity-strengthening behavior, and reducing frictional healing. Negative frictional healing is observed and likely related to the presence of expandable clays, leading to frictional weakness over long time periods. It is suggested that, by controlling frictional strength, phyllosilicate content influences the depth of onset of ductile shear zones, which often underlie these reservoirs and are critical for the horizontal advection and vertical sealing of geothermal fluid. Further, as these types of reservoirs are likely critically stressed, varying degrees of alteration within different reservoir zones can give rise to the formation of stress jumps. Overall, the frictional behavior depended to a first order on overall phyllosilicate content, potentially simplifying engineering studies.

Plain Language Summary Altered andesitic core and surface samples were taken from five geothermal fields in volcanic arc environments. The alteration has resulted in the formation of clay-like (phyllosilicate) minerals. Through a large number of friction experiments, it is shown that the amount of clay-like minerals controls frictional properties, irrespective of the specific clay-like minerals present, potentially simplifying induced seismicity studies if all clay-like minerals might be treated frictionally as one species. Increased clay-like mineral content decreases frictional strength (making faults weaker), promotes stable sliding (meaning faults are unlikely to nucleate an earthquake), and reduces frictional healing (meaning faults recover strength slowly). The unusual phenomenon of fault weakening during seismic stasis (negative frictional healing) is also occasionally observed and linked to clay-like minerals. Further, reservoirs in these settings are often rooted in distributed (ductile) shear zones which facilitate horizontal fluid movement. It is suggested that the extent to which clay-like minerals have formed will influence the depth at which this distributed shear zone begins. Finally, it is suggested that the reduced frictional strength of clay-like-mineral-rich zones may lead to the formation of sharp stress changes between highly and un-altered zones, indicating a strong control of alteration on fracture propagation.

1. Introduction

As geothermal energy production greatly benefits from a high geothermal gradient, the preponderance of global geothermal electricity production is located near tectonically active volcanic- or, equivalently, magmatic-arc regions (Stelling et al., 2016). Some examples include Cerro Pabellón, Chile (Maza et al., 2018), Tolhuaca Geothermal Field, Chile (Melosh et al., 2010), the Awibengkok Geothermal System, Indonesia (Stimac et al., 2008), Darajat, Indonesia (Rejeki et al., 2010), the Ogiri Field, Japan (Goko, 2000), the Copahue

Software: Barnaby Fryer, Florian Jermann
Supervision: Barnaby Fryer, Gabriel Meyer, Marie Violay
Validation: Barnaby Fryer
Visualization: Barnaby Fryer
Writing – original draft: Barnaby Fryer
Writing – review & editing: Barnaby Fryer, Florian Jermann, Patricia Patrier, Bruno Lanson, Stanislav Jelavic, Gabriel Meyer, Stephen E. Grasby, Marie Violay

Geothermal Reservoir, Argentina-Chile (Barcelona et al., 2019), Los Azufres, Mexico (Cathelineau & Izquierdo, 1988), Bouillante, France (Jaud & Lamethe, 1985), Newberry, USA (MacLeod & Sammel, 1982), and Mount Meager, Canada (Jessop, 2008). These systems located in volcanic- or, in many cases, specifically andesitic-arcs represent a significant proportion of global geothermal energy production (Stelling et al., 2016).

However, our understanding of the structure, fluid pathways, and history of these reservoirs is generally poor (e.g., Bouchot et al. (2010), Favier, Lardeaux, Corsini, et al. (2021)). Secondary permeability is thought to be a key factor in the productive potential of such geothermal systems (Stelling et al., 2016) and is often governed by fractures and faults in these contexts (Curewitz & Karson, 1997; Favier, Lardeaux, Corsini, et al., 2021; Goko, 2000; Jolie et al., 2021; Navelot et al., 2018; Stimac et al., 2008). The fluids that flow through these discontinuities often cause the hydrothermal alteration of the surrounding rock due to chemical disequilibrium (Browne, 1978; Fenner, 1934; Frolova et al., 2014). As alteration, while dependent on fluid-to-rock (F/R) mass ratio and the degree of disequilibrium, is strongly dependent on temperature, which often varies directly with depth, it is not uncommon for alteration to occur in temperature-delimited zones, albeit with this zonation often appearing during the cooling of the system. For example, smectite and kaolinite form at relatively low temperatures and therefore generally form a shallow alteration zone, at times overprinting previous high-temperature alteration (e.g., Patrier et al. (1997)). Below this, at slightly higher temperatures an illite-rich or mixed-layer zone may have previously formed. Deeper still, at again higher temperatures, a chlorite-rich alteration zone may be present. The combination of these three zones leads to a typical geothermal reservoir structure with a smectite/kaolinite zone overlying an illite-rich zone, which in turn overlies a chlorite-rich zone (e.g., Cathelineau and Izquierdo (1988), Mas et al. (2006), Sillitoe (2010), Stimac et al. (2015)). Of course, many other alteration products will likely form in such reservoirs and the zones themselves may not be marked by sharp boundaries such that transitions are common. Note, additionally, that it is common to find strong lateral variations of temperature and alteration facies in these contexts. At any rate, alteration and the formation of secondary minerals can significantly impact the permeability and porosity of fluid pathways and may lead, for example, to the zone rich in smectite and kaolinite forming a clay cap, preventing the loss of heated fluids to the surface through advection (Frolova et al., 2010, 2014; Navelot et al., 2018; Wyering et al., 2014).

Frictional sliding can result in such phenomena as cataclasis and gouge formation, dilation, and cracking; all of which can have meaningful implications for fluid flow. Additionally, considering the high geothermal gradient present in most geothermal fields, the transition in mode and mechanism of deformation can be anomalously shallow in these regions (Cameli et al., 1993; Lucchitta, 1990; Ranalli & Rybach, 2005). The ”ductile” shear zones of distributed deformation at the base of many geothermal fields (e.g., Stimac et al. (2015), Yagupsky et al. (2023)) may serve as a foundation for the sub-vertically-oriented faults within the reservoir, and act as zones providing horizontal fluid transport (Favier et al., 2019; Favier, Lardeaux, Corsini, et al., 2021; Knipe & McCaig, 1994; Kohlstedt et al., 1995; Verati et al., 2018), while acting as vertical seals (Stimac et al., 2015), Figure 1. The depth of this zone will depend, in part, on the frictional strength of the rock (Byerlee, 1968; Griggs, 1936; Kohlstedt et al., 1995; Meyer et al., 2019; Meyer & Violay, 2023; Paterson, 1958; Ranalli & Rybach, 2005; Violay et al., 2012). Therefore, an understanding of how the frictional behavior of these rocks may change and develop in these settings throughout the life of the system is important for reconstructing the entire history of the reservoir, which can in turn improve the exploration process within that specific field, in particular as these fields have a tendency to migrate and often have non-monotonic temperature profiles, resulting in potentially hidden high-temperature zones (e.g., Mas et al. (2003, 2006)). It is further crucial to understand how these faults control the state of stress of the field and how they respond to engineering operations influencing stress and pore pressure conditions.

Further, geothermal projects have often been burdened by instances of induced seismicity. For example, induced seismic events in Basel, Switzerland (Häring et al., 2008), St. Gallen, Switzerland (Obermann et al., 2015), Darajat Geothermal Field, Indonesia (Pramono & Colombo, 2005), Soultz-sous-Forêts, France (Dorbath et al., 2009), and Pohang, South Korea (Kim et al., 2018) have in some cases led to significant project difficulties. Therefore, an understanding of the frictional properties of rocks is relevant to prevent unwanted seismicity and better understand how a reservoir responds to shear stimulation, a stimulation technique often applied to Enhanced Geothermal Systems. This is particularly true in the case of volcanic arcs, where seismicity may at times be capable of inducing debris avalanches (Keefer, 1984; Siebert, 1984) or threatening the integrity of the clay cap (Yamaya et al., 2013).

21699356, 2025, 2, Downloaded from https://agupubs.onlinelibrary.wiley.com/doi/10.1029/2024JB030213 by Cochrane France, Wiley Online Library on [28/01/2025]. See the Terms and Conditions (https://onlinelibrary.wiley.com/terms-and-conditions) on Wiley Online Library for rules of use; OA articles are governed by the applicable Creative Commons License

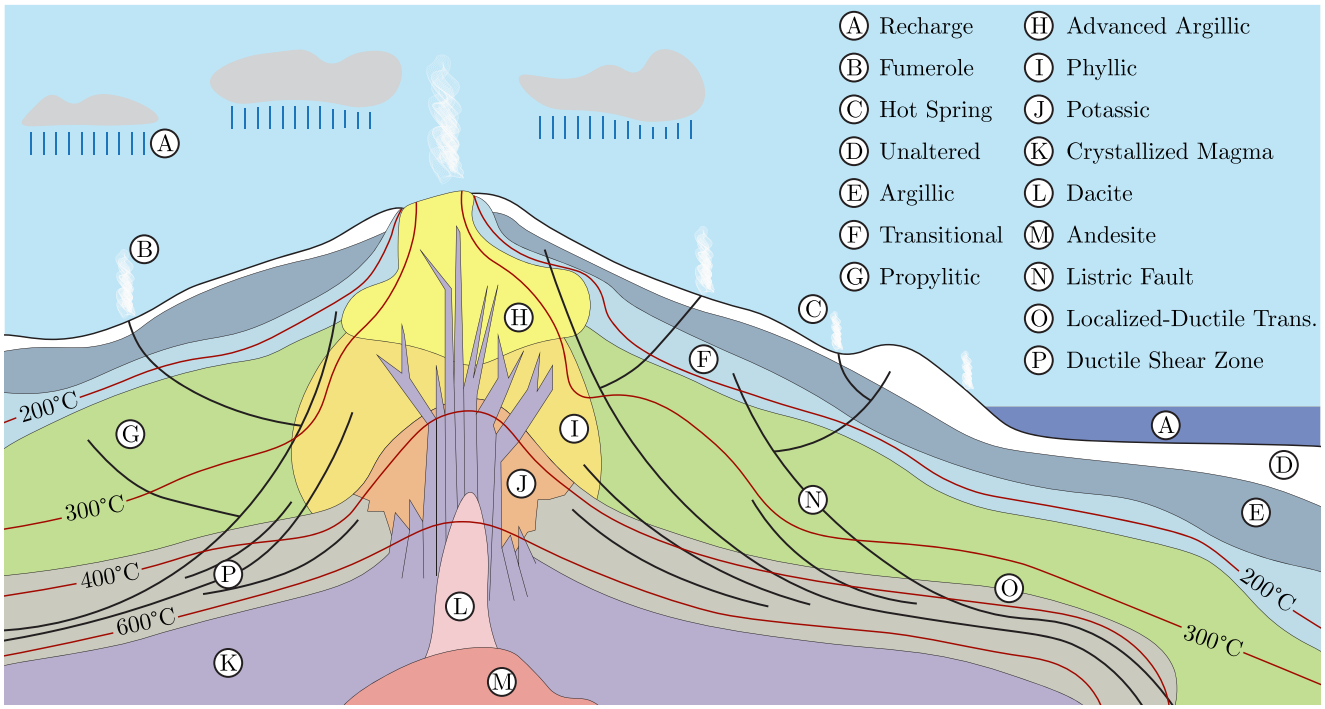

Figure 1. A representative example of a volcanic arc system, based on Richards (2011), Stimac et al. (2015), Revil and Gresse (2021). The argillic zone (E) may contain smectite, kaolinite, and/or illite, may overprint higher-temperature alteration, and may act as a clay cap. Propylitic alteration (G) may produce chlorite. Due to a high geothermal gradient, the onset of ductile deformation (i.e., the Localized-to-Ductile Transition) is found at a relatively shallow depth (O) and leads to the formation of a ductile shear zone (P). This zone is comprised of laterally extensive fractures that connect to listric-like faults and allows for the lateral transfer of fluids, while acting as a vertical seal. As depth and temperature increase, deformation mechanisms shift from brittle to plastic. The onset of this second transition may occur within the ductile shear zone or outside of it. Note that the original in situ rocks may be many different types of volcanic rock (e.g., tuff, ash, lava, etc.) depending on the deposition history of the region. The schematic is not to scale.

Here, 18 samples (15 core samples and 3 surface samples) are collected from two volcanic arcs relevant for geothermal energy exploration and exploitation: the Lesser Antilles and Cascade volcanic arcs. The samples are generally andesitic in nature and have undergone a wide range of alteration. A general overview of the samples is provided in Table 1. Gouges are prepared from the samples and their frictional behaviors are tested in a biaxial apparatus in the rate-and-state friction framework (Dieterich, 1979; Ruina, 1983). It is found that alteration has the potential to significantly influence the friction coefficient, velocity-dependence, and inter-seismic healing of this rock type, having consequences in these settings for geothermal-reservoir-history reconstruction and fluid flow (because friction coefficient is related to the depth of onset of any ductile shear zone), in situ stresses (because the stress state is influenced by the friction coefficients along critically stressed faults), and induced seismicity (because friction coefficient, velocity dependence, and healing all influence the seismic response of faults).

2. Sample Sourcing

2.1. The Lesser Antilles Volcanic Arc

The Lesser Antilles form an island volcanic arc and are a result of the subduction of the North and South American plates underneath the Caribbean Plate at approximately 20 mm per year (DeMets et al., 2010; Deng & Sykes, 1995). The Lesser Antilles are home to a number of active volcanoes, Figure 2a, and are considered to have geothermal-energy production potential. Despite this, geothermal energy production is currently only operative in Guadeloupe, in the Bouillante geothermal field. Other islands, such as Martinique, have seen the drilling of a number of exploratory wells. Cores from these wells and surface samples from Guadeloupe will be used in this study as representative of the potential geothermal systems of the Lesser Antilles.

Terre-de-Haut, an island belonging to the Guadeloupe Archipelago, Figure A1, is primarily composed of andesitic rocks (Jacques & Maury, 1988), a typical composition for the recently active arc in the Lesser Antilles

21699356, 2025, 2, Downloaded from https://agupubs.onlinelibrary.wiley.com/doi/10.1029/2024JB030213 by Cochrane France, Wiley Online Library on [28/01/2025]. See the Terms and Conditions (https://onlinelibrary.wiley.com/terms-and-conditions) on Wiley Online Library for rules of use; OA articles are governed by the applicable Creative Commons License

21699356, 2025, 2, Downloaded from https://agupubs.onlinelibrary.wiley.com/doi/10.1029/2024JB030213 by Cochrane France, Wiley Online Library on [28/01/2025]. See the Terms and Conditions (https://onlinelibrary.wiley.com/terms-and-conditions) on Wiley Online Library for rules of use; OA articles are governed by the applicable Creative Commons License

Table 1
A Summary of the Samples Used for This Study

Sample	Location (well name)	Rock type	Depth [m]	T [°C]	Pred. Alt. Type	Phyll. [%]
B494D	Les Saintes (surface)	Ba/An-Dac	-	-	Smectite	23
S491I	Les Saintes (surface)	Ba/An-Dac	-	-	Smectite	29
S491B	Les Saintes (surface)	Ba/An-Dac	-	-	Illite	49
LA02422	Lamentin (LA02)	An	442.0	49	Intermediate	51
LA02541	Lamentin (LA02)	An	541.6	47	Intermediate	44
LA02767	Lamentin (LA02)	An	767.8	47[b]	Chlorite	10
LA03749	Lamentin (LA03)	An[a]	749.8	77	Al-smectite/Kaolinite	62
LA03758	Lamentin (LA03)	An	758.2	77	Intermediate	19
M1430	Mount Meager (M-17)	Diorite	≈435	167	Intermediate	21
G2658	Summerland Basin (GSC495)	TrAn	810.3	37	Mg-smectite	15
G2690	Summerland Basin (GSC495)	TrAn	819.9	37	Chlorite	17
G3005	Summerland Basin (GSC495)	TrAn	915.9	40	Chlorite	15
G3130	Summerland Basin (GSC495)	TrAn	954.0	41	Chlorite	20
N3583	Newberry (GEO N-2)	Ba-Ba/An	1,092.3	134	Mg-smectite	24
N3808	Newberry (GEO N-2)	Ba-Ba/An	1,160.7	143	Mg-smectite	22
N4330	Newberry (GEO N-2)	Ba-Ba/An	1,319.8	163	Mg-smectite	15
N4343	Newberry (GEO N-2)	Ba-Ba/An	1,323.7	164	Intermediate	20
N4422	Newberry (GEO N-2)	Ba-Ba/An	1,348.0	166[c]	Mg-smectite	18

Note. The rock types are taken from Verati et al. (2016), Favier, Lardeaux, Corsini, et al. (2021) for Les Saintes and Mas et al. (2003) for Lamentin; otherwise they are unpublished. Ba is basalt, An is andesite, Dac is dacite, and TrAn is trachyandesite. Depths are measured depths. The temperature, T, data are taken from Mas et al. (2003) for Lamentin wells, Ghomshei et al. (2004) for Mount Meager, Jessop (2008) for Summerland Basin (based on a linear interpolation of temperature measurements taken at 706 and 946.5 m depth), and Walkey and Swanberg (1990) for Newberry. Note that these are the modern temperatures for these reservoirs. The predominant alteration type (Pred. Alt. Type) and phyllosilicate content by weight (Phyll.) are given in the last two columns and are based on XRD results (shown in more detail later, see Section 5.1.2), with predominant alteration type noting the principal category of secondary phyllosilicate mineral present. Intermediate means that no one phyllosilicate mineral is responsible for more than 67% of the phyllosilicate minerals present. [a]This sample is heavily altered and from a fault zone. The original rock type cannot be stated with certainty. See Genter et al. (2002). [b]The last depth for which temperature was recorded for this well was 724 m. [c]The last depth for which temperature was recorded for this well was 1,346 m.

(Navelot et al., 2018). As with the current Bouillante system, the paleo-geothermal system in the central part of Terre-de-Haut is associated with the intersection of two major fault systems (Verati et al., 2016). As surface samples from Les Saintes can be considered as analogs to in situ Bouillante geothermal reservoir rock (Favier, Lardeaux, Verati, et al., 2021; Navelot et al., 2018; Verati et al., 2016), three such samples were used for this study, taken from the center of Terre-de-Haut, near Grande Anse, which is comprised of highly altered andesite (Jacques & Maury, 1988; Navelot et al., 2018). Note that, due to this alteration, it is difficult to know if these samples were originally lavas, debris, or pyroclastic flows (Favier, Lardeaux, Corsini, et al., 2021; Jacques & Maury, 1988); however, lavas sampled in this region are generally in the basalt-andesite to dacite range (Favier, Lardeaux, Corsini, et al., 2021; Verati et al., 2016). These samples will be referred to as S491B, S491I, and B494D.

Located on the center-west side of Martinique, the Plain of Lamentin is an alluvial plain surrounded by older volcanic highlands and lain down on a volcanic substratum (Gadalia et al., 2014; Mas et al., 2003), Figure A2. The reservoir of Lamentin is cut by large, widespread, and often steeping-dipping normal faults (Gadalia et al., 2014; Genter et al., 2002). These faults are thought to be the conduits through which mantle-derived gases reach the Lamentin reservoir and even the surface (Gadalia et al., 2019). It is not uncommon to find alteration minerals such as kaolinite, chlorite, and calcite within cores taken from zones transected by faults (Genter et al., 2002). On the basis of clay-mineral signatures and α-spectrometry, it is thought that the system presented temperatures greater

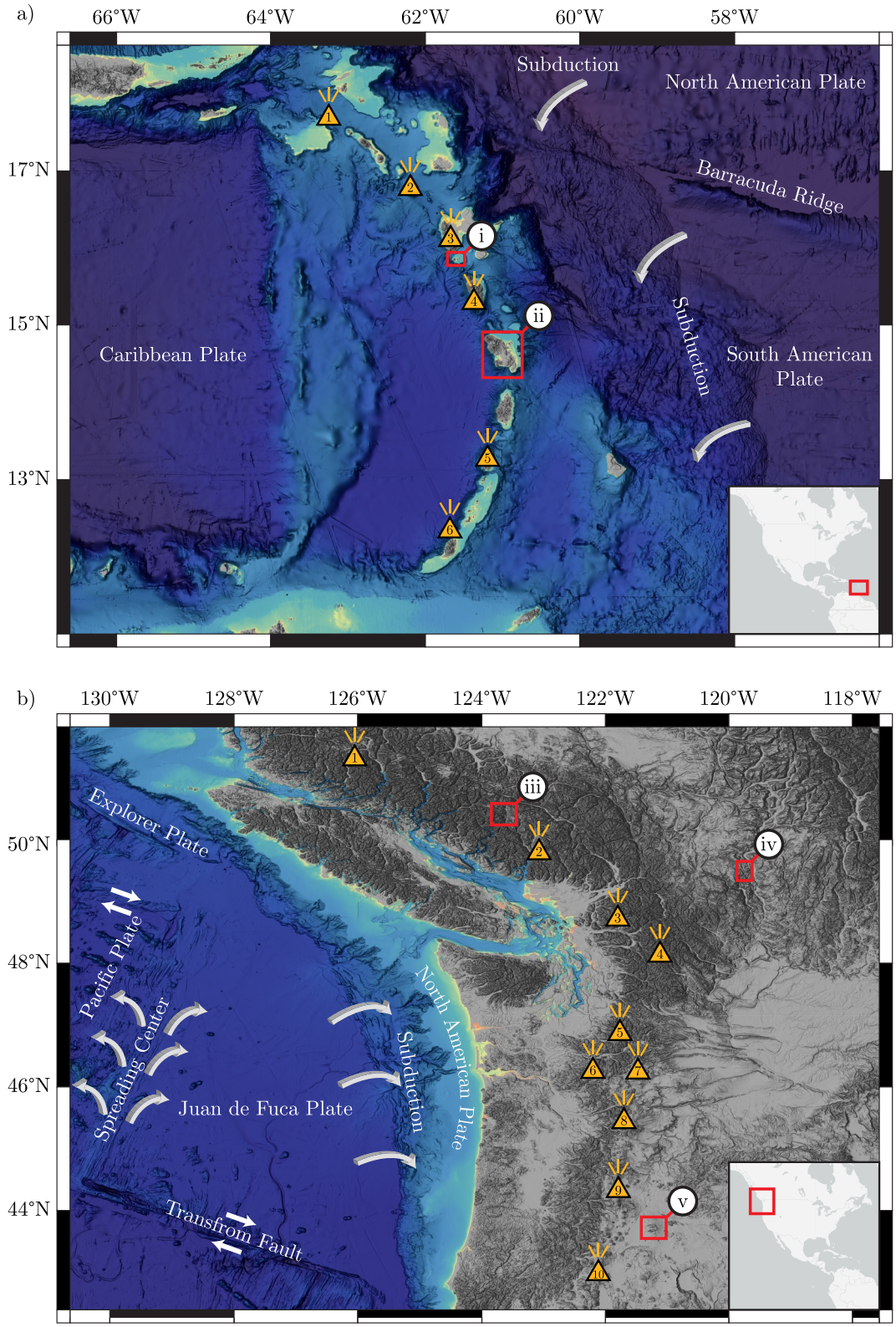

Figure 2.

21699356, 2025, 2, Downloaded from https://agupubs.onlinelibrary.wiley.com/doi/10.1029/2024JB030213 by Cochrane France, Wiley Online Library on [28/01/2025]. See the Terms and Conditions (https://onlinelibrary.wiley.com/terms-and-conditions) on Wiley Online Library for rules of use; OA articles are governed by the applicable Creative Commons License

21699356, 2025, 2, Downloaded from https://agupubs.onlinelibrary.wiley.com/doi/10.1029/2024JB030213 by Cochrane France, Wiley Online Library on [28/01/2025]. See the Terms and Conditions (https://onlinelibrary.wiley.com/terms-and-conditions) on Wiley Online Library for rules of use; OA articles are governed by the applicable Creative Commons License

than 200°C as recently as 250,000 years ago (Gadalia et al., 2019; Mas et al., 2003). It currently presents much more moderate temperatures, less than 100°C. In this study, the cores from the LA02 (Carrère) well were taken from 422, 541.55, and 767.8 m and will be referred to as LA02422, LA02541, and LA02767, respectively. Further, two cores from the LA03 (Californie) well are studied here from depths of 749.8 and 758.2 m and will be referred to as LA03749 and LA03758, respectively. Both of these cores are from moderately to slightly fractured zones with calcite fillings (Genter et al., 2002). Further information on the field histories of Lamentin and Les Saintes can be found in Appendices A1 and A2. Sample photos can be found in Supplementary Material, Figures S1-S2 in Supporting Information S1.

2.2. The Cascade Volcanic Arc

The Cascade Volcanic Arc is located in the Northwestern United States and Southwestern Canada. This continental volcanic arc is related to the spreading of the Juan de Fuca Ridge and the subduction of the Juan de Fuca Plate under the North American Plate (Jessop, 2008). The Cascade Volcanic Arc is home to a number of active volcanoes, Figure 2b, and is considered to have significant geothermal-energy production potential. In particular, Mount Meager in Canada and the Newberry Volcano EGS Demonstration Project are thought to represent promising candidates for geothermal energy production, and both have been drilled and cored. Further exploration has also occurred farther inland in the Summerland Basin, but this resource is likely low enthalpy.

Mount Meager is a volcanic complex located in southwest British Colombia in the Garibaldi Volcanic Belt, Figure A3. For this study, a core sample of diorite was taken from well M-17, drilled across the southern flank of Pylon Peak (Jessop, 2008), in the interval from 433.4 to 437.1 m (1,422 ft–1,434 ft). This sample will be referred to as M1430.

The Summerland Basin is an Eocene volcanic caldera located in the Okanagan Valley of British Columbia, Figure A4, and has been interpreted to be composed of accreted oceanic and island arcs as part of the Intermontane Belt of the Canadian Cordillera (Church et al., 1990; Monger & Irving, 1980). The Summerland Basin comprises several major units; of particular importance here are the massive volcanic beds of the Marron Formation, principally comprised of alternating ash and lava flows which are largely continuous despite being offset by faulting (Jessop, 2008; Michel et al., 2002). For the study being performed here, samples were taken from 810.3 m (2,658.5 ft), 819.9 m (2,690 ft), 915.9 m (3,005 ft), and 954.0 m (3,130 ft). These samples will be referred to as G2658, G2690, G3005, and G3130, with the numerical portion of the name corresponding to the sample depth in feet. All four samples are part of the Marron Formation's Kitley Lake Member, which is predominantly composed of chloritized amygdaloidal porphyritic trachyandesite. While G2658 is considered to be fairly fresh trachyandesite, the rest of these samples have undergone alteration. G2690 displays pink oxidation, whereas G3005 has undergone carbonate-rich alteration and is light green in color. G3130 is dark green and is chloritic clay rich.

The Newberry Volcano, Figure A5, is located 60 km east of the Cascade range in central Oregon, covers an area of 1,200 km^2, and has been active as recently as 1,300 years ago (MacLeod & Sammel, 1982; MacLeod & Sherrod, 1988). While the composition of its rocks varies widely at depth, it is thought that it is underlain by a rhyolitic magma chamber of approximately 5 km in diameter (MacLeod & Sherrod, 1988). Interest in this region is related in particular to an exploration well (USGS N-2) completed in 1981, where a temperature of 265°C was encountered at 932 m (MacLeod & Sammel, 1982). For the study being performed here, samples were taken from the GEO N-2 (not the USGS N-2) well at 1,092.3 m (3,583.5 ft), 1,160.7 m (3,808 ft), 1,319.8 m (4,330 ft),

Figure 2. The geodynamic contexts of the samples. Detailed geological maps are given in Appendix A. (a) A map of the Lesser Antilles Volcanic Arc. Sample sourcing locations are denoted by red boxes, with (i) corresponding to Les Saintes, and (ii) to Lamentin. The listed volcanoes, denoted by orange triangles, are all likely to have been active in the last 11,700 years (Holocene) (Global Volcanism Program, 2024), with the numbers corresponding to (1) Mount Scenery, (2) Soufrière Hills (Montserrat), (3) La Grande Soufrière, (4) Morne Plat Pays, (5) La Soufrière (Saint Vincent), and (6) Kick'em Jenny. These volcanoes are generally related to the subduction of the North and South American plates underneath the Caribbean Plate. (b) A map of the Cascade Volcanic Arc. Core samples are taken from locations denoted by the red boxes, with (iii) corresponding to Mount Meager, (iv) Summerland Basin, and (v) to Newberry. The listed volcanoes, denoted by orange triangles, are all likely to have been active in the last 11,700 years (Holocene) (Global Volcanism Program, 2024), with the numbers corresponding to (1) Silverthrone Caldera, (2) Mount Garibaldi, (3) Mount Baker, (4) Glacier Peak, (5) Mount Rainier, (6) Mount St. Helens, (7) Mount Adams, (8) Mount Hood, (9) the Three Sisters, (10) Crater Lake. These volcanoes are generally related to the subduction of the Juan de Fuca Plate underneath the North American Plate. Also shown is the spreading center between the Juan de Fuca and Pacific Plates (i.e., the Juan de Fuca Ridge). The ETOPO 2022 Global Relief Model is used as the base map (NOAA National Centers for Environmental Information, 2022).

21699356, 2025, 2, Downloaded from https://agupubs.onlinelibrary.wiley.com/doi/10.1029/2024JB030213 by Cochrane France, Wiley Online Library on [28/01/2025]. See the Terms and Conditions (https://onlinelibrary.wiley.com/terms-and-conditions) on Wiley Online Library for rules of use; OA articles are governed by the applicable Creative Commons License

1,323.7 m (4,343 ft), and 1,348.0 m (4,422.5 ft). These samples will be referred to as N3583, N3808, N4330, N4343, and N4422, with the numerical portion of the name corresponding to the sample depth in feet. These samples are basaltic to basaltic-andesitic in composition with varying degrees of alteration. Further information on the field histories of Mount Meager, Summerland Basin, and Newberry can be found in Appendices A3–A5. Sample photos can be found in Supplementary Material, Figures S3–S5 in Supporting Information S1.

3. Methods

3.1. Sample Preparation

The samples were first photographed and then cut into more manageable pieces. Two cut pieces of each sample were analyzed with X-ray Diffraction (XRD) and as thin sections. The remaining sample material was crushed by hand with first a hammer and then an agate mortar and pestle. Finally, the prepared gouge was passed through a sieve to ensure a particle size of less than 125 μm, later confirmed by granulometry, Table S6 in Supporting Information S1. The samples were never oven dried to avoid altering the clays present in the sample (Summers & Byerlee, 1977). One gram of each sample was ground with 15 ml of ethanol for 10 min using the McCrone mill equipped with agate grinding elements to ensure a nominal average particle size of 1 μm, important for the quantitative phase analysis.

3.2. Sample Characterization

3.2.1. Microstructure

Thin sections were prepared by Thin Section Lab and the Institute of Earth Sciences at the Université de Lausanne from virgin samples and then carbon coated and analyzed using scanning electron microscopes (SEMs) at the University of Poitiers (JEOL JSM IT500) and the Ecole Polytechnique Fédérale de Lausanne. These samples were viewed using back-scattered electrons, illustrating density contrasts. In addition, energy-dispersive X-ray spectrometry (EDX) was used to evaluate the mass percentages of elements present in different minerals in the samples. This was then used to calculate the structural formulas of the minerals, which, in conjunction with the density contrasts and particle morphology, led to mineral identification. Specifically, the SEM was equipped with a Bruker Lynxeye EDX spectrometer with a XFlash 4,030 Silicon drift detector. The analytical conditions for quantitative EDX analysis were as follows: acceleration voltage 15 kV, current beam 1 nA, counting time 50 s, working distance 11 mm. The standards used for the EDX quantitative analysis consisted of albite (Na, Al, Si), almandine (Mg, Fe), diopside (Ca), orthoclase (K) and spessartite (Mn). Matrix corrections were performed using the Phi-Rho-Z correction.

3.2.2. X-Ray Diffraction (XRD) and Quantitative Phase Analysis (QPA)

XRD data was collected on randomly oriented powders using a Bruker D8 Advance diffractometer operating in Bragg-Brentano geometry and using CoKα radiation (λ = 1.7902 Å; 40 kV–35 mA). Data was collected from 5-90° 2θ, counting 6s per 0.026° step. Following identification of the crystalline phases, sample mineralogy was assessed quantitatively with the Rietveld program BGMN and the Profex user-interface (Doebelin & Kleeberg, 2015). Clay minerals were grouped by families (kaolinite, micas, and swelling 2:1). Swelling 2:1 minerals include both discrete smectite and smectite-containing mixed layers (e.g., chlorite/smectite or corrensite). When both species coexist, XRD data was fit using smectite contributions with contrasting hydration states to reproduce the positions of basal reflections. The tri- or di-octahedral character of identified phyllosilicates was derived mainly from the position of (06,33) diffraction bands despite significant overlap with phases such as quartz. XRD analyses were guided by the chemical analyses performed with SEM/EDX, and vice versa. The quantity of amorphous material was determined by adding corundum as an internal standard. The difference between the amount of corundum added and refined was recalculated into the amorphous content.

3.3. Apparatus

Double-direct shear experiments (Dieterich, 1972) were performed in the HighSTEPS apparatus (Violay et al., 2021), Figure 3, a biaxial apparatus located at the Ecole Polytechnique Fédérale de Lausanne. The prepared gouge is placed in between one vertical and two horizontal sample holders, with 4.86 mm of gouge on either side, and is then compacted by hand with a steel block and a leveling jig. The surface of the horizontal sample holders

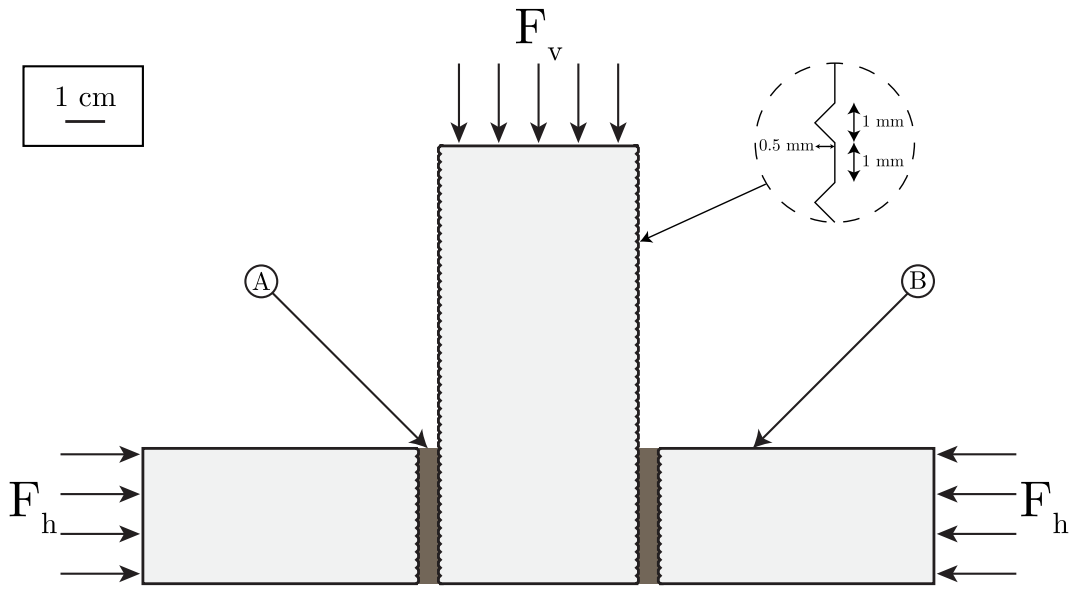

Figure 3. Side-on view of double-direct shear arrangement used during the investigation. (A) Gouge sample; (B) stainless steel block. A horizontal piston on the right-hand-side of this image applies the horizontal (normal) force. The left-hand-side is supported by the HighSTEPS apparatus' internal wall. The vertical piston applies the vertical (shear) force through the central sample holder.

on which the gouge is placed and compacted measures 34 mm by 34 mm. Both the horizontal and vertical sample holders are grooved to a depth of 0.5 mm, with the grooves repeating every 2 mm. The groves ensure shearing occurs inside the gouge layer (Marone et al., 1990).

3.4. Experimental Procedure

In order to test the frictional behavior of the gouge samples, the sample holders are placed inside the apparatus and the horizontal piston is moved into contact with the sample holder. After contact is established, the normal load is increased to 1 MPa. At this stage, if the experiment is to be performed under nominally wet conditions, the impermeable membrane (a plastic bag) containing the sample holders and sample is filled with deionized water, and the normal load of 1 MPa is held for 40 min. This corresponds to the time required for the horizontal piston to reach an approximately constant position. If the experiment is to be performed under nominally dry conditions (room temperature and humidity), this holding period is skipped. Note that while deionized water can take a significant amount of time to reach equilibrium with gouge samples (up to two days with calcite gouge (Carpenter, Collettini, et al., 2016)), here additional XRD analyses were performed on a calcite-rich gouge (N3583) after an experiment to verify that there was no significant loss of calcite or alteration of clay minerals during the experiment, Supplementary Material, Figure S24 and Table S7 in Supporting Information S1. Next, the normal load is increased to either 10, 30, or 50 MPa, depending on the experiment. These values correspond to effective stresses typical of lithostatic burdens at approximately 650, 2,000, and 3,300 m depth, respectively; depths relevant for shallow faults. This normal load is then held for 20 min to allow for sample compaction, Supplementary Material, Figure S8 in Supporting Information S1. At this point nominally wet samples have been equilibrating with the added water for approximately 1.5–2.5 hr, depending on the normal stress of the experiment. Then, the vertical piston, which is brought into contact with the vertical sample holder at the beginning of the experiment, is lowered at 10 $\frac{\mu m}{sec}$ for 11 mm, Figure 4. This constitutes the run-in phase of the experiment which allows for the development of the shear fabric and steady-state friction (e.g., Pozzi et al. (2022), Noël et al. (2023), Noël, Giorgetti, et al. (2024)). After the run-in, the velocity-step sequence is begun. Each velocity step is 500 μm long, with 3, 10, 30, 100, and 300 $\frac{\mu m}{sec}$ being the up-step velocities. Next, the slide-hold-slide sequence is begun, where during each slide-hold-slide the sample is sheared for 500 μm at 10 $\frac{\mu m}{sec}$ before the vertical piston holds a constant position for either 1, 3, 10, 30, 100, 300, 1,000, or 3,000 s, after which the sample is again sheared at 10 $\frac{\mu m}{sec}$ for 500 μm as the next sliding phase is carried out. Finally, the vertical and then horizontal forces are removed by first raising the vertical piston and then retracting the horizontal piston. At this stage the sheared sample is

21699356, 2025, 2, Downloaded from https://agupubs.onlinelibrary.wiley.com/doi/10.1029/2024JB030213 by Cochrane France, Wiley Online Library on [28/01/2025]. See the Terms and Conditions (https://onlinelibrary.wiley.com/terms-and-conditions) on Wiley Online Library for rules of use; OA articles are governed by the applicable Creative Commons License

21699356, 2025, 2, Downloaded from https://agupubs.onlinelibrary.wiley.com/doi/10.1029/2024JB030213 by Cochrane France, Wiley Online Library on [28/01/2025]. See the Terms and Conditions (https://onlinelibrary.wiley.com/terms-and-conditions) on Wiley Online Library for rules of use; OA articles are governed by the applicable Creative Commons License

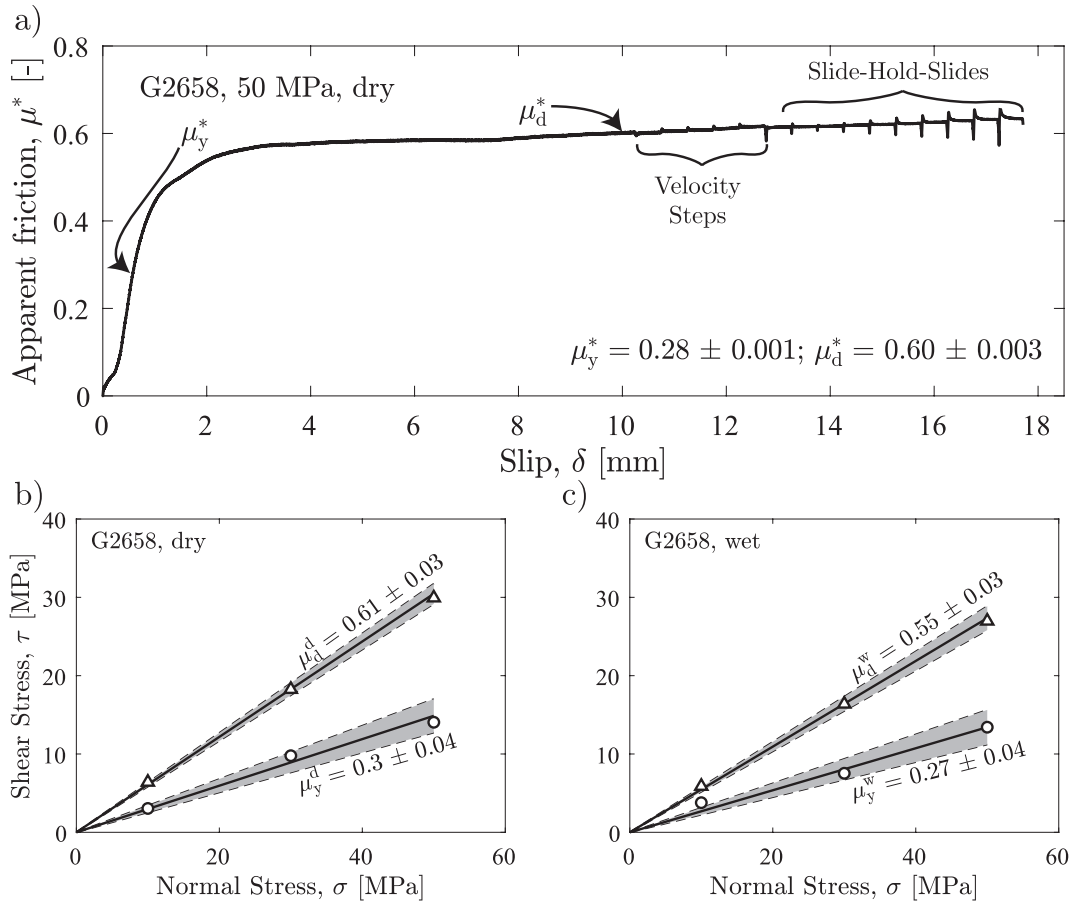

Figure 4. (a) An example experiment, G2658 at 50 MPa normal stress under dry conditions. (b), (c) A demonstration of how the picked values of the apparent frictional yield and dynamic friction coefficients are used to calculate the actual coefficients of frictional yield and dynamic friction coefficients of the samples. The sample G2658 is used as an example.

stored, dried, and then placed in epoxy resin to enable later thin section preparation for micro-structural analysis. All 18 samples were tested at 10, 30, and 50 MPa under both nominally wet and nominally dry conditions resulting in 108 total experiments. Note that all references to wet and dry conditions from this point on refer to nominally wet (immersed but not necessarily saturated) and nominally dry (room humidity, approximately 40%) conditions, respectively. All experiments are performed at room temperature, but it should be noted that, at low temperatures (<300°C), first-order friction characteristics are considered to be relatively independent of temperature (e.g., Scholz (2019), ch. 2). That said, second-order friction characteristics do often show temperature dependence (e.g., Blanpied et al. (1991), Kolawole et al. (2019), Jeppson et al. (2023)).

4. Data Treatment

Considering that the gouges present a constant surface area of 34 mm by 34 mm, the applied normal stress, σ, and shear stress, τ, are calculated based on the applied vertical and horizontal forces, F_v and F_h, respectively. Note that the shear stress is applied across an area twice as large as that for the normal stress as the experiments were performed in double-direct shear. Error in the force measurements was taken as 0.3 kN, based on standard levels of noise. The slip, δ, is calculated as the difference in vertical position based on the values recorded by the optical encoder attached to the vertical piston just above the sample. The layer thickness is calculated based on the values recorded by the optical encoder fixed to the horizontal piston. Error in the displacement measurements was taken as 250 nm, based on standard levels of noise (e.g., Figure 5c). The effective error on all single measurements propagates for other derived quantities, see in Supporting Information S1. Displacement data are corrected based

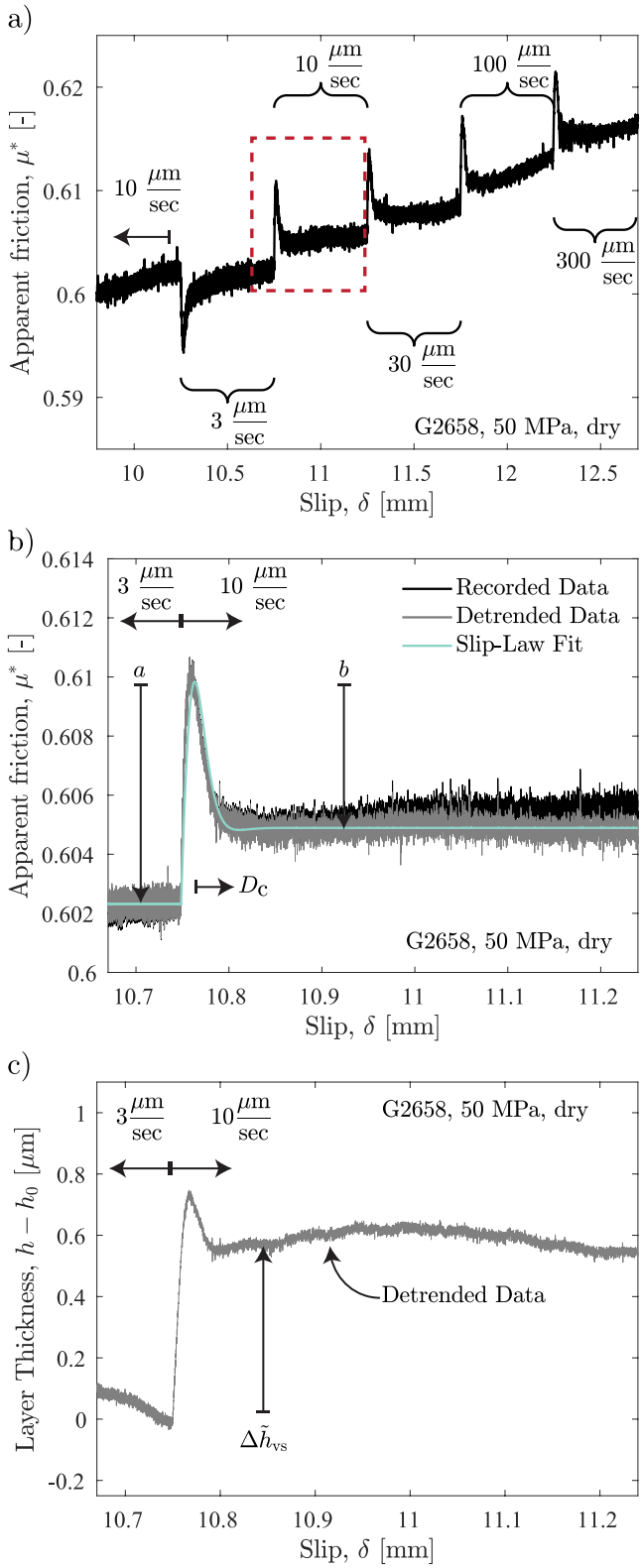

Figure 5.

on machine stiffnesses (Violay et al., 2021). The data are not filtered and were collected at 10 Hz except during the velocity steps where the recording frequency was 2 kHz.

4.1. Friction Coefficients

Apparent friction, μ^*, is defined based on the ratio between τ and σ. Apparent friction coefficients calculated this way neglect cohesion, layer thinning, and densification (Scott et al., 1994).

4.1.1. Coefficient of Frictional Yield, μ_y

During the elastic loading of the sample, a stiffness, k, is defined based on the linear portion of the loading curve, after anelastic deformation, and fit using a least-squares regression. An apparent frictional yield coefficient, μ_y^*, is defined for each experiment based on the last moment that the loading curve intersects the line defined by k, breaking from linearity, Figure 4. This point is also known as the proportional limit. The criterion used for defining the accepted deviation is somewhat arbitrary, meaning application of this parameter to real conditions should be done with care (e.g., Kutz (2009), pg. 445). Instead, this parameter should be treated as a simple proxy for the yield point of the material. Note, however, the yield point is likely dependent on temperature, such that it is difficult to apply these values, found at room temperature, to reservoir conditions. Using the values of μ_y^*, a coefficient of frictional yield, μ_y, is defined for each rock sample using a least-squares estimate, based on the values of μ_y^* from experiments at 10 MPa, 30 MPa, and 50 MPa normal stress, weighted based on the uncertainty of each data point, with cohesion forced to be zero, Figures 4b and 4c. Note that this parameter is not necessarily a coefficient, but is presented as such to capture the dependence on normal stress. Details on the fitting and confidence interval are provided in Supporting Information S1 and Montgomery and Runger (2011). This process is performed for both the wet and dry suites of experiments, yielding a wet, μ_y^w, and dry, μ_y^d, coefficient of frictional yield for each sample.

4.1.2. Dynamic Coefficient of Friction, μ_d

An apparent dynamic coefficient of friction, μ_d^*, is defined for each experiment as the average value of μ^* during the last 1.5 mm of the run-in, Figure 4. Then, for each sample, a dynamic coefficient of friction, μ_d, is defined using a least-squares estimate, based on the values of μ_d^* from experiments at 10 MPa, 30 MPa, and 50 MPa normal stress, weighted based on the uncertainty of each data point, with cohesion forced to be zero, Figures 4b and 4c. Details on the fitting and confidence interval are provided in Supporting Information S1 and Montgomery and Runger (2011). This process is performed for both the wet and dry suites of experiments, yielding a wet, μ_d^w, and dry, μ_d^d, dynamic coefficient of friction.

Figure 5. A series of velocity steps from an example experiment, G2658 at 50 MPa under dry conditions. (a) The full series of velocity steps. After a run-in performed at 10 $\frac{\mu m}{sec}$, velocity steps of 3, 10, 30, 100, and 300 $\frac{\mu m}{sec}$ are performed, each for 500 μm. (b) A zoom on the region outlined by a dotted red line in panel (a). The velocity step is fit with both the slip and aging laws, with the slip-law fit shown here. The parameters a, b, and D_c are illustrated. (c) The change in layer thickness based on detrended data. This image illustrates how $\Delta\tilde{h}_{vs}$ is found.

21699356, 2025, 2, Downloaded from https://agupubs.onlinelibrary.wiley.com/doi/10.1029/2024JB030213 by Cochrane France, Wiley Online Library on [28/01/2025]. See the Terms and Conditions (https://onlinelibrary.wiley.com/terms-and-conditions) on Wiley Online Library for rules of use; OA articles are governed by the applicable Creative Commons License

21699356, 2025, 2, Downloaded from https://agupubs.onlinelibrary.wiley.com/doi/10.1029/2024JB030213 by Cochrane France, Wiley Online Library on [28/01/2025]. See the Terms and Conditions (https://onlinelibrary.wiley.com/terms-and-conditions) on Wiley Online Library for rules of use; OA articles are governed by the applicable Creative Commons License

4.2. Velocity Steps

The velocity dependence of friction, a key component of one of the two principal criteria for the nucleation of a dynamic earthquake (Rice & Ruina, 1983; Ruina, 1983), is modeled using the rate-and-state friction constitutive law (Dieterich, 1979),

$$\mu^* = \mu_0^* + a\ln\left(\frac{v}{v_0}\right) + b\ln\left(\frac{v_0\theta}{D_c}\right), \tag{1}$$

where μ_0^* is an initial value of apparent friction prior to a change in velocity from v_0 to v, a is the direct effect, b is the evolution effect, D_c is the critical slip distance, and θ is a state variable which is given by,

$$\frac{d\theta}{dt} = -\frac{v\theta}{D_c}\ln\left(\frac{v\theta}{D_c}\right), \tag{2}$$

when described by the slip law (Ruina, 1983). Velocity steps are detrended and then fit with RSFit3000 (Skarbek & Savage, 2019), Figure 5. Insight into frictional stability can then be provided by evaluating $a - b$, where $a - b > 0$ represents velocity-strengthening behavior and $a - b < 0$ velocity-weakening behavior. Velocity-weakening behavior is one of the necessary conditions for unstable fault slip under the assumption of small perturbations (Rice & Ruina, 1983; Ruina, 1983).

4.3. Slide-Hold-Slides

Inter-seismic healing can be assessed through the use of slide-hold-slides (Dieterich, 1972), providing insight into potential earthquake recurrence time and strength recovery along faults. The healing that occurs during a given slide hold slide, $\Delta\mu_h^*$, is found as the difference between the peak in apparent friction achieved upon reshearing and the steady-state value of apparent friction prior to the hold, Figures 6a and 6b. Generally, the healing increases with the logarithm of time (Dieterich, 1972). This allows for the definition of a healing rate, β, which is defined based on (Paterson and Wong (2005), pg. 174),

$$\Delta\mu_h^* = \beta\log_{10}\left(1 + \frac{t_h}{t_c}\right), \tag{3}$$

where t_h is the hold time and t_c is the hold time for which the healing can be considered to be zero, taken here as one divided by the recording frequency of 10 Hz. This is then solved for β with a weighted-least-squares estimate using all eight holds, Figure 6d.

4.4. Dilatancy Measurements

4.4.1. Velocity Steps

Based on Marone and Kilgore (1993), Ikari et al. (2009), Giacomel et al. (2021), and analogous to the parameter ϵ from Segall and Rice (1995), a parameter α representing the normalized dilation is defined for each velocity step,

$$\frac{\Delta h_{vs}}{h_0} = \alpha\ln\left(\frac{v}{v_0}\right), \tag{4}$$

which acts as a measure of the dilatancy response of the gouge to a change in velocity. Then, Δh_{vs} is the near-instantaneous dilantancy that occurs when the velocity changes from v_0 to v during a velocity step and h_0 the layer thickness just prior to the step. Note that the layer thickness is de-trended prior to this calculation based on the approximately linear steady-state change in layer thickness occurring after the velocity step, Figure 5c.

4.4.2. Slide-Hold-Slides

The change in layer thickness that occurs during a given slide hold slide, Δh_{shs}, is calculated as (e.g., Giacomel et al. (2021)),

21699356, 2025, 2, Downloaded from https://agupubs.onlinelibrary.wiley.com/doi/10.1029/2024JB030213 by Cochrane France, Wiley Online Library on [28/01/2025]. See the Terms and Conditions (https://onlinelibrary.wiley.com/terms-and-conditions) on Wiley Online Library for rules of use; OA articles are governed by the applicable Creative Commons License

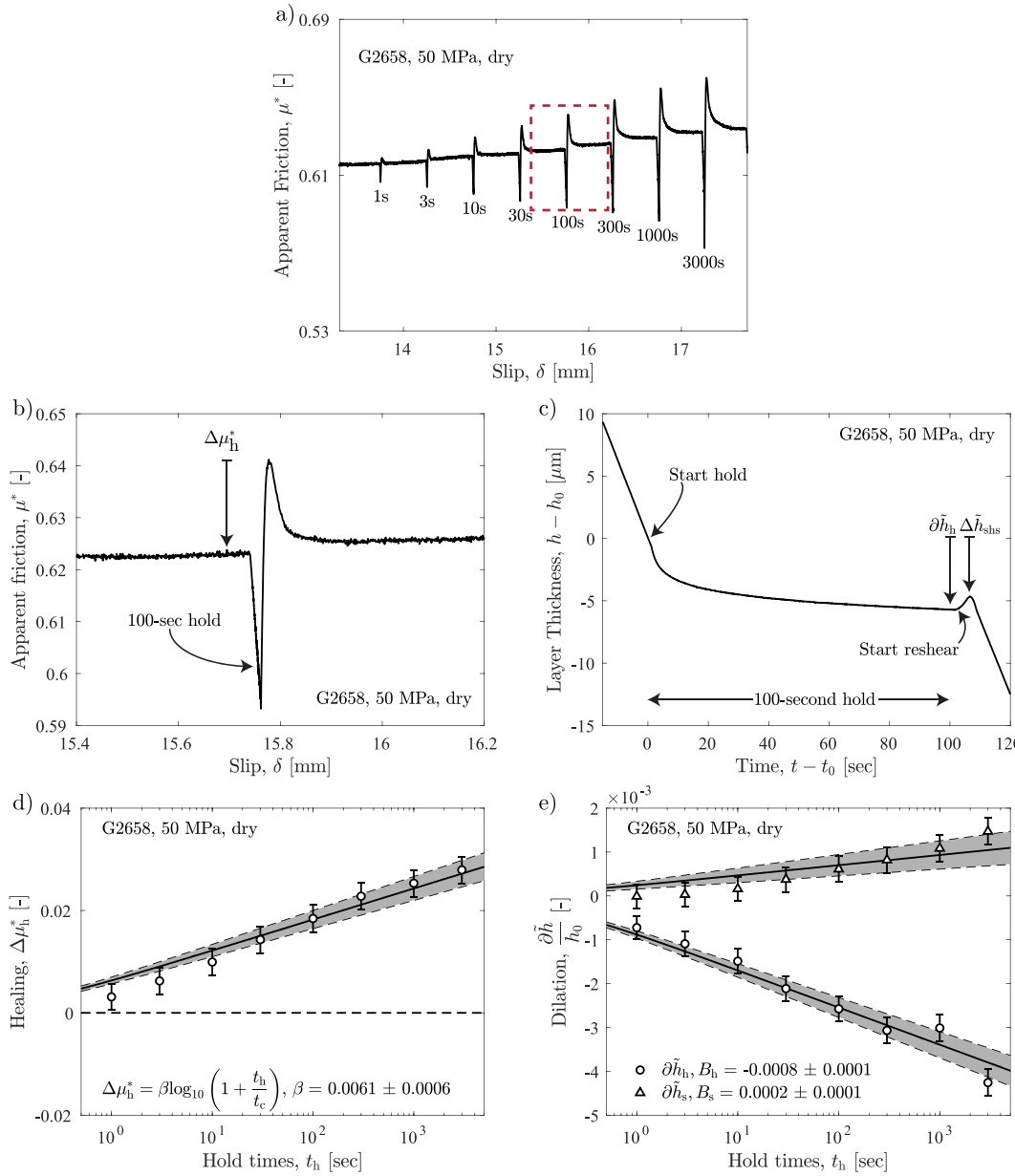

Figure 6. (a) An example of a sequence of slide-hold-slides for sample G2658 at 50 MPa under dry conditions. The hold periods are written under the minimum value of apparent friction reached during each hold. (b) A zoom on the area in panel (a) delineated by a dotted red box. (c) The change in layer thickness occurring during the 100-s hold, corresponding to the dotted red box in panel (a). Note that, from Equation 5, $\Delta h_{shs} = \partial\tilde{h}_h + \partial\tilde{h}_s$. (d) The healing incurred after each hold is plotted as points. These points are then fit to find a value for the healing rate, β. The error for the linear fit is weighted based on the error of each value of $\Delta\mu^*_h$ and fit with a 95 percent confidence interval. (e) The normalized dilation incurred during the hold, $\partial\tilde{h}_h$, and upon reshear, $\partial\tilde{h}_s$. These data are then fit with Equation 6 to find the dilation rates, B_h, B_s, and B_{shs} (not shown).

$$\Delta h_{shs} = \partial\tilde{h}_h + \partial\tilde{h}_s, \tag{5}$$

where $\partial\tilde{h}_h$ is the dilation that occurs during the hold phase, based on the average thickness of the gouge (i.e., considering the experiments are performed in double-direct shear), and $\partial\tilde{h}_s$ is the dilation that occurs upon re-shearing, again based on the average thickness of the gouge. Note that $\partial\tilde{h}_h$ is a negative value as the gouge

compacts during a hold. This allows for the definition of three dilation rates: B_h, B_s, B_{shs}, for the hold periods, re-shearing events, and overall slide-hold-slide sequence which are the best-fit slopes of

$$\frac{\partial \tilde{h}_h}{h_0} = B_h \log_{10}\left(1 + \frac{t_h}{t_c}\right), \quad \frac{\partial \tilde{h}_s}{h_0} = B_s \log_{10}\left(1 + \frac{t_h}{t_c}\right), \quad \frac{\Delta h_{shs}}{h_0} = B_{shs} \log_{10}\left(1 + \frac{t_h}{t_c}\right). \tag{6}$$

An illustration of these calculations can be seen in Figures 6c and 6e. Note that, as Δh_{shs} is a linear combination of $\partial \tilde{h}_h$ and $\partial \tilde{h}_s$, B_{shs} is also a linear combination of B_h and B_s. Therefore, B_h and B_s, two different measurements of dilatancy at different parts of the slide-hold-slides, will be presented here to highlight the rate of change in layer thickness during the slide-hold-slides. Other authors have first de-trended the layer thickness to account for monotonic long-term trends in dilation (Giacomel et al., 2021). This was not done here due to the use of load point displacement measurements (as opposed to measurements directly on the fault). Correcting for layer thickness as a function of vertical slip while using load point displacement measurements would incorrectly adjust layer thickness during the re-shear period prior to the re-initiation of slip. Finally, while the data fit to all three measured dilations in Equation 6 are not truly linear, their fitted slopes still serve as a useful tool to compare the relative tendencies for dilation in the different experiments.

5. Results

5.1. Sample Characteristics

5.1.1. Alteration Features

SEM analyses showed clear differences in sample mineralogy. In particular, certain samples were clearly highly altered presenting many secondary minerals, while others were composed almost exclusively of primary minerals. As an example, Figure 7 shows four samples: LA02767 (a), LA03749 (b), LA02422 (c), and N4343 (d). While LA02767 has experienced alteration, in particular with the presence of chlorite and quartz, it is one of the least-altered samples in this study, and may therefore be representative of a zone which has undergone only limited rock-fluid interaction. LA03749 is an altered sample principally composed of phyllosilicates (kaolinite and smectite), with some carbonate minerals (ankerite). It is likely that the rod-like shapes were originally plagioclase. In LA02422, likely coming from an illite-rich or Al-smectite/kaolinite-rich zone, phyllosilicates (kaolinite and illite) and carbonates (siderite) are common. N4343 contains a significant amount of chlorite and is thus likely coming from a chlorite-rich zone. However, the presence of other phyllosilicates suggests this sample might represent an intermediate state, with multiple alteration phases.

5.1.2. XRD

The detailed XRD results are presented in Supplementary Material, Tables S1–S5 in Supporting Information S1, but a simplified version is given here in Table 2. Note that the expandable clays and kaolinite are typical of the Al-smectite/kaolinite- or Mg-smectite-rich zones (kaolinite is never associated to Mg-smectite), the micas are typical of the illite-rich zone (illite is a dioctahedral mica), and chlorite is typical of the chlorite-rich zone. The samples are classified based on both their absolute weight percentage of phyllosilicate content and the relative amounts of each phyllosilicate, Table 2. Samples more than 40% by weight phyllosilicate are considered highly altered, between 20% and 40% by weight are moderately altered, and below 20% are slightly altered. In this sense, phyllosilicate content is used a proxy for the level of alteration as phyllosilicates are secondary minerals in these samples. If a sample's phyllosilicate content is made up of more than 67% of a given phyllosilicate type then that sample is considered to be representative of the zone corresponding to that phyllosilicate. Based on this classification, LA03749 has a mineralogy representative of a highly altered Al-smectite/kaolinite-rich zone. B494D, S491I, N3583, and N3808 have mineralogies which might be representative of Al-smectite/kaolinite- or Mg-smectite-rich zones which are moderately altered. G2658, N4330, and N4422 could be representative of Mg-smectite zones that are only slightly altered. S491B can be considered representative of a highly altered illite-rich zone. LA02422 and LA02451 can be considered highly altered samples, intermediate between all three zones. M1430 and N4343 are intermediate between zones but only moderately altered. LA03758 is also intermediate but only lightly altered. LA02767, G2690, G3005, and G3130 can be considered to represent the chlorite-rich zone with a low level of alteration.

21699356, 2025, 2, Downloaded from https://agupubs.onlinelibrary.wiley.com/doi/10.1029/2024JB030213 by Cochrane France, Wiley Online Library on [28/01/2025]. See the Terms and Conditions (https://onlinelibrary.wiley.com/terms-and-conditions) on Wiley Online Library for rules of use; OA articles are governed by the applicable Creative Commons License

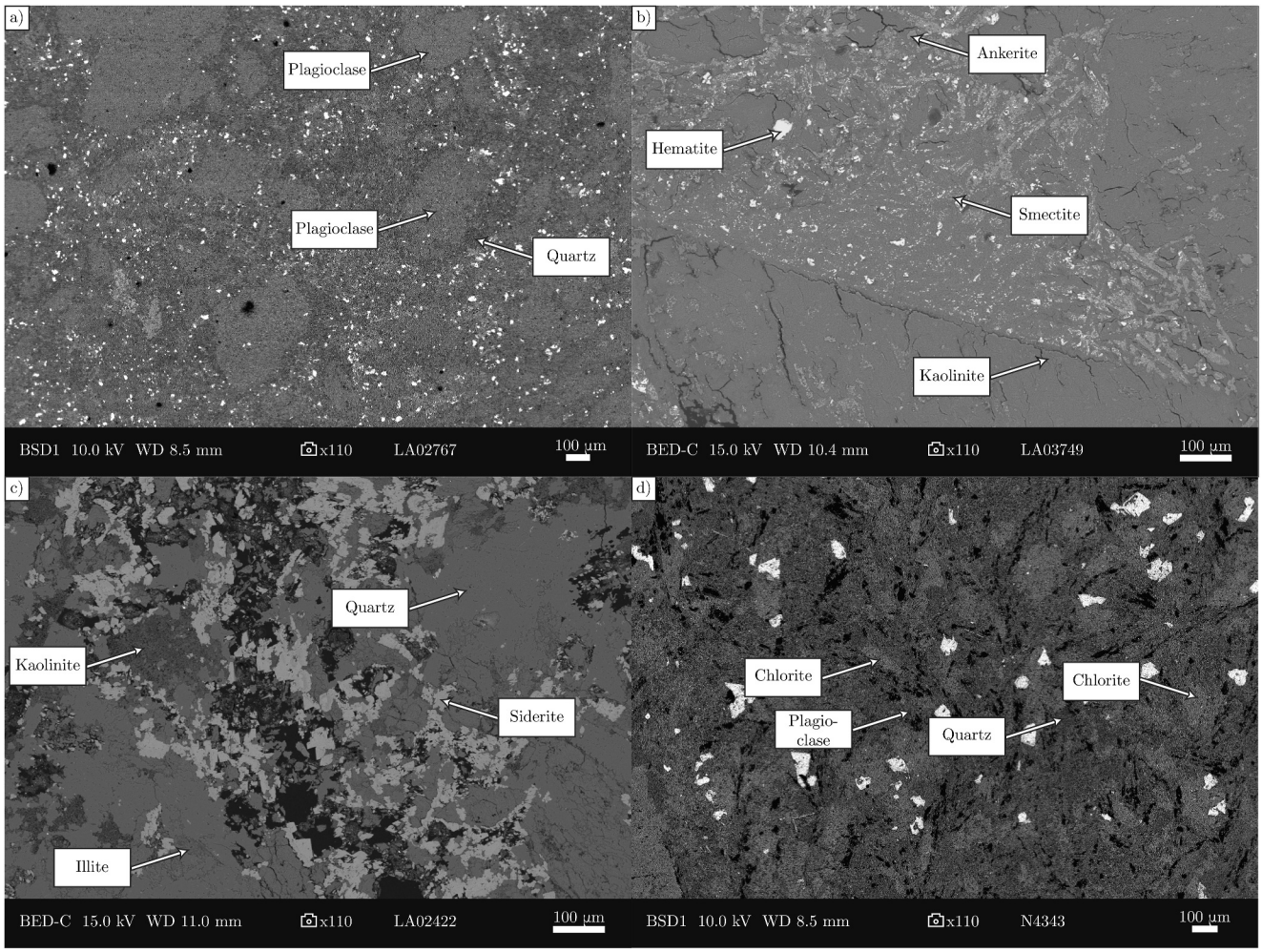

Figure 7. Images of polished thin sections made from intact samples taken during SEM analysis with backscattered electrons, illustrating density contrast. (a) LA02767 is only lightly altered, with the presence of a small amount of chlorite. (b) LA03749 is highly altered, exhibiting secondary minerals almost exclusively. In particular, this sample is marked by the significant presence of smectite and kaolinite, making it representative of the clay cap of a geothermal reservoir in a volcanic arc setting. (c) LA02422 is also highly altered, with the most abundant phyllosilicates being dioctahedral micas, as can be seen by the illite present on the SEM image. However, this sample is classified as intermediate due to the presence of kaolinite and 2:1 expandable dioctahedral clays. (d) N4343 is only moderately altered, but contains a significant amount of chlorite and is classified as intermediate between alteration zones. In (b) the shapes of replaced primary minerals (in many instances likely plagioclase) can be clearly seen.

5.2. Overall Summary of Friction Coefficients

Coefficients of frictional yield have a median value of approximately 0.26 in dry conditions and 0.24 in wet conditions, meaning any water weakening that is present is generally within the errors of the calculations of the friction coefficients. Dry dynamic friction coefficients have values which are typically between 0.55 and 0.60, with the lowest value being 0.25, the highest 0.61, and the median 0.58. Sample with more phyllosilicate content generally have low dynamic friction coefficients. Note that these friction coefficients, in particular the dynamic friction coefficients, are generally associated with narrow 90% confidence windows, despite all possible sources of experimental error, Table 3. This acts as justification for cohesion being neglected. Water-induced frictional-strength reduction for the dynamic coefficient of friction is present in all but one sample (LA02767). The median value of water-induced frictional-strength reduction is 0.09, with the most extreme water-induced frictional-strength reduction seen in S491I, a difference of 0.16 or 29%. Water-induced frictional-strength reduction is more common in samples rich in phyllosilicate content. The friction coefficients are summarized in Table 3, with

21699356, 2025, 2, Downloaded from https://agupubs.onlinelibrary.wiley.com/doi/10.1029/2024JB030213 by Cochrane France, Wiley Online Library on [28/01/2025]. See the Terms and Conditions (https://onlinelibrary.wiley.com/terms-and-conditions) on Wiley Online Library for rules of use; OA articles are governed by the applicable Creative Commons License

Journal of Geophysical Research: Solid Earth

10.1029/2024JB030213

Table 2
The Results of the XRD Analysis for All Samples

Sample	Location	Pred. Alt. Type	Plagioclase	Clino-Px	K-spar	Quartz	2:1 exp. Dioct.	2:1 exp. Trioct	Kaolinite	Mica dioct.	Mica trioct.	Chlorite	Vermiculite	Other	Amorphous
B494D	Les Saintes	Smectite	33.7 ± 0.5	-	5.9 ± 0.3	28.2 ± 0.4	12.7 ± 0.8	5.4 ± 0.4	-	-	-	4.4 ± 0.5	-	9.9 ± 0.3	5 ± 0
S491I	Les Saintes	Smectite	25.9 ± 0.4	-	5.3 ± 0.2	27.4 ± 0.3	24.8 ± 0.7	3.8 ± 0.4	-	-	-	-	-	13.1 ± 0.5	5 ± 0
S491B	Les Saintes	Illite	-	-	1.7 ± 0.2	43.2 ± 0.4	-	-	-	46.2 ± 0.5	3.2 ± 0.3	-	-	4.7 ± 0.2	-
LA02422	Lamentin	Intermediate	-	-	-	34 ± 0.2	7.4 ± 0.5	-	15.6 ± 0.3	27.9 ± 1.2	-	-	-	15.2 ± 1.3	-
LA02541	Lamentin	Intermediate	13.8 ± 0.2	2.8 ± 0.2	-	19.5 ± 0.2	14.3 ± 0.7	-	-	17.7 ± 0.8	-	11.6 ± 0.4	-	20.3 ± 0.7	-
LA02767	Lamentin	Chlorite	50.7 ± 1.7	-	2.8 ± 0.2	17.3 ± 0.2	-	-	-	0.6 ± 0.2	-	9.5 ± 0.3	-	11.2 ± 0.7	8 ± 0
LA03749	Lamentin	Al-smectite/ Kaolinite	11.8 ± 0.2	-	-	0.6 ± 0.1	41.4 ± 0.7	-	19 ± 0.9	-	-	-	1.2 ± 0.2	26.1 ± 1.2	-
LA03758	Lamentin	Intermediate	51.7 ± 0.8	6.9 ± 0.2	3.1 ± 0.2	0.4 ± 0	8.7 ± 0.2	-	1.9 ± 0.2	-	-	8.4 ± 0.5	-	10.5 ± 0.8	8.4 ± 0
M1430	Mount Meager	Intermediate	40.6 ± 0.4	-	10.4 ± 0.3	20.5 ± 0.2	9.2 ± 0.2	-	-	2 ± 0.2	-	9.9 ± 0.6	-	7.3 ± 0.2	-
G2658	Summerland Basin	Mg-smectite	28.3 ± 0.5	15.2 ± 0.5	29 ± 1.15	5.6 ± 0.3	-	13.2 ± 0.5	-	-	1 ± 0.1	1.2 ± 0.3	-	6.5 ± 0.8	-
G2690	Summerland Basin	Chlorite	25.9 ± 0.6	-	30.3 ± 1.5	5.4 ± 0.1	-	3.7 ± 0.6	-	-	-	13.2 ± 0.6	-	20.6 ± 1.2	5 ± 0
G3005	Summerland Basin	Chlorite	21.3 ± 0.3	11.1 ± 0.2	15.9 ± 0.3	-	-	3.4 ± 0.3	-	-	-	11.3 ± 0.8	0.5 ± 0.2	36.5 ± 1.6	-
G3130	Summerland Basin	Chlorite	33.3 ± 2.3	3.5 ± 0.3	20.6 ± 1.4	7.3 ± 0.5	-	1 ± 0.1	-	-	-	18.9 ± 2	-	15.5 ± 1.5	5 ± 0
N3583	Newberry	Mg-smectite	39.8 ± 0.8	-	2.7 ± 0.3	10.2 ± 0.1	-	23.5 ± 0.6	-	-	-	-	-	23.9 ± 0.7	-
N3808	Newberry	Mg-smectite	49.3 ± 0.8	-	2.5 ± 0.2	15.6 ± 0.2	-	21.5 ± 2.3	-	-	-	-	-	11 ± 0.5	-
N4330	Newberry	Mg-smectite	62.4 ± 2.1	10.1 ± 0.4	0.6 ± 0.2	4.4 ± 0.1	-	15.4 ± 0.4	-	-	-	-	-	7.3 ± 0.7	5 ± 0
N4343	Newberry	Intermediate	39.5 ± 1.5	-	4.9 ± 0.2	17.7 ± 0.4	-	9.2 ± 0.9	-	-	-	11.1 ± 2.7	-	17.7 ± 0.9	-
N4422	Newberry	Mg-smectite	55.7 ± 1.4	1.1 ± 1.2	4 ± 0.2	11.2 ± 0.2	-	18.3 ± 1.1	-	-	-	-	-	9.7 ± 0.8	-

Note. The results here are simplified through the use of an "Other" category. Detailed XRD results can be found in Supplementary Material, Tables S1–S5 in Supporting Information S1. Values are given in weight percentage. Uncertainties expressed as standard deviation of the Rietveld refinement only. K-spar—potassium feldspars, Clino-Px—clinopyroxenes, dioct. - dioctahedral (Al—rich for expandables), trioc. —trioctahedral (Mg—rich for expandables), exp. —expandable, that is, either pure smectite or smectite-containing mixed layer. Samples used for XRD underwent a different grinding procedure than those used for friction tests.

21699356, 2025, 2, Downloaded from https://agupubs.onlinelibrary.wiley.com/doi/10.1029/2024JB030213 by Cochrane France, Wiley Online Library on [28/01/2025]. See the Terms and Conditions (https://onlinelibrary.wiley.com/terms-and-conditions) on Wiley Online Library for rules of use; OA articles are governed by the applicable Creative Commons License

21699356, 2025, 2, Downloaded from https://agupubs.onlinelibrary.wiley.com/doi/10.1029/2024JB030213 by Cochrane France, Wiley Online Library on [28/01/2025]. See the Terms and Conditions (https://onlinelibrary.wiley.com/terms-and-conditions) on Wiley Online Library for rules of use; OA articles are governed by the applicable Creative Commons License

Table 3
A Summary of the Friction Coefficients

Sample	Location	Pred. Alt. Type	μ_y^d [-]	μ_y^w [-]	μ_d^d [-]	μ_d^w [-]
B494D	Les Saintes	Smectite	0.26 ± 0.02	0.23 ± 0.01	0.57 ± 0.01	0.48 ± 0.01
S491I	Les Saintes	Smectite	0.18 ± 0.04	0.19 ± 0.04	0.56 ± 0.03	0.40 ± 0.01
S491B	Les Saintes	Illite	0.16 ± 0.05	0.18 ± 0.04	0.46 ± 0.01	0.33 ± 0.02
LA02422	Lamentin	Intermediate	0.26 ± 0.02	0.17 ± 0.03	0.48 ± 0.02	0.35 ± 0.01
LA02541	Lamentin	Intermediate	0.21 ± 0.04	0.21 ± 0.07	0.51 ± 0.02	0.37 ± 0.02
LA02767	Lamentin	Chlorite	0.29 ± 0.02	0.23 ± 0.06	0.59 ± 0.03	0.59 ± 0.03
LA03749	Lamentin	Al-smectite/Kaolinite	0.19 ± 0.03	0.15 ± 0.02	0.25 ± 0.05	0.24 ± 0.02
LA03758	Lamentin	Intermediate	0.25 ± 0.04	0.23 ± 0.03	0.59 ± 0.02	0.53 ± 0.03
M1430	Mount Meager	Intermediate	0.22 ± 0.06	0.24 ± 0.05	0.58 ± 0.02	0.50 ± 0.02
G2658	Summerland Basin	Mg-smectite	0.30 ± 0.04	0.27 ± 0.04	0.61 ± 0.03	0.55 ± 0.03
G2690	Summerland Basin	Chlorite	0.28 ± 0.05	0.32 ± 0.07	0.58 ± 0.02	0.51 ± 0.01
G3005	Summerland Basin	Chlorite	0.27 ± 0.05	0.30 ± 0.01	0.60 ± 0.03	0.54 ± 0.02
G3130	Summerland Basin	Chlorite	0.30 ± 0.02	0.28 ± 0.02	0.60 ± 0.02	0.53 ± 0.01
N3583	Newberry	Mg-smectite	0.24 ± 0.05	0.22 ± 0.03	0.55 ± 0.07	0.48 ± 0.09
N3808	Newberry	Mg-smectite	0.22 ± 0.02	0.24 ± 0.06	0.58 ± 0.04	0.48 ± 0.03
N4330	Newberry	Mg-smectite	0.24 ± 0.05	0.28 ± 0.04	0.59 ± 0.04	0.49 ± 0.06
N4343	Newberry	Intermediate	0.27 ± 0.04	0.30 ± 0.11	0.59 ± 0.02	0.49 ± 0.02
N4422	Newberry	Mg-smectite	0.28 ± 0.14	0.25 ± 0.04	0.59 ± 0.03	0.50 ± 0.03

Note. The coefficients of frictional yield for dry and wet conditions are given by μ_y^d and μ_y^w, respectively. The dynamic coefficients of friction for dry and wet conditions are given by μ_d^d and μ_d^w, respectively. Each friction coefficient is based on three separate experiments, each at a given normal stress of either 10, 30, or 50 MPa. See Figure 4 for an illustration of this procedure. The error refers to the 90% confidence interval fit, see Supporting Information S1. Predominant alteration type is based on Table 2.

a more detailed look at site-specific results in the Supplementary Material, Section 4 and Figures S9 and S10 in Supporting Information S1.

5.3. Overall Summary of Velocity Steps

Of the 18 samples tested, in 14 cases a is larger in wet conditions than in dry conditions. Similarly, in 11 instances b is larger in dry conditions than in wet conditions. Ultimately, however, $a - b$ is larger (more positive) in wet conditions than in dry conditions for 17 of the samples. Regarding the critical slip distance, D_c is often larger (for 15 out of 18 samples) in wet conditions than in dry conditions. Finally, α is larger in wet conditions than in dry conditions for 15 of the samples.

As normal stress increases, a decreases for 14 of the samples. Similarly, b decreases with increasing normal stress for 12 of the samples. Finally, however, $a - b$ increases with increasing normal stress for 4 of the samples, decreases for 3 samples, and displays no clear trend with normal stress for 11 samples. The critical slip distance increases with increasing normal stress for 6 samples, decreases with increasing normal stress for 1 sample, and displays no clear trend with normal stress for 11 samples. α increases with increasing normal stress for 1 samples, decreases for 2 samples, but displays no clear trend for the other 15 samples. These data can be found in the Supplementary Material, Tables S8–S25 in Supporting Information S1, with a description of site-specific results in the Supplementary Material, Section 4 and Figures S11–S15 in Supporting Information S1.

5.4. Overall Summary of Frictional Healing

The healing rate does not consistently vary with water presence when all of the samples are taken together, in some instances it decreases when the experiment was performed in wet conditions in others it increases. This

21699356, 2025, 2, Downloaded from https://agupubs.onlinelibrary.wiley.com/doi/10.1029/2024JB030213 by Cochrane France, Wiley Online Library on [28/01/2025]. See the Terms and Conditions (https://onlinelibrary.wiley.com/terms-and-conditions) on Wiley Online Library for rules of use; OA articles are governed by the applicable Creative Commons License

effect is clearly composition dependent. When the healing rate varies with normal stress, most often it decreases as normal stress increases, otherwise it remains approximately constant. An increasing healing rate with increasing normal stress is rare in these samples. Phyllosilicate-poor (<25%) samples (B494D, LA02767, LA03758, M1430, G2658, G2690, G3005, G3130) have a decreasing healing rate with increasing normal stress in dry conditions. These data can be found in the Supplementary Material, Tables S26–S30 in Supporting Information S1. Site-specific descriptions of the results can be found in the Supplementary Material, Section 4 and Figures S16 and S18 in Supporting Information S1.

Values for B_h, the dilation rate (often negative, implying compaction) during the hold, are greater (more negative) in wet conditions than in dry conditions for almost all of the experiments performed. The values for B_s, the dilation rate during the reshear, are more mixed when compared between dry and wet conditions, and can be considered generally similar. For higher normal stresses, B_h is often greater. A similar, but less consistent, trend persists for B_s. These data can be found in the Supplementary Material, Tables S26–S30 in Supporting Information S1. Site-specific descriptions of the results can be found in the Supplementary Material, Section 4 and Figures S17 and S19 in Supporting Information S1.

Finally, negative healing rates were consistently observed in N3583 in wet conditions and LA03749 in wet conditions for large hold times. These negative healing rates led to negative healing for large hold times, generally at either 1,000 or 3,000 s. Negative healing was not observed for these samples in dry conditions. Isolated instances of negative healing rates were also observed in LA02422 and N3808. Negative healing will be further discussed in Section 6.1.

5.5. Post-Mortem Microstructure

An analysis of the post-mortem sample fabrics, Figure 8, reveals fabric elements typical of deformation of brittle fault rocks, particularly when phyllosilicate content is low. Phyllosilicate-rich rocks are more likely to develop the S-C-C' fabrics common in this type of material and first described for ductiley-deformed mylonites (e.g., Bertheé et al. (1979), Volpe et al. (2022)), Figures 8b and 8d. Conversely, samples with limited amounts of phyllosilicates are more likely to develop Y-B-P-R fabrics typical of granular-rich faults (e.g., Logan et al. (1992), Volpe et al. (2022)), Figures 8a–8c. In general, the lightly altered samples, limited in their phyllosilicate contents, exhibited the highest levels of localized deformation. In samples richer in phyllosilicates, deformation was more distributed (ductile). This is an indication of a change in mode of deformation, from localized to ductile, as phyllosilicate content increases. Further, a change in mechanism is also likely, as rocks with principally Y-B-P-R fabrics (seen primarily in samples with low phyllosilicate contents) indicate cataclastic processes as the primary deformation mechanism. Conversely, rocks with principally S-C-C' (seen primarily in samples with high phyllosilicate contents) fabrics indicate frictional sliding along foliations (Volpe et al., 2022). Note that both of these mechanisms are brittle deformation mechanisms. This implies that alteration, by producing phyllosilicate minerals in these settings, promotes both a change in deformation mode and mechanism. Generally, dry experiments also produced increased localized deformation compared to wet experiments, with wet experiments also generally yielding more widespread grain-size reduction.

6. Discussion

6.1. Negative Frictional Healing

Interestingly, while the frictional resistance upon reshear of all of the samples increases with the logarithm of hold time for small hold times (<1,000 s), for a few samples (N3583, LA03749, LA02422, and N3808), large hold times (>1,000 s) may result in negative healing rates and even negative healing. This phenomenon is most pronounced in N3583 in wet conditions at all tested normal stresses, Figure 9. This phenomenon is clearly dependent on water presence, as the same sample tested in dry conditions does not result in negative healing, Figure 9. Negative healing rates and negative healing have been previously observed (Boulton et al., 2012; Chen et al., 2015; Jeppson et al., 2023; Orellana et al., 2018; Pozzi et al., 2023; Tesei et al., 2017). Tesei et al. (2017) observed negative healing for bare-surface carbonate samples, relating it to fast-healing gouge patches that ultimately result in the fracturing of the intact rock, yet here experiments were performed on gouge. Orellana et al. (2018), who observed negative healing for small hold times in Opalinus Clay, suggested that their negative healing could be explained by a local overpressure at small hold times; this would result in transiently reduced effective normal stresses and therefore reduced strength. This mechanism is a possible explanation for the

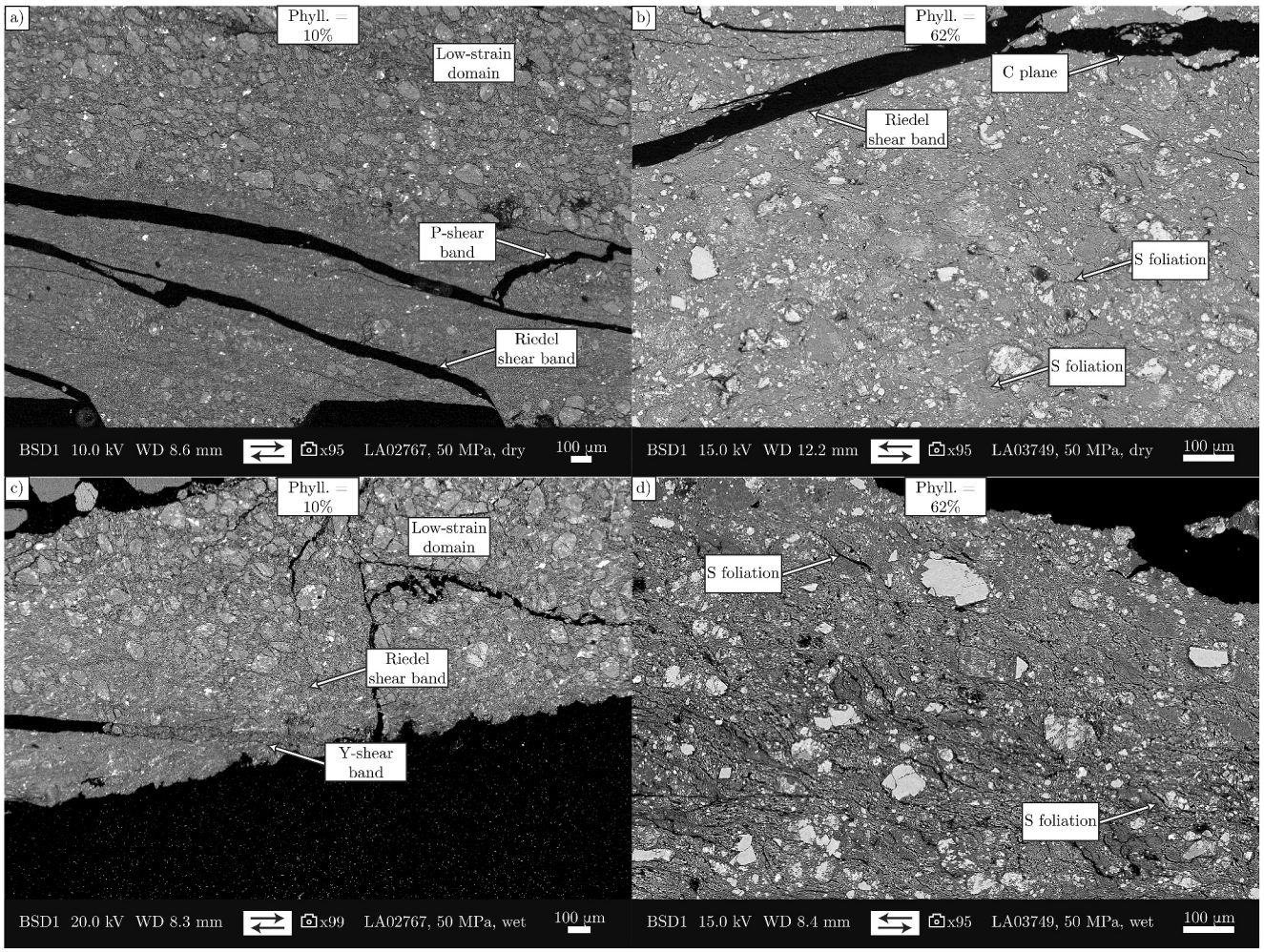

Figure 8. SEM images are of samples deformed at 50 MPa under (a), (b) dry and (c), (d) wet conditions. The samples shown are (a), (c) LA02767 and (b), (d) LA03749. LA02767 represents a sample exhibiting minimal alteration, with a low (10%) weight percentage of phyllosilicates. LA03749 is a highly altered sample with significant amounts of kaolinite and smectite (62% by weight phyllosilicates). (a) A low-strain domain as well as R- and P-shear bands can be seen. (c) A low strain domain along with Y- and R-shear bands can be seen. (b) C planes, R-shear bands, as well as S foliations can be seen. (d) S foliations can be seen. Generally, while localization still occurs for the sample high in phyllosilicate content (LA03749 in (b), (d)), deformation is more ductile (distributed) in this case compared to the sample low in phyllosilicate content (LA02767 in panels (a), (c)). These images can be further compared with Figures 10b–10e, which also shows a sample deformed at 50 MPa containing 24% phyllosilicate content by weight. Arrows underneath the images show the far-field shear direction. It should be noted that the part of the thin section near the teeth (e.g., the bottom of (a)) was often not recovered. Additional localization often occurs in this part of the gouge. The pre-mortem images of these samples can be found in Figures 7a and 7b.

negative healing observed here, and was also suggested by Boulton et al. (2012), but is difficult to confirm without on-fault pore pressure measurements. Here, however, negative healing was only observed at large hold times. Jeppson et al. (2023) observed negative healing only at elevated temperatures (200°C) and suggested that the underlying mechanisms was thermally activated. Here, however, negative healing was observed at room temperature. The negative healing for N3583 in wet conditions is associated with an increased compaction during the hold (negative dilation) relative to dry experiments, Figure 9d, but the dilation upon reshear is quite similar for both wet and dry cases, Supplementary Material, Figure S21 in Supporting Information S1. Reversing the hold times still resulted in only large hold times yielding negative healing, indicating a limited effect of strain, Supplementary Material, Figure S22 in Supporting Information S1.

The post-mortem microstructures of N3583 can be observed in Figure 10, with Figure 10a showing an undeformed sample. In Figures 10b and 10d, the sample deformed in dry conditions and did not demonstrate negative healing. In Figure 10c and 10e the sample deformed in wet conditions and did exhibit negative healing. Clearly, a

21699356, 2025, 2, Downloaded from https://agupubs.onlinelibrary.wiley.com/doi/10.1029/2024JB030213 by Cochrane France, Wiley Online Library on [28/01/2025]. See the Terms and Conditions (https://onlinelibrary.wiley.com/terms-and-conditions) on Wiley Online Library for rules of use; OA articles are governed by the applicable Creative Commons License

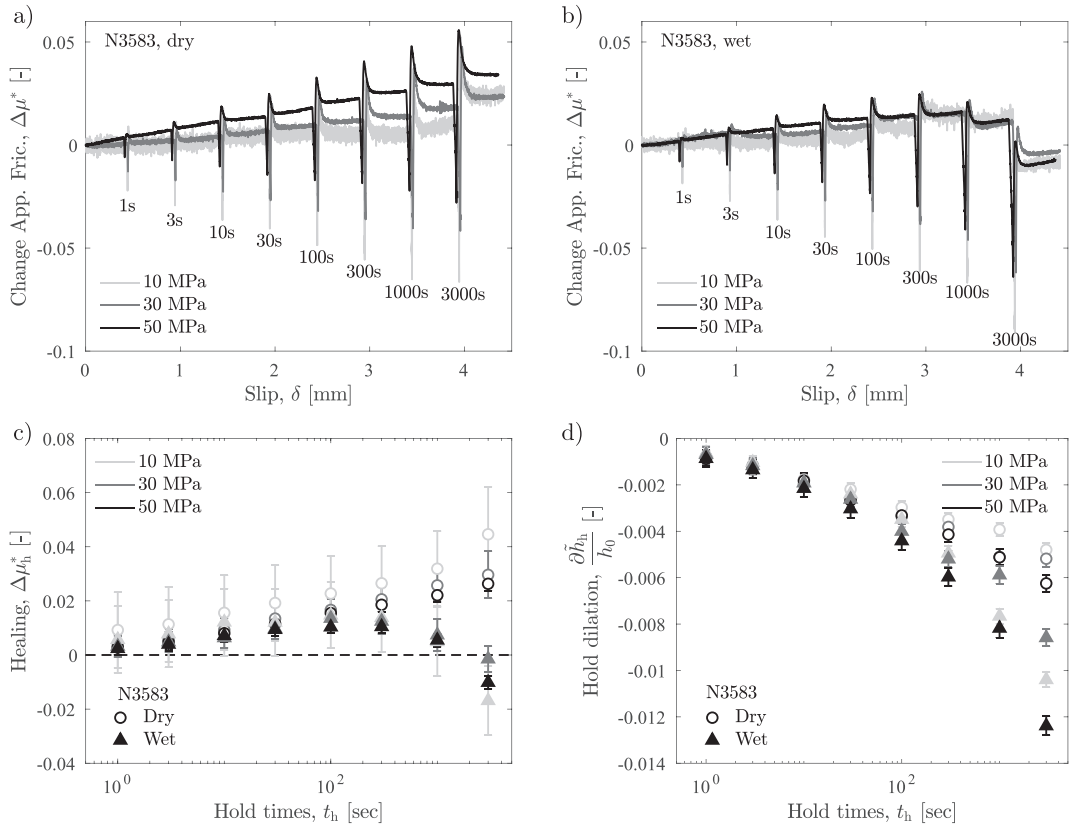

Figure 9. Slide-hold-slides for N3583 in both dry (a) and wet (b) conditions. The length of the hold is written under the minimum value of apparent friction reached during each hold. Importantly, this sample exhibits negative frictional healing, but only in wet conditions for large (>1,000 s) hold times. The (c) healing, $\Delta\mu_h^*$, and (d) normalized dilation during the hold, $\frac{\partial\bar{h}_h}{h_0}$, as a function of hold time, t_h, for these cases (a), (b).

significant difference in grain size can be observed between the two cases. This suggests that the sample deformed in wet conditions experiences significantly more cataclasis than the sample deformed under dry conditions; however, this is a common effect observed in many samples. Further, the grains are more rounded and less angular when N3583 is deformed in wet conditions, which can be indicative of dissolution.

Indeed, Jeppson et al. (2023) speculated that the development of alteration products, such as phyllosilicates, and solution-transfer processes may have lowered the strength of the rock in their case; however, XRD analyses performed after the experiment reveal that the gouge composition did not change during the experiment, at least not on the scale of the bulk, Supplementary Material, Figure S24 and Table S7 in Supporting Information S1. It can be noted in Table 2 that N3583 has the most 2:1 expandable trioctahedral clays of all the samples. N3808, a sample which also showed limited negative healing, also has a significant amount of 2:1 expandable trioctahedral clays. These clays were not measured in LA03749 and LA02422, with instead the presence of 2:1 expandable dioctahedral clays. Why other samples with significant amounts of expandable clays, such as S491I, did not show negative healing is unclear, however. Alternatively, N3583 has more calcite (15.7% by weight, Supplementary Material, Figure S5 in Supporting Information S1) than any other sample (no other sample has more than 10% by weight). Because expandable clays absorb Ca^{2+} ions, it may be that calcite is dissolved during long hold times in wet conditions and, due to its absorption by clay minerals (which have a negative charge), is not able to be re-precipitated, resulting in loss of strength and negative healing. To test this hypothesis, an experiment on N3583 at 50 MPa was run using acid fluid (HCl solution 0.1 M diluted by a factor of 10 yielding a pH of 2). Negative healing was slightly enhanced, but the difference was within experimental error such that the test was inconclusive, Supplementary Material, Figure S23 in Supporting Information S1. XRD analyses, including

21699356, 2025, 2, Downloaded from https://agupubs.onlinelibrary.wiley.com/doi/10.1029/2024JB030213 by Cochrane France, Wiley Online Library on [28/01/2025]. See the Terms and Conditions (https://onlinelibrary.wiley.com/terms-and-conditions) on Wiley Online Library for rules of use; OA articles are governed by the applicable Creative Commons License

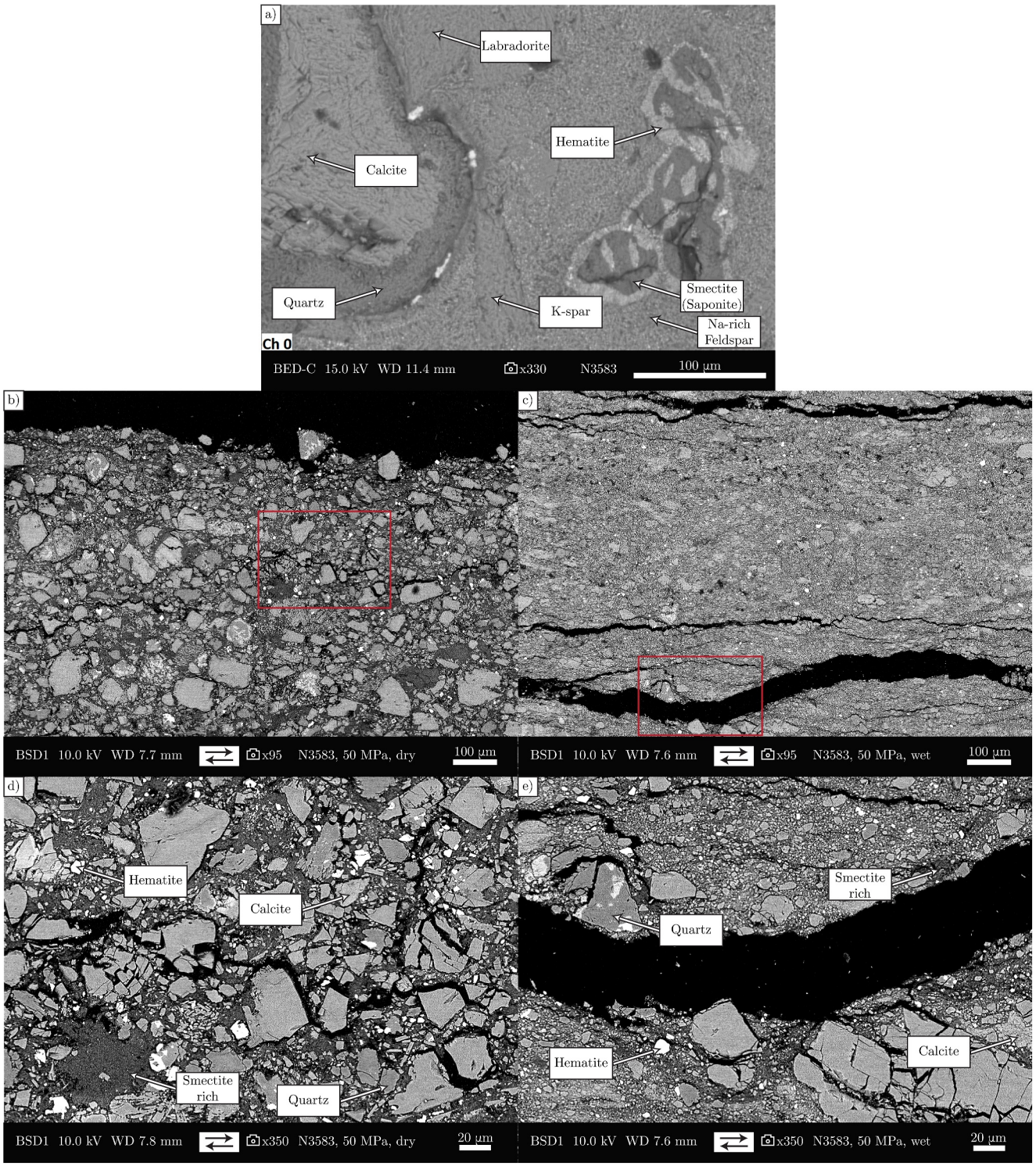

Figure 10. (a) An intact sample of N3583. (b)–(e) N3583 deformed at 50 MPa under (b), (d) dry conditions and (c), (e) wet conditions. N3583 exhibited negative healing under wet conditions. Arrows underneath the images show the far-field shear direction.

analyses on the extracted clay fraction, performed on the post-mortem sample revealed that calcite concentrations did not change before and after the test, nor did the clay mineral species, Supplementary Material, Figure S24 and Table S7 in Supporting Information S1.

21699356, 2025, 2, Downloaded from https://agupubs.onlinelibrary.wiley.com/doi/10.1029/2024JB030213 by Cochrane France, Wiley Online Library on [28/01/2025]. See the Terms and Conditions (https://onlinelibrary.wiley.com/terms-and-conditions) on Wiley Online Library for rules of use; OA articles are governed by the applicable Creative Commons License

21699356, 2025, 2, Downloaded from https://agupubs.onlinelibrary.wiley.com/doi/10.1029/2024JB030213 by Cochrane France, Wiley Online Library on [28/01/2025]. See the Terms and Conditions (https://onlinelibrary.wiley.com/terms-and-conditions) on Wiley Online Library for rules of use; OA articles are governed by the applicable Creative Commons License

A further possibility may be related to the platy structure of phyllosilicates, which cause the accelerated saturation of real contact areas (Carpenter et al., 2011; Carpenter, Ikari, & Marone, 2016; Collettini et al., 2019; Ikari et al., 2016; Saffer & Marone, 2003; Tesei et al., 2012). It may be, for example, that the grain rotation of phyllosilicates results in a texture with pronounced preferred orientation during longer holds which in turn inhibits or even reduces asperity expansion, ultimately reducing either real contact area or the quality of contact, resulting in reduced healing. As dry samples have undergone less cataclasis, larger grains are still intact. For this reason a granular load-bearing framework may still be in place in dry experiments, such that real contact still increases during long holds and negative healing does not result. Further investigation is clearly required.

6.2. Velocity Dependence and Dilatancy

When all of the velocity steps are taken together, it can be seen that a and, in particular, b do not have a clear relationship with the dilation occurring during the velocity step, Figures 11a–11d. However, the overall velocity dependence, $a - b$, does seem to correlate directly with α, Figures 11e and 11f. As seen previously (e.g., Ikari et al. (2009)) the value of α does not seem to depend on upstep velocity. Indeed in Figure 11 it was not necessary to separate the results based on velocity, with all velocity steps plotted together. Certain samples, in particular those with high phyllosilicate contents, displayed negative values of b. This is likely due to the saturation of contact area, as previously seen in experiments on phyllosilicate-rich samples (Carpenter, Ikari, & Marone, 2016; Collettini et al., 2019; Ikari et al., 2009; Saffer & Marone, 2003).

6.3. Frictional Healing and Dilatancy

Generally slightly smaller healing rates are seen at larger normal stresses, Figure 12. However, this trend may be well or poorly pronounced depending on the type of sample. Some samples (in particular those rich in phyllosilicates) do not clearly show this trend at all. Samples also tend to show greater dilation rates at higher normal stresses, maybe counter-intuitively implying that on a per-sample basis more sample compaction during a hold and more sample dilation during reshear yields less healing. This is unexpected as dilatancy should depend on the grain size of the fabric that controls the shear strength (e.g., the boundary shear, in the case of granular materials). At higher stress, less dilation is expected as less grain climbing and rigid body rotation of the grains can be attained without grain fracturing (e.g., Bos and Spiers (2001), Giorgetti et al. (2015)). However, it should be noted that the dilation rates B_s and B_h are both normalized by the gouge thickness prior to the start of a hold, which is significantly less at the start of a hold for experiments at higher normal stresses. Indeed, by simply plotting the healing, $\Delta\mu_h^*$, versus the dilation upon reshear, $\partial\tilde{h}_s$, for all holds performed in all experiments, it can be clearly seen that more dilation corresponds to more healing, Figures 12a and 12b. As a matter of fact, normalizing the dilation by layer thickness and replotting results in a less collapsed trend. This implies that the anticorrelation between sample dilation during reshear and healing is an artifact of the normalization and that gouge thickness at the start of a hold is not the correct normalization parameter for dilation rates. It is likely that the correct normalization involves a micro-scale measurement local to the experimental fault and not a macro-scale measurement at the load cells of the machine's pistons. A similar argument can be made for the larger dilation rates seen in wet conditions, as the gouge has a larger tendency to compact under wet conditions. That said, there still exists a positive trend between healing rate and dilation-upon-reshear rate, Figures 12c and 12d.

6.4. The Influence of Water

As previously mentioned, wet samples tend to have compacted more than dry samples at any given landmark in the experiment. Based on microstructure, for example, Figures 8 and 10, deforming gouge under wet conditions leads to more distributed cataclasis and a more significant reduction in grain size than when the same sample is deformed at the same normal stress but dry. This is likely due to the increased localization occurring during dry experiments, resulting in large low-strain domains and only local cataclasis. Alternative explanations include local overpressure, the Rehbinder effect, fault lubrication, or general water weakening (e.g., Noël et al. (2021), Noël, Fryer, et al. (2024)) leading to an increased ease in grain sliding; however, it may also be due to the period of sample wetting at the start of all wet experiments. Sample wetting is performed for 40 min at low normal stress (1 MPa), but the samples continuously compact during this time. Wet conditions further affect healing rate; however, whether or not healing is increased or decreased in wet conditions is sample dependent. Finally, note here that deionized water was used during the experiments and that pore-fluid chemistry can affect second-order friction characteristics (e.g., Carpenter, Collettini, et al. (2016)).

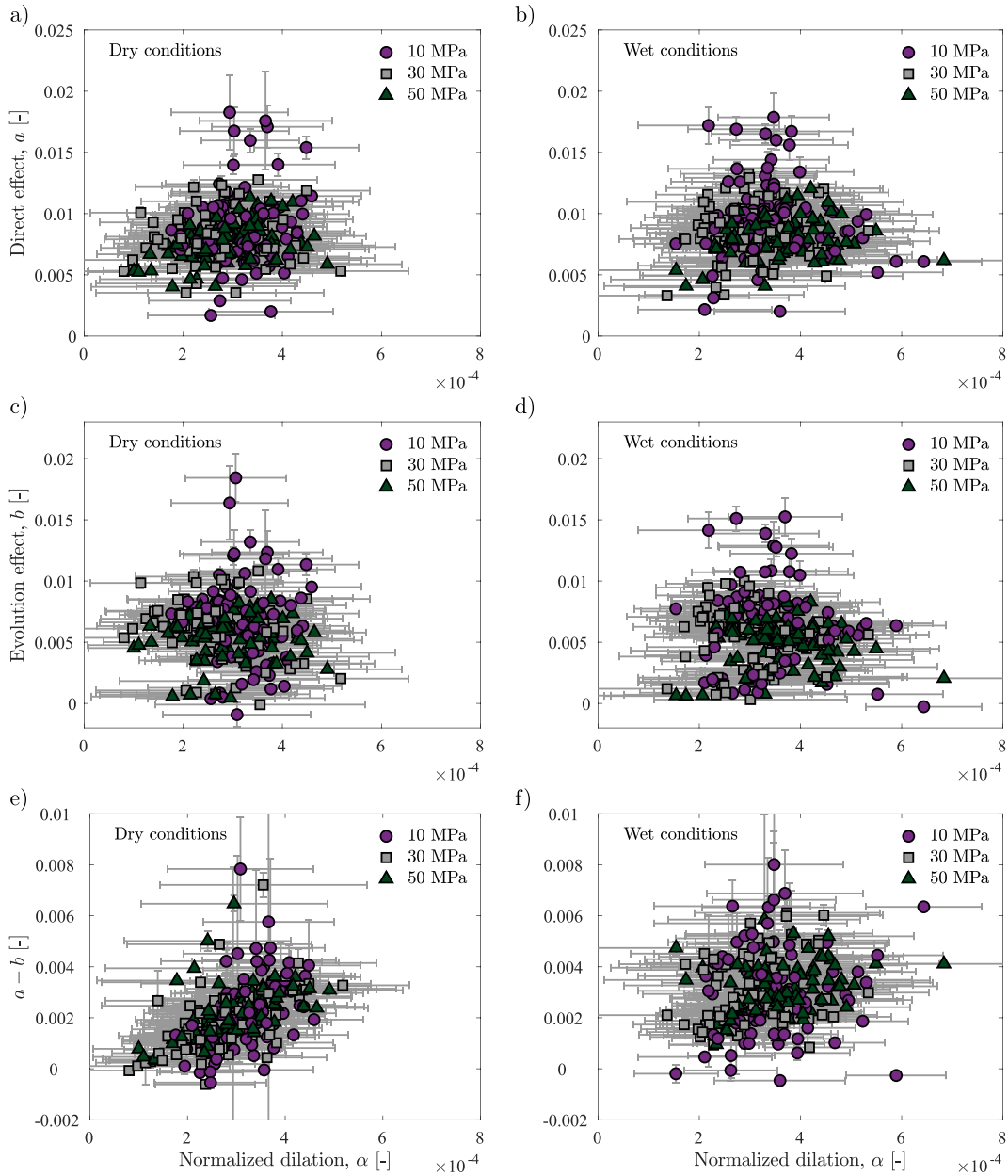

Figure 11. A demonstration of how $a - b$ scales with the normalized dilation upon a velocity step, α, for panels (a, c, e) dry and (b, d, f) wet conditions. The correlation between α and (a), (b) a, (c), (d) b, and (e), (f) $a - b$. It can be seen that the correlation between α and $a - b$ principally stems from α's correlation with a. The more a fault gouge must dilate to increase its sliding velocity the more velocity strengthening that gouge generally is. Velocity steps where either a or b was found to be above 0.02 were excluded because they were considered to be anomalous values related to difficulties in keeping a constant normal stress at high velocities.

6.5. The Influence of Phyllosilicate Content

The alteration of volcanic samples can lead to the existence of a variety of phyllosilicate minerals within the rock matrix. It has long been recognized that the presence of phyllosilicate minerals has a tendency to either mechanically or chemically reduce the frictional resistance of gouge samples, with initial work focusing on soils (Lupini et al., 1981; Skempton, 1964). More recently, a large number of authors have demonstrated this phenomenon for a wide variety of conditions, rock types, and gouge compositions (e.g., Summers and Byerlee (1977), Logan and Rauenzahn (1987), Moore et al. (1997), Morrow et al. (2000), Brown et al. (2003), Saffer

21699356, 2025, 2, Downloaded from https://agupubs.onlinelibrary.wiley.com/doi/10.1029/2024JB030213 by Cochrane France, Wiley Online Library on [28/01/2025]. See the Terms and Conditions (https://onlinelibrary.wiley.com/terms-and-conditions) on Wiley Online Library for rules of use; OA articles are governed by the applicable Creative Commons License

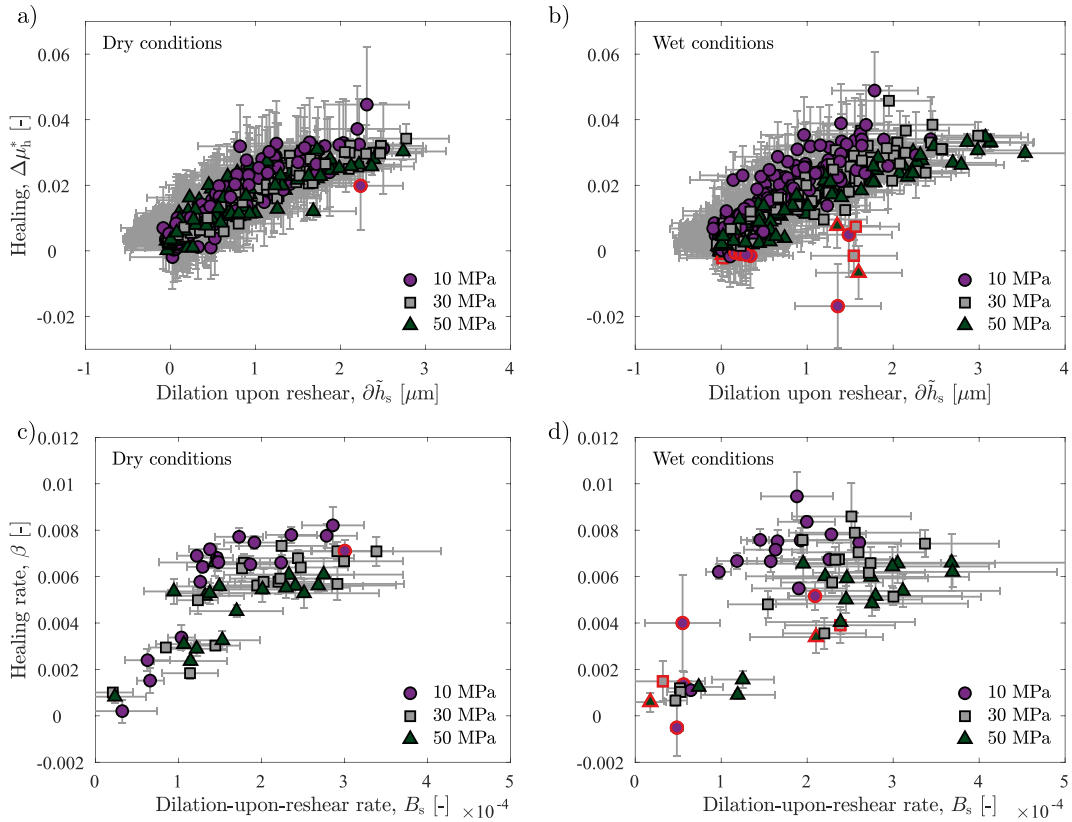

Figure 12. (a), (b) The healing, μ_h^*, versus the dilation upon reshear, $\partial\tilde{h}_s$, for holds performed in panels (a) dry and (b) wet conditions. In the case that the healing is negative (or represents a negative healing rate compared to smaller hold times), the data point is outlined in red. (c), (d) The healing rate, β, versus the dilation-upon-reshear rate, B_s, for experiments performed in panels (c) dry and (d) wet conditions. In the case that the healing becomes negative for large hold times, the data point is outlined in red.

and Marone (2003), Moore and Lockner (2004, 2007), Ikari et al. (2009), Tembe et al. (2010), Ikari et al. (2011), Saffer et al. (2012), Tesei et al. (2012), Giorgetti et al. (2015), Carpenter, Ikari, and Marone (2016), Fang et al. (2016), Zhang et al. (2022), Ashman and Faulkner (2023)). Additionally, the frictional healing (Bos & Spiers, 2000; Carpenter et al., 2011; Carpenter, Ikari, & Marone, 2016; Giorgetti et al., 2015; Ikari et al., 2016; Shreedhara et al., 2022; Tesei et al., 2012) and velocity-dependence (Giorgetti et al., 2015; Phillips et al., 2020; Summers & Byerlee, 1977) of gouge samples has been shown to be influenced by phyllosilicate content.

The strong influence of phyllosilicate content on frictional behavior and common occurrence of phyllosilicates in fault gouge have led to the questioning of the use of unaltered-rock or monomineralic friction results, without considering phyllosilicate content, to model natural fault gouge (Bos & Spiers, 2000). This may be particularly true for hydrothermal systems where alteration products are common. Indeed, all 18 samples collected here in situ contain phyllosilicates and other secondary minerals.

While the presence of phyllosilicates generally reduces frictional strength, decreases frictional healing, and promotes velocity-strengthening behavior, different phyllosilicate minerals produce these effects to a variety of degrees and magnitudes (Ikari et al., 2009; Moore et al., 1997; Moore & Lockner, 2004; Morrow et al., 1992, 2000; Summers & Byerlee, 1977). Despite this, direct comparisons between frictional parameters and the general phyllosilicate content have been performed on numerous occasions (e.g., Brown et al. (2003), Tembe et al. (2010), Tesei et al. (2012), Giorgetti et al. (2015)), and it has further been suggested by some authors that the overall phyllosilicate content controls the friction coefficient to a first order (Brown et al., 2003; Morrow et al., 1992; Saffer et al., 2012). Similarly, here, the dynamic friction coefficient is shown to be a first-order function of phyllosilicate content in andesite-like volcanic rocks from volcanic arc settings, despite the wide variety of

21699356, 2025, 2, Downloaded from https://agupubs.onlinelibrary.wiley.com/doi/10.1029/2024JB030213 by Cochrane France, Wiley Online Library on [28/01/2025]. See the Terms and Conditions (https://onlinelibrary.wiley.com/terms-and-conditions) on Wiley Online Library for rules of use; OA articles are governed by the applicable Creative Commons License

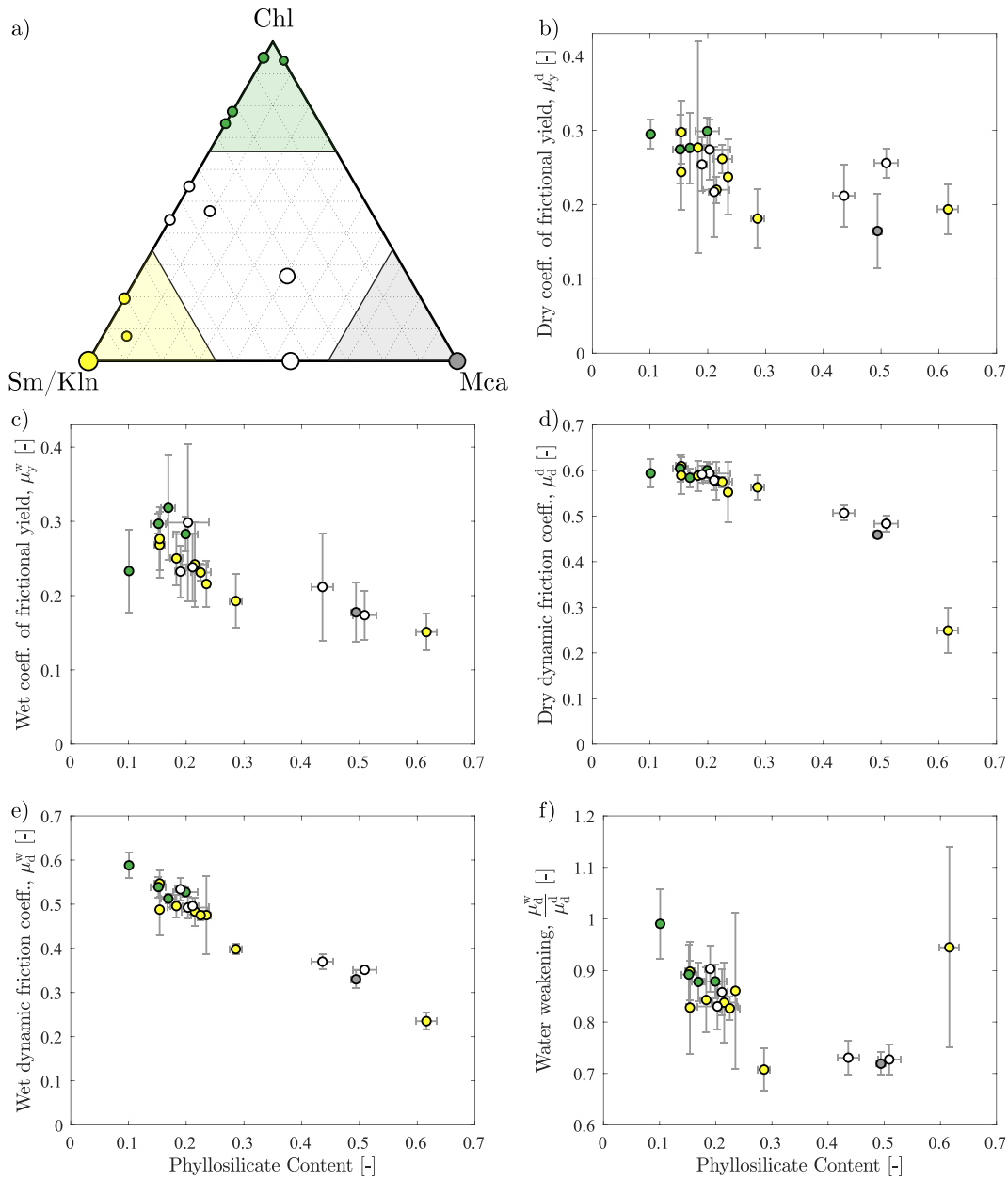

Figure 13. (a) A ternary diagram illustrating the relative proportions of phyllosilicate minerals, Table 2. For simplicity, 2:1 expandable clays, kaolinite, vermiculite are all grouped together in the category "Sm/Kln"; taken as representative of a smectite- and/or kaolinite-rich zone. Similarly, both dioctahedral and trioctahedral micas are grouped together in the "Mca" category; considered representative of the illite-rich zone, as illites are dioctahedral micas. "Chl" stands for chlorite. A sample is considered to belong to one of these three groups when when the relative proportion is greater than 0.67. Samples belonging to the Sm/Kln category are denoted with yellow points, those belonging to the Mca category with gray points, and those belonging to the Chl category with green points. Intermediate cases are left white. The marker size corresponds to the total phyllosilicate content. The (b) dry and (c) wet coefficients of frictional yield. The (d) dry and (e) wet coefficients of dynamic friction as a function of phyllosilicate content for all samples. The coefficients of dynamic friction are calculated as demonstrated in Figure 4. (f) The water-induced frictional-strength reduction of the dynamic friction coefficient as a function of the phyllosilicate content.

mineralogies of the samples, Figure 13. It should be noted that, as shown by other workers mentioned above, different phyllosilicate minerals are still expected to have different influences on the friction characteristics of a given gouge. The emphasis here is on the first-order behavior, with a view to simplify engineering and hazard studies. A less clear trend is also present for the coefficient of frictional yield. The weakening with increased

21699356, 2025, 2, Downloaded from https://agupubs.onlinelibrary.wiley.com/doi/10.1029/2024JB030213 by Cochrane France, Wiley Online Library on [28/01/2025]. See the Terms and Conditions (https://onlinelibrary.wiley.com/terms-and-conditions) on Wiley Online Library for rules of use; OA articles are governed by the applicable Creative Commons License

21699356, 2025, 2, Downloaded from https://agupubs.onlinelibrary.wiley.com/doi/10.1029/2024JB030213 by Cochrane France, Wiley Online Library on [28/01/2025]. See the Terms and Conditions (https://onlinelibrary.wiley.com/terms-and-conditions) on Wiley Online Library for rules of use; OA articles are governed by the applicable Creative Commons License

phyllosilicate content is present in both wet and dry conditions, but is more significant in wet conditions. Generally, the higher the phyllosilicate content the larger the difference in weakening between wet and dry conditions, as seen by other authors (Morrow et al., 1992). This trend may reverse for very large phyllosilicate contents (>0.6), Figure 13f, but it is also likely that the nominally dry samples at such high phyllosilicate contents are sufficiently wet (due to, for example, room humidity) to behave as (partially) wet samples.

Further, as seen by previous workers in other rock types and gouge compositions (Fang et al., 2016; Ikari et al., 2007, 2009, 2011, 2016; Logan & Rauenzahn, 1987; Niemeijer & Spiers, 2006; Tembe et al., 2010; Zhang et al., 2022), the velocity dependence of these andesitic-like volcanic arc samples is affected by phyllosilicate content, Figure 14. The direct effect, a, slightly decreases with increased phyllosilicate content, but the evolution effect, b, decreases significantly. Overall this results in an increase in $a - b$ and therefore increased velocity-strengthening behavior. A decrease in b has been previously associated with a transition from brittle to "semi-brittle" behavior (Carpenter, Collettini, et al., 2016). The dilation that occurs during a velocity step also generally decreases with increasing phyllosilicate content, similar to previous observations (Ashman & Faulkner, 2023).

Additionally, as shown previously in other rock types (Bos & Spiers, 2000; Carpenter et al., 2011; Carpenter, Ikari, & Marone, 2016; Ikari et al., 2016; Shreedhara et al., 2022; Tesei et al., 2012), the healing rate is reduced in samples with higher phyllosilicate contents, Figure 15. As seen by Bos and Spiers (2000), dilation upon reshear is reduced for higher phyllosilicate contents and might be related to observations of permeability decrease during shear slip in phyllosilicate-rich crystalline samples (Meng et al., 2022).

While difficult to constrain precisely, it seems that phyllosilicate content begins having a significant influence on frictional behavior at weight contents larger than approximately 20%. Previous operators, in a variety different geological contexts, have reported a range of values for the onset of a significant influence of phyllosilicate content. Giorgetti et al. (2015) reported that as little as 5% talc content was already enough to significantly influence the behavior of talc-calcite mixtures; whereas Brown et al. (2003) report behavior similar to that reported here for samples relevant to subduction zones. Similar results were also reported by Tembe et al. (2010) for quartz-clay mixtures. Tesei et al. (2012) report a still higher value of phyllosilicate content, albeit with a more stringent criterion for weakening. While a relative independence of first- and second-order frictional behavior on the specific phyllosilicate mineral is generally shown here, this data set lacks a sample with a large (>40% by weight) amount of chlorite, such that phyllosilicate-mineral-specific behavior may appear for highly altered chlorite-rich samples. Additionally, it should be noted that while the temperature independence of first-order friction characteristics is accepted at low (<300°C) temperatures (e.g., Scholz (2019), ch. 2), second-order friction characteristics are often dependent on temperature (e.g., Blanpied et al. (1991), Kolawole et al. (2019), Jeppson et al. (2023)).

The evolution effect, b, in the measurement of the velocity-dependence of friction reflects the evolution and renewal of contact area (Dieterich, 1979; Ikari et al., 2016; Scholz, 2019). As shown here and elsewhere, phyllosilicate-rich rocks often exhibit very low, or even negative, values of b (Ikari et al., 2009, 2016; Saffer & Marone, 2003). This is because clay gouge particles are in complete contact and the contact area does not change upon a step in velocity (Ikari et al., 2016; Saffer & Marone, 2003). Interestingly, however, it has been shown here that phyllosilicate-rich gouge can also exhibit negative healing, likely due to either (a) the saturation and even reduction of real contact area during periods of very low slip velocities (during the hold periods of slide-hold-slides the stress reduction is due to slip, despite the far field slip rate being maintained at zero (Marone, 1998)), or (b) due to a reduction in the quality of contacts, for example, through the development of a preferred orientation. Although the sliding velocities during the velocity steps performed here and by other operators are too high for this effect to be evident during laboratory velocity steps (the time scale of contact renewal due to slip is shorter than the time scale for contact area/quality reduction), tectonic strain rates are orders of magnitudes lower and may be more comparable to the slip rate during slide-hold-slide holds. It may be that, at tectonic strain rates, these phyllosilicate-rich samples would undergo contact area/quality reduction as far-field stresses cause mineral reorientation. Depending on relative time scales between contact area reduction and contact resaturation during slip, it may be therefore that - at very low strain rates - these samples exhibit higher values of b than those measured in the laboratory, potentially leading to velocity weakening at tectonic strain rates. Indeed, bulk rate-strengthening phyllosilicate-rich samples have recently been connected to slow-slipping earthquakes (Volpe et al., 2024). We caution that this phenomenon, while plausible, is highly speculative.

21699356, 2025, 2, Downloaded from https://agupubs.onlinelibrary.wiley.com/doi/10.1029/2024JB030213 by Cochrane France, Wiley Online Library on [28/01/2025]. See the Terms and Conditions (https://onlinelibrary.wiley.com/terms-and-conditions) on Wiley Online Library for rules of use; OA articles are governed by the applicable Creative Commons License

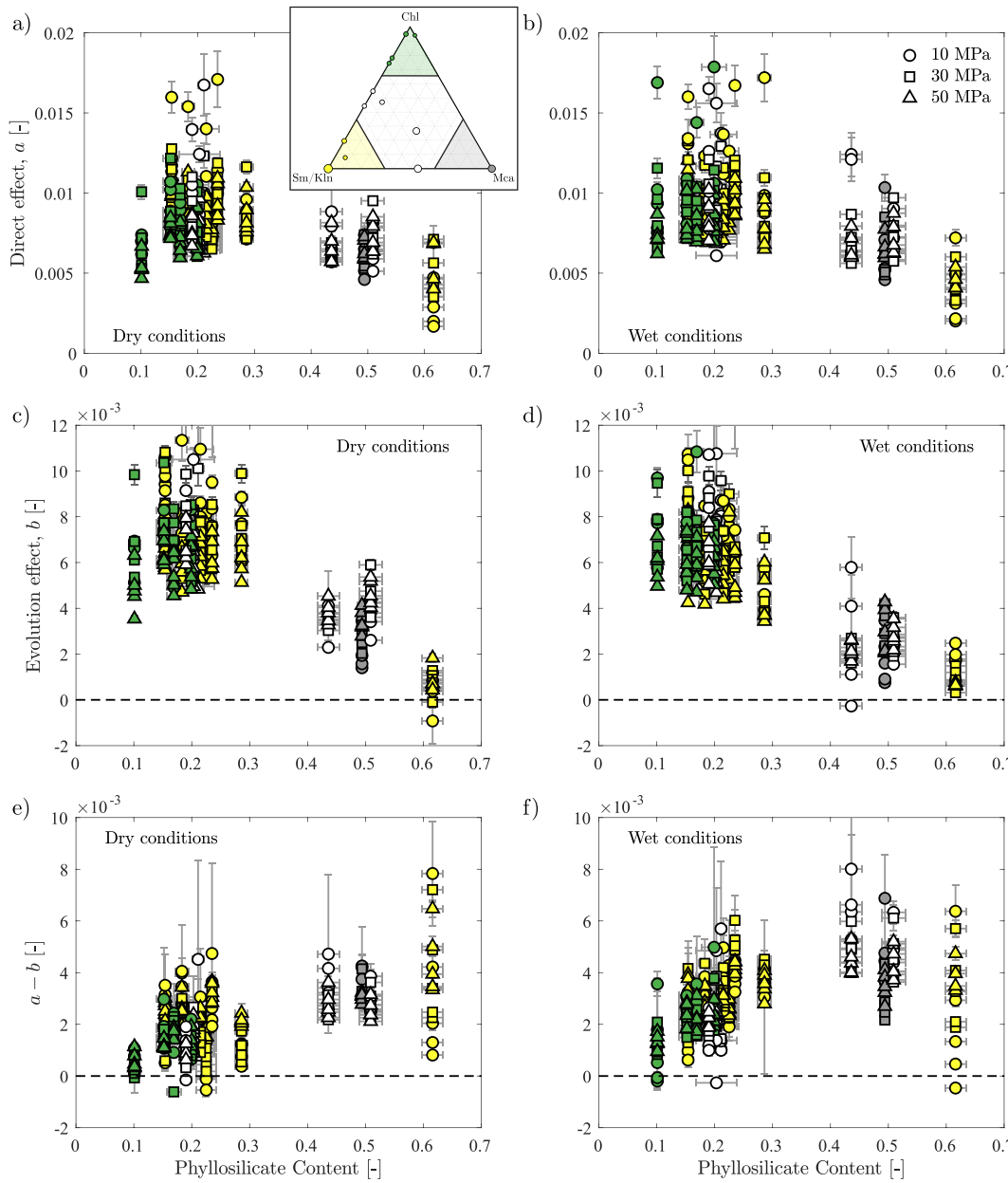

Figure 14. The velocity dependence as a function of the phyllosilicate content of each sample. The normal stress of each point is indicated by the shape of the marker. (a), (b) The direct effect, *a*. (c), (d) The evolution effect, *b*. (e), (f) The velocity dependence, $a - b$. The results are shown for dry (a, c, e) and wet (b, d, f) experiments. Points are colored in accordance with Figure 13a (repeated as an inset here in panel (a)), where yellow is representative of the smectite/kaolinite zone, gray of the illite-rich zone (illites are dioctahedral micas), green of the chlorite-rich zone, and white is intermediate between two or more zones.

6.6. Implications

6.6.1. Geothermal Reservoirs

Geothermal reservoirs in volcanic arc settings often have a general, albeit simplified, structure consisting of, from shallowest to deepest, a smectite-kaolinite zone, an illite-rich zone, a chlorite-rich zone, and finally a ductile shear zone (Cathelineau & Izquierdo, 1988; Stimac et al., 2015; Verati et al., 2018). Examples of this hydrothermal alteration pattern, either in part or in full, include Bouillante, France (Beauchamps et al., 2019), Terre-de-Haut, France (Beauchamps et al., 2019), the Ogiri Field, Japan (Goko, 2000), Pauzhetskoe geothermal field, Russia

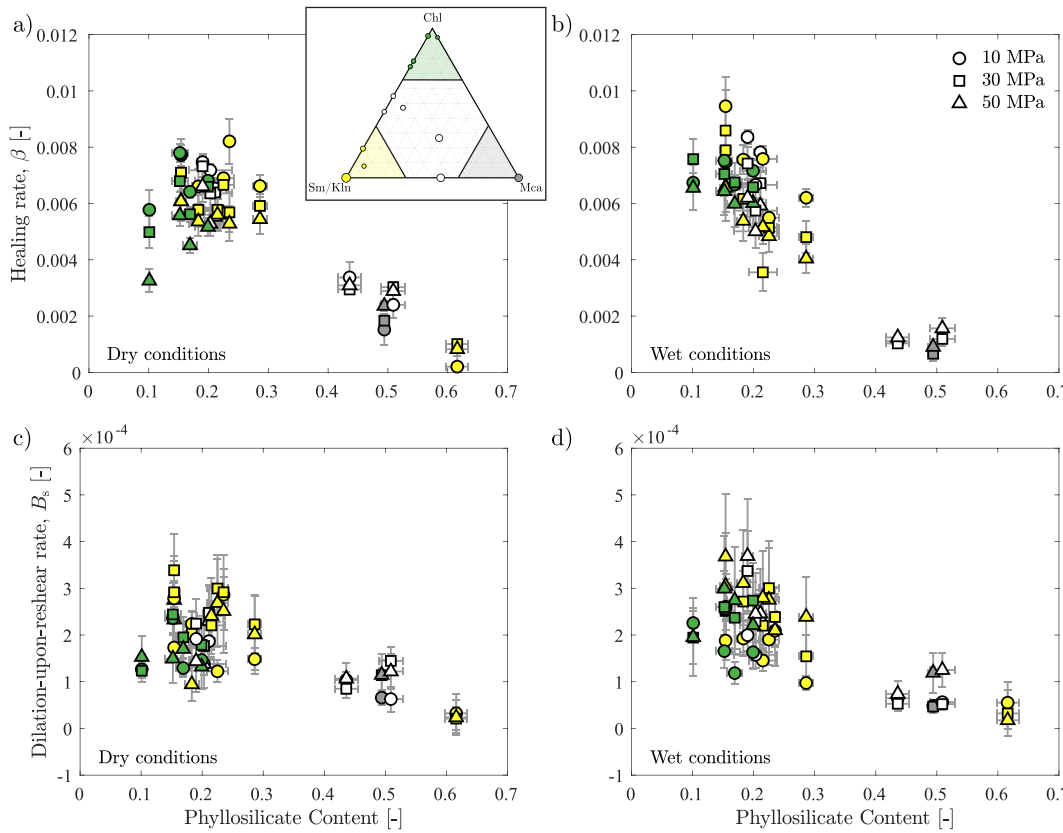

Figure 15. (a), (b) The frictional healing rate, β, as a function of the phyllosilicate content of each sample in both dry (a) and wet (b) conditions. Note that experiments which exhibited negative healing rates for longer holds are not plotted here. (c), (d) The dilation-upon-reshear rate as a function of phyllosilicate content for dry (c) and wet (d) conditions. Points are colored in accordance with Figure 13a (repeated as an inset here in panel (a)), where yellow is representative of the smectite/kaolinite zone, gray of the illite-rich zone, green of the chlorite-rich zone, and white is intermediate between two or more zones.

(Frolova et al., 2006), Okeanskoe geothermal field, Russia (Frolova et al., 2006), the Cophaue geothermal reservoir, Argentina (Barcelona et al., 2019; Yagupsky et al., 2023), Darajat, Indonesia (Rejeki et al., 2010), Cerro Pabellón, Chile (Maza et al., 2018), Tolhuaca, Chile (Melosh et al., 2010; Sanchez-Alfaro et al., 2016), Mount Meager, Canada (Hormozzade Ghalati et al., 2023), and the Awibengkok Geothermal System, Indonesia (Stimac et al., 2008). The literature also contains examples of ductile shear zones acting as vertical fluid barriers (Stimac et al., 2015; Yagupsky et al., 2023) and horizontal fluid conduits (Favier, Lardeaux, Corsini, et al., 2021; Favier, Lardeaux, Verati, et al., 2021). The samples tested here can provide insight into the likely frictional properties of the smectite- and kaolinite-rich, illite-rich, and chlorite-rich zones. In particular, samples B494D, S491I, LA03749, N3808, and N3583 are likely representative of smectite- and kaolinite-rich zones, sample S491B is likely representative of illite-rich zones. G3130 may represent chlorite-rich zones, although the degree of alteration is somewhat low compared to previously listed examples. LA02541, LA02422, M1430, and N4343 may represent mixed or transitional layers, with multiple types of alteration present. Other samples may be interpreted to represent these zones in cases where the alteration is less developed.

The frictional properties of the samples have been shown to depend, to a first order, on the general phyllosilicate contents of the samples. It is therefore not expected that the different zones mentioned above have significantly different frictional properties based solely on their relative phyllosilicate compositions. This should facilitate the numerical modeling of frictional phenomena in these regions; however, a given geothermal system may have different propensities for producing certain alteration minerals, meaning that high phyllosilicate contents may be more or less likely to be found in a given zone resulting in differing frictional properties depending on the zone being modeled.

21699356, 2025, 2, Downloaded from https://agupubs.onlinelibrary.wiley.com/doi/10.1029/2024JB030213 by Cochrane France, Wiley Online Library on [28/01/2025]. See the Terms and Conditions (https://onlinelibrary.wiley.com/terms-and-conditions) on Wiley Online Library for rules of use; OA articles are governed by the applicable Creative Commons License

21699356, 2025, 2, Downloaded from https://agupubs.onlinelibrary.wiley.com/doi/10.1029/2024JB030213 by Cochrane France, Wiley Online Library on [28/01/2025]. See the Terms and Conditions (https://onlinelibrary.wiley.com/terms-and-conditions) on Wiley Online Library for rules of use; OA articles are governed by the applicable Creative Commons License

The ductile shear zones which provide lateral fluid transport in these settings can only occur when the primary mode of deformation is delocalized or, equivalently, ductile (e.g., Rutter (1986), Knipe and McCaig (1994), Meyer and Violay (2023)). For this to occur, the bulk yield stress of a given rock mass as it experiences a far-field stress must be lower than its frictional strength. As the frictional strength has been shown here and elsewhere to be dependent on the phyllosilicate content of the rock, the localized-to-ductile transition (LDT) is predicted to be dependent on the phyllosilicate content (e.g., Koroknai et al. (2008)), and therefore alteration, of the in situ rock, Figure 16. While increasing phyllosilicate content lowers the frictional strength of fault gouge, it is not necessarily the case that the LDT will occur at a greater stress (and therefore greater depth). Indeed, it may be that the higher the phyllosilicate content the lower the yield stress of the rock. However, there is currently no systematic study of the impact of phyllosilicates on the yield (onset of yield) of volcanic rocks, and the effect of phyllosilicate content on bulk yield stress (which can be expected to be temperature dependent) was only tested here at room temperature. Yet, the LDT depends on the competition between the frictional strength and the yield stress of the material. Hence, despite the apparent decrease in frictional yield coefficient with increasing phyllosilicate content (and supporting microstructural observations), we are unable to assess the relative impact of clays on frictional strength and bulk yield stress at reservoir conditions and therefore unable to assess whether the LDT will shift to shallower or greater depths with increasing alteration. It should be noted, however, that alteration resulting in an increased proportion of phyllosilicate minerals has been suggested as a mechanism resulting in a shallower brittle-ductile transition along tectonic faults (Imber et al., 2001; Shea & Kronenberg, 1992).

The alteration of a given zone is reliant on the ability of hydrothermal fluids to reach that zone, typically through fluid conduits such as faults and fractures. It is therefore possible that certain zones of a given reservoir remain fairly unaltered. This can be seen, for example, in the samples from Lamentin where the relatively unaltered LA03758 occurs in close proximity to the highly altered LA03749, or in the Tolhuaca-1 wellbore in the Tolhuaca Geothermal Field (Melosh et al., 2010). As these reservoirs occur in regions which are tectonically active and likely critically stressed, it can be thought that the stress present in a given reservoir horizon will depend on the frictional resistance of that horizon (e.g., Harrison et al. (1954), Brudy et al. (1997), Townend and Zoback (2000), Zoback and Townend (2001), Zoback et al. (2002), Evans et al. (2012)). Therefore, zones which are frictionally weak will be able to support smaller differential stresses. An implication of this idea is the prediction that, in normal-faulting stress regimes (where the maximum principal stress is fixed by the overburden), such as that recently active in Les Saintes (Verati et al., 2016), the minimum principal stress will be larger in phyllosilicate-rich zones and smaller in unaltered zones if the environment is critically stressed, leading to the formation of stress jumps when altered and unaltered zones are vertically adjacent, Figure 16. This has been previously implied for the Soultz-sous-Forêts reservoir (Meller & Kohl, 2014), albeit in a different tectonic setting. While stress jumps have been observed and measured in a number of instances, particularly in sedimentary basins (e.g., Kry and Gronseth (1983), Teufel (1989), Lucier et al. (2006), Wileveau et al. (2007)), to the authors' knowledge they have not yet been observed in a volcanic-arc setting in igneous rock. The presence of a stress jump would have significant influence on natural and induced fracture propagation and containment, as a jump in minimum principal stress can significantly inhibit a propagating fracture (e.g., Adachi et al. (2010)).

In summary, it can be expected that, for geo-reservoirs in volcanic arc settings, the degree of alteration controls (a) the ability of faults within and around the reservoir to nucleate seismic slip (by influencing their velocity dependence; i.e., $a - b$) as well as their sliding strength (μ_d) and strength recovery (β), (b) the depth of ductile shear zones, which are crucial for the horizontal movement of fluid, and (c) the vertical propagation of natural and induced fractures through phyllosilicate content's influence on the minimum principal stress.

6.6.2. Seismicity in Volcanic Arcs

Volcanic arcs are found in areas of active plate tectonics and are therefore likely to be seismically active regions. For example, a significant number of on- and off-shore faults in the Guadeloupe archipelago are seismically active and are thought to control the volcanic activity, fluid flow, and superficial earthquakes in the area (Verati et al., 2016). The results presented here can be used to help with the understanding of active volcanoes, where alteration has been previously suggested to potentially lead to explosive volcanic behavior by reducing the permeability of pore and micro-fracture pathways (Heap et al., 2019).

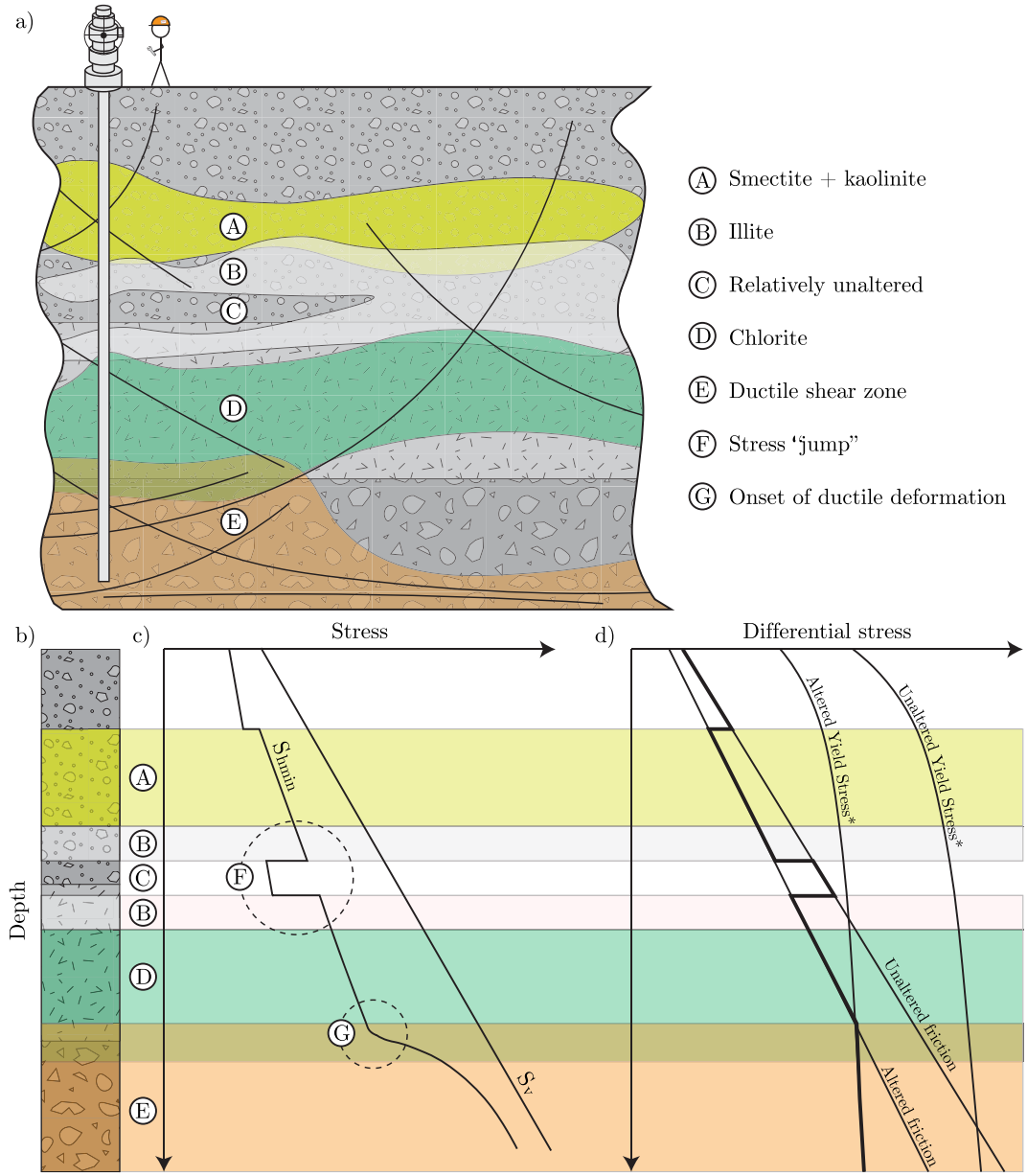

Figure 16. An example stress profile and localized-ductile transition resulting from the alteration profiles of a hypothetical geothermal reservoir in a volcanic arc setting. (a) A cross-section illustrating the wellpath and the alteration zones present. (b) The example stratigraphic profile comprised of (A) a smectite-kaolinite-rich zone, (B) an illite-rich zone, (C) an unaltered zone, (D) a chlorite-rich zone, and (E) a ductile shear zone. Note the faults/fractures represented by black curved lines. The presence of these fluid conduits allows for alteration to occur in these zones. The unaltered zone, which may be equivalently present within the clay cap or chlorite-rich zone, is a result of the lack of faults and fractures crossing this zone. Further note that the ductile shear zone does not necessarily coincide with the end of the chlorite-rich zone. (c) The stress profile in a normal-faulting stress regime. The vertical stress increases linearly with depth. As these zones are often critically stressed, the magnitude of the minimum horizontal stress depends on the friction coefficient. In altered zones, phyllosilicate content is high and the differential stress is low. This may result in stress jumps (F). The onset of the localized to ductile transition will result in a relative increase in the minimum horizontal stress (G). (d) The differential stress as a function of depth based on frictional strength and yield stress of each zone. The ductile to localized transition begins when the frictional strength is larger than the yield stress (Meyer et al., 2019; Rutter, 1986). The frictional strength of the rock has been shown here to depend on the phyllosilicate content, meaning alteration may affect the depth of the localized-to-ductile transition and therefore the depth of the ductile shear zone and its proximity to the acting geothermal reservoir. Note that the yield stresses of the samples were not measured here at reservoir conditions and likely also depend on alteration.

21699356, 2025, 2, Downloaded from https://agupubs.onlinelibrary.wiley.com/doi/10.1029/2024JB030213 by Cochrane France, Wiley Online Library on [28/01/2025]. See the Terms and Conditions (https://onlinelibrary.wiley.com/terms-and-conditions) on Wiley Online Library for rules of use; OA articles are governed by the applicable Creative Commons License

21699356, 2025, 2, Downloaded from https://agupubs.onlinelibrary.wiley.com/doi/10.1029/2024JB030213 by Cochrane France, Wiley Online Library on [28/01/2025]. See the Terms and Conditions (https://onlinelibrary.wiley.com/terms-and-conditions) on Wiley Online Library for rules of use; OA articles are governed by the applicable Creative Commons License

Further, geothermal projects are often concerned with induced seismicity. For example, a risk assessment related to induced seismicity has been commissioned for the Newberry EGS Demonstration project (Wong et al., 2010). The frictional data presented here suggest that zones which are highly altered and rich in phyllosilicates are less likely to produce a large seismic event, despite being frictionally weak (Fang et al., 2016; Meller & Kohl, 2014). However, slip induced in these zones may act to transfer stress to a stronger, less-altered patch of a given fault. In general, care should be taken to contain the footprint of a given operation to as small a region as possible within a phyllosilicate-rich zone. This not only means limiting pore pressure increases to a small region, but also ensuring that aseismic-slip and thermo- and poro-elastic stress changes associated with fluid injection and stress transfer due to fault slip are also constrained.

7. Conclusion

The frictional properties of 18 core and surface samples from five geothermal reservoirs in volcanic arc settings have been explored through 108 biaxial experiments. It has been shown that, despite the previously demonstrated differences in the frictional behavior of different phyllosilicate minerals in monomineralic experiments, the overall combined phyllosilicate content controls the frictional behavior in these settings to a first order. This simplification may facilitate the numerical modeling of these geothermal reservoirs which often have stratified alteration zones in which different phyllosilicate minerals dominate. Specifically, larger phyllosilicate contents result in reduced frictional strength, an increased tendency for velocity-strengthening behavior, and reduced frictional healing. Further, negative healing was observed, in particular in one sample which was rich in calcite and 2:1 expandable trioctahedral clays under wet conditions (deionized water), and warrants further investigation. The faults and fracture networks which make up these reservoirs are often rooted in ductile shear zones, crucial for the horizontal advection of geothermal fluids, and it is suggested here that the depth of onset for these zones will depend on the level of alteration and may therefore shift in time as alteration continues. Finally, the critically stressed nature of these reservoirs and the varying degrees of alteration in their constituent horizons implies that stress jumps may develop, with important implications for fracture propagation.

Appendix A: Field Histories

A1. Les Saintes

The western coast of Basse Terre on the island of Guadeloupe presents a number of hydrothermal expressions near the town of Bouillante, including hot springs, mud pools, steaming ground, and fumaroles (Correia et al., 2000). This led to geothermal exploration of the area by the BRGM in the 1960's (Jaud & Lamethe, 1985) and ultimately the drilling of four exploration wells by Eurafrep and la Société de Production d'Electricité de Guadeloupe (SPDEG) between 1969 and 1977 (Jaud & Lamethe, 1985). These wells encountered high-temperature conditions (approximately 245^{o}C), but only one well (BO-2) showed potential for economical steam production (Correia et al., 2000; Jaud & Lamethe, 1985). Two other wells were plugged and a fourth, deeper well (BO-4) was deemed to have too low of a productivity to warrant production (Correia et al., 2000). Initially, only BO-2 was connected to a 4.7 MWe-capacity power plant which was brought online in 1987 (Correia et al., 2000). Following a slight decline in production from BO-2, BO-4 was stimulated with the injection of cold fluid; while the area was monitored for induced seismicity during the stimulation activities, no seismic events were recorded (Correia et al., 2000). In 2001, three further wells were drilled from the platform of BO-4. Two of these wells (BO-5 and BO-6) were connected to a new geothermal power plant, raising the productivity of the field to 15 MWe (Mas et al., 2006). The geothermal field is comprised of predominately andesitic volcanic horizons (Bouchot et al., 2010), and is considered to be located at the junction between a major transcurrent fault and a perpendicular network of steeply dipping normal faults (Navelot et al., 2018; Verati et al., 2014).

Les Saintes is an island archipelago of Guadeloupe located South of Basse Terre, Figure A1. One of its principal islands, Terre-de-Haut, is considered to contain outcrops which represent an exhumed geothermal paleo-system, active between 2.4 and 2.0 Ma, which may act as an analog for the modern-day Bouillante geothermal reservoir (Favier, Lardeaux, Verati, et al., 2021; Navelot et al., 2018; Verati et al., 2016). While there have been no exploration wells drilled in this area, it is thought that the paleo-gradient was likely in the range of 90–140 $\frac{^{o}C}{km}$, with the deepest part of the paleo-reservoir at approximately 2.5 km (Favier, Lardeaux, Verati, et al., 2021). The

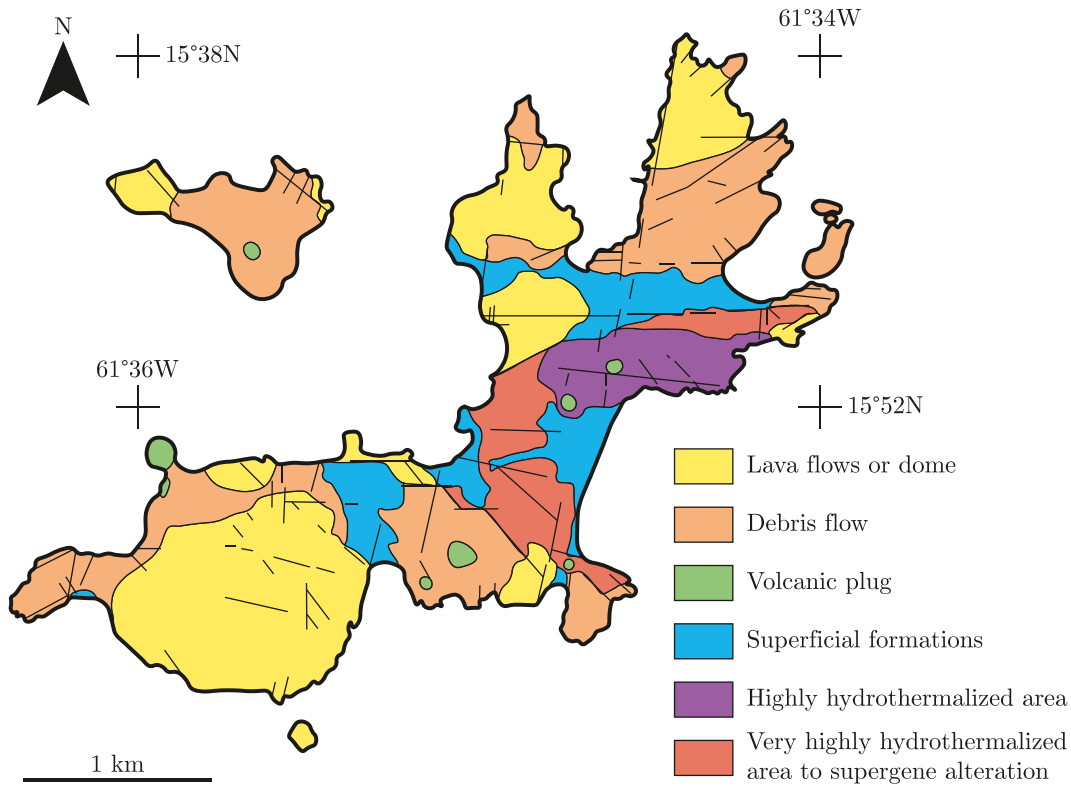

Figure A1. A geological map of Terre-de-Haut; modified from Favier, Lardeaux, Verati, et al. (2021). Les Saintes samples are taken from the central very highly hydrothermalized area.

present day geothermal gradient of the area is not known, but near the Gaudeloupe archipelago a gradient in the range of 69–98 $\frac{^{\circ}C}{km}$ may be considered reasonable (Manga et al., 2012).

A2. Lamentin

The presence of thermal springs in the area of Le Lamentin motivated a first geothermal exploration phase in the late 1960s (Gadalia et al., 2014), with a relatively deep exploration well, LA-101, drilled in 1970 to a depth of 771 m; this well presented a maximum temperature of approximately 90ºC at 250 m depth (Genter et al., 2002). Subsequent surface investigations and drilling programs in the 1980's and early 2000's further explored the area (Gadalia et al., 2014). In particular, three exploratory wells were drilled in 2001 by the Compagnie Française de Géothermie (CFG) with the goal of investigating the possibility of developing a high-enthalpy reservoir at depth and to improve the data coverage of the existing geothermal reservoir between 200 and 400 m depth (Genter et al., 2002). Accompanying this drilling program was a scientific program headed by the Bureau de Recherches Géologiques et Minières (BRGM) (Sanjuan, Genter, et al., 2002). Ultimately, this exploration program found that there was no major evidence of a high-temperature geothermal reservoir. However, while this system is a low-temperature hydrothermal system with a maximum recorded temperature of approximately 90ºC, evidence (such as clay mineral structure, for example) of a fossil high-temperature system is present (Genter et al., 2002; Mas et al., 2003). Additionally, while there are currently no active geothermal wells at Lamentin, a new round of investigations has begun to probe key uncertainties regarding the geothermal system with the hope of updating its conceptual model and proposing new sites for exploration (Gadalia et al., 2019). To this end, cores from two of the three exploration wells drilled in the early 2000's are used in this study, Figure A2.

The Habitation Carrère well, also known as LA02, was drilled in an area of thermal springs. The drilling was performed in a destructive manner until a depth of 386.7 m after which the well was cored to a depth of 816.15 m (Genter et al., 2002; Mas et al., 2003). LA02422 comes from a permeable zone characterized by mud losses

21699356, 2025, 2, Downloaded from https://agupubs.onlinelibrary.wiley.com/doi/10.1029/2024JB030213 by Cochrane France, Wiley Online Library on [28/01/2025]. See the Terms and Conditions (https://onlinelibrary.wiley.com/terms-and-conditions) on Wiley Online Library for rules of use; OA articles are governed by the applicable Creative Commons License

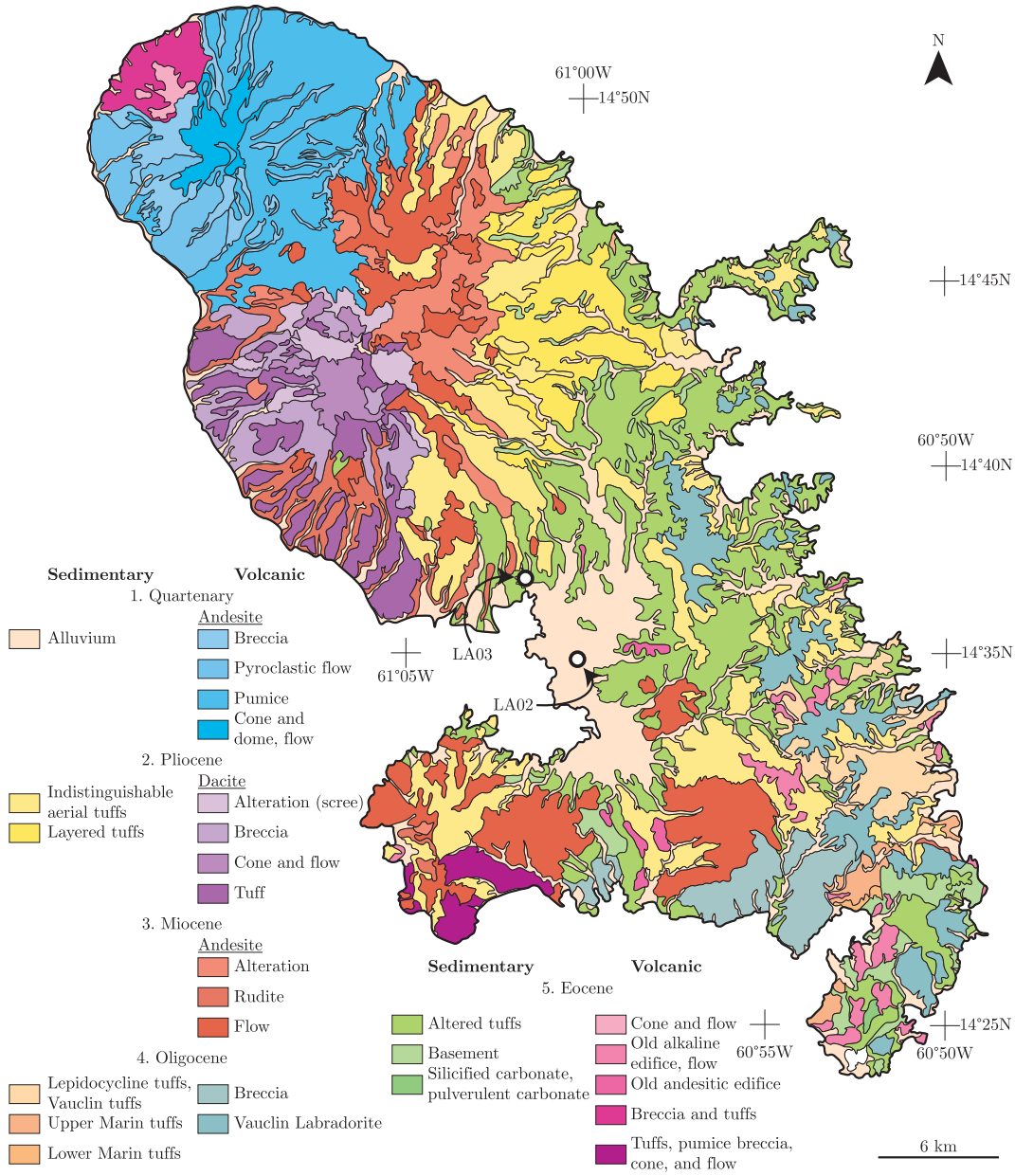

Figure A2. A geological map of Martinique with the locations of the wells LA02 and LA03 marked; modified from IRD (2014), Zaiss (2014). Well locations from Sanjuan, Traineau, et al. (2002), Mas et al. (2003).

(between the depths of 412 and 428 m) which is also considered to be one of the main aquifers of this well (Genter et al., 2002; Sanjuan, Traineau, et al., 2002). The bottom hole temperature of this well was 47°C at the time of measurement. Further measurements at 100 m and 350–375 m indicate temperatures of 40°C and 50°C, respectively (Genter et al., 2002).

The Californie Well, also known as LA03, was drilled destructively to 398.14 m and then cored to 1,000.25 m (Genter et al., 2002). The maximum temperature of this well is thought to be 88°C at around 400 m depth; temperature below this depth is slightly lower, with a bottom-hole temperature reading of 83°C at 997 m (Genter

21699356, 2025, 2, Downloaded from https://agupubs.onlinelibrary.wiley.com/doi/10.1029/2024JB030213 by Cochrane France, Wiley Online Library on [28/01/2025]. See the Terms and Conditions (https://onlinelibrary.wiley.com/terms-and-conditions) on Wiley Online Library for rules of use; OA articles are governed by the applicable Creative Commons License

et al., 2002). The formations encountered by this well are more permeable but less fractured than those in the Carrère well (Genter et al., 2002).

A3. Mount Meager

In the Mount Meager area, the Meager Creek Hot Springs were first drilled in 1974 as part of a scientific project aimed at investigating local thermal springs (Jessop, 2008). These initial shallow wells then led to the drilling of deeper exploration wells in the early 1980's. These wells encountered temperatures sufficient for a producing geothermal system (approximately 290°C at 3,000 m), but the flow rates were deemed insufficient for economic power production (Jessop, 2008). Further drilling occurred in the 1990's and 2000's, including three cored holes drilled in 2001 and 2002. One of these cored holes, M-17, Figure A3, was drilled to a total depth of 1,186 m and exhibited a maximum temperature of 197°C at 1,100 m depth (Jessop, 2008). The other two wells both recorded temperatures of over 200°C (Jessop, 2008). Despite these results, and further deeper drilling in the mid-2000's, power production never materialized beyond a pilot geothermal power facility. Interest has recently been renewed in Mount Meager, however, with Geoscience BC and the Geological Survey of Canada commissioning a study to

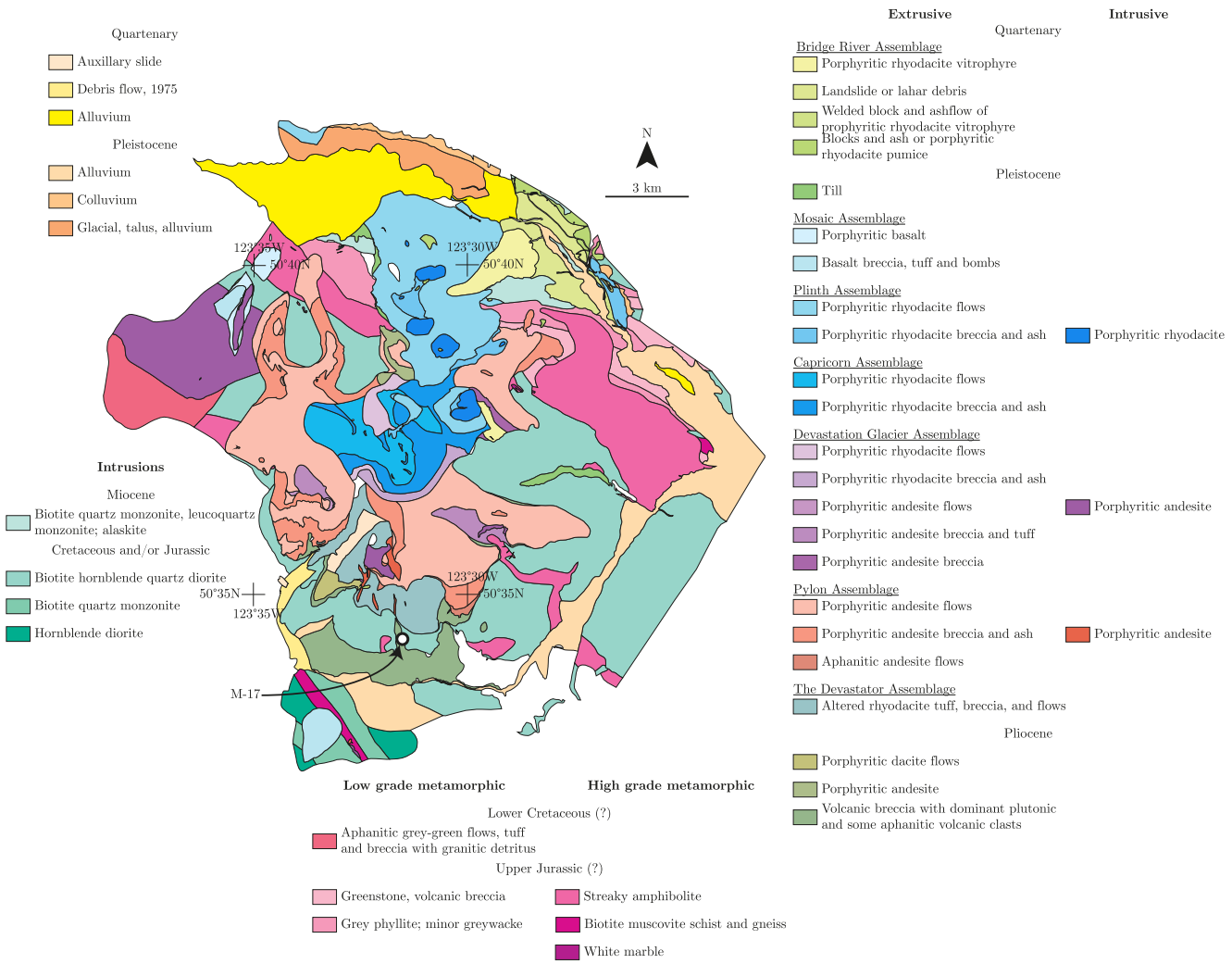

Figure A3. A geological map of Meager Creek Geothermal Area with the location of the well M-17 marked; modified from Read (1979). Well location from Ghomshei et al. (2004).

21699356, 2025, 2, Downloaded from https://agupubs.onlinelibrary.wiley.com/doi/10.1029/2024JB030213 by Cochrane France, Wiley Online Library on [28/01/2025]. See the Terms and Conditions (https://onlinelibrary.wiley.com/terms-and-conditions) on Wiley Online Library for rules of use; OA articles are governed by the applicable Creative Commons License

reduce exploration risk for geothermal energy associated with volcanic systems of Canada (Grasby et al., 2020; Hormozzade Ghalati et al., 2023).

A4. Summerland Basin

In 1990, the EPB/GSC495 well was drilled to a depth of 712 m in the Summerland Basin, Figure A4, being cored from 544 to 712 m (Church et al., 1990; Jessop, 2008). This well was extended and cored in 1992 to a depth of 956 m (Jessop, 2008). The original purpose of this wellbore was exploratory geothermal research; however the highest temperature recorded in the well was approximately 41°C at 946.5 m (Jessop, 2008). Although the temperatures measured were sufficient for the low-temperature geothermal system proposed, no useable water was found and the project was largely abandoned (Jessop, 2008). The cores have since been stored at the Geological Survey of Canada - Calgary core storage facility. Indeed, this region has long been thought to be a potential geothermal resource (e.g., Jessop (2008) and references within), and, with renewed interest in geothermal energy, British Columbia is being revisited with an aim to reduce the exploration risk for geothermal resources associated with volcanic systems (e.g., Grasby et al. (2022)).

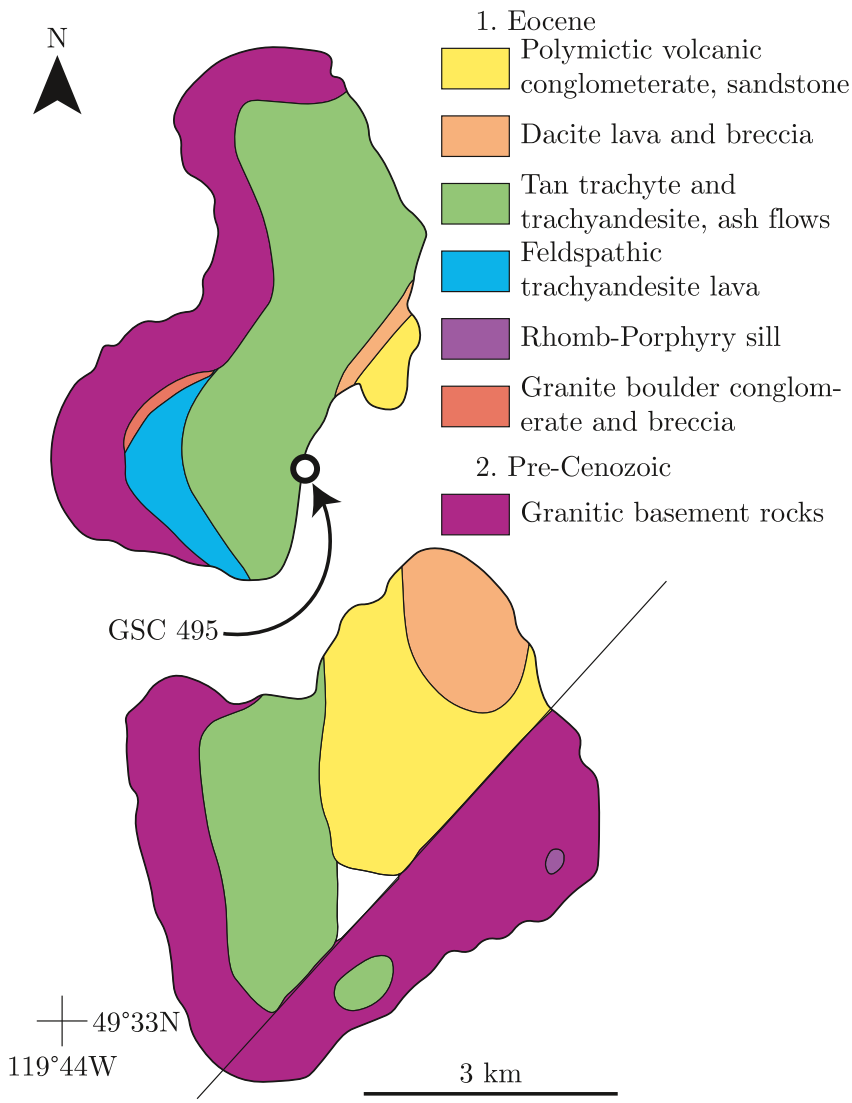

Figure A4. A geological map of the Summerland Basin well location with the location of GSC 495 marked; modified from Church et al. (1990).

21699356, 2025, 2, Downloaded from https://agupubs.onlinelibrary.wiley.com/doi/10.1029/2024JB030213 by Cochrane France, Wiley Online Library on [28/01/2025]. See the Terms and Conditions (https://onlinelibrary.wiley.com/terms-and-conditions) on Wiley Online Library for rules of use; OA articles are governed by the applicable Creative Commons License

A5. Newberry

The Newberry Volcano cores used in this study were taken from an exploratory well (GEO N-2, sometimes referred to as GNC-2) drilled by Geo Newberry Crater, Inc. to a depth of approximately 1,370 m and with a maximum temperature of 167°C (Ayling et al., 2012; Walkey & Swanberg, 1990). This well is located approximately 2.8 km from the western flank of the Newberry caldera and was one of a number of exploratory wells drilled in the area (Bargar & Keith, 1999). Core from the GEO N-2 well has been previously described by Bargar and Keith (1999) and used in fracture characterization (Ayling et al., 2012), geophysical (Fetterman & Davatzes, 2011), and geomechanical (Li et al., 2012; Wang et al., 2016) studies among others.

Approximately 30 years after the drilling of GEO N-2, in 2008 a further well NWG 55-29, located approximately 1 km from GEO N-2, Figure A5, was drilled and targeted for shear stimulation by AltaRock Energy (Cladouhos et al., 2016). This well was drilled to a measured depth of 3,067 m and recorded an equilibrated static bottom hole temperature of 331°C (Cladouhos et al., 2016). Shear stimulation occurred across of 1200-m stretch of uncased hole (Fang et al., 2016), and concerns about related induced seismicity, have led AltaRock Energy to commission a risk assessment report related to induced seismicity (Wong et al., 2010) and perform seismic monitoring (Cladouhos et al., 2013). The potential for induced seismicity due to this project has been the subject of laboratory studies using core from NWG 55-29 (Fang et al., 2016).

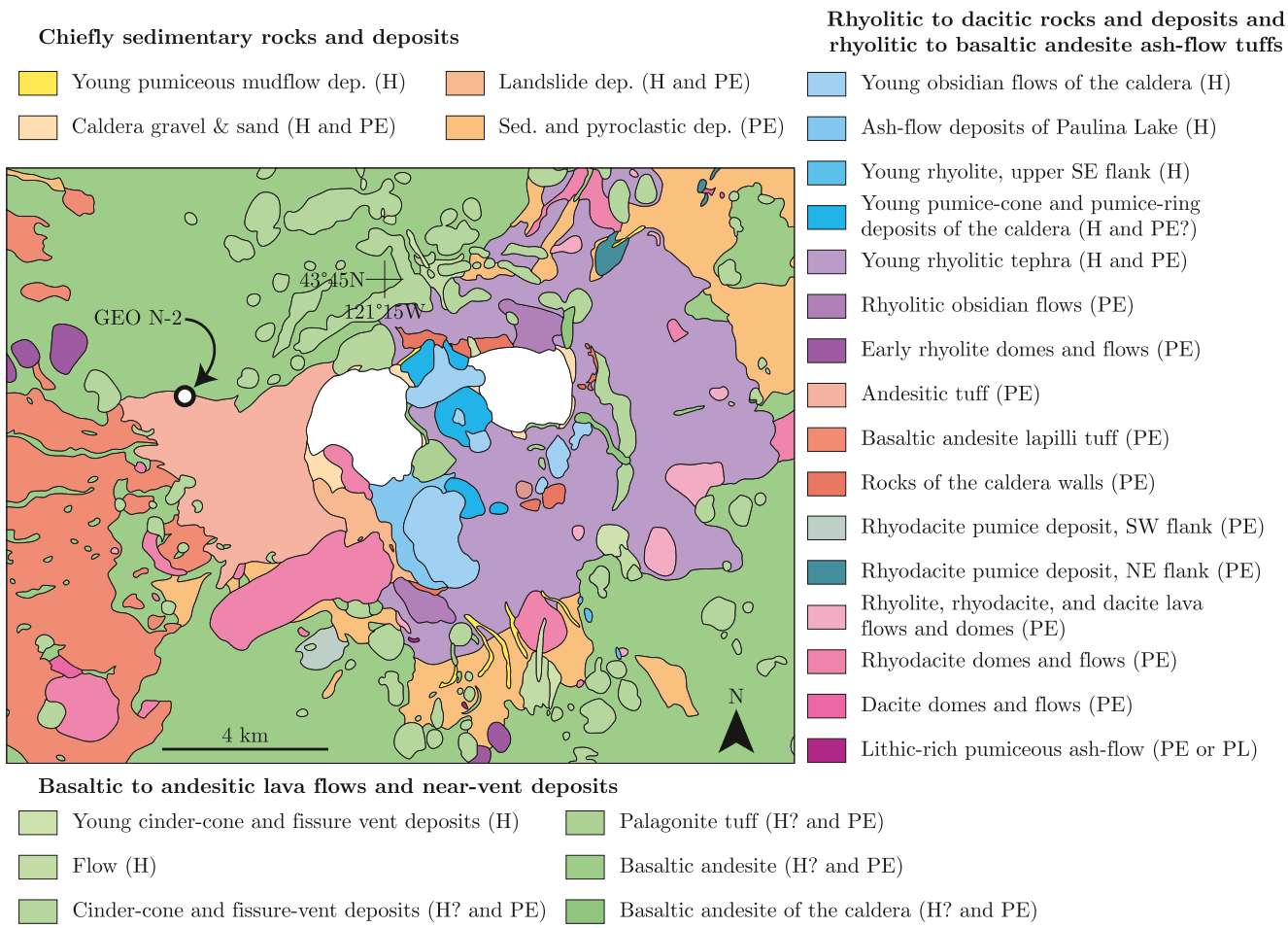

Figure A5. A geological map of Newberry Volcano with the location of the well GEO-N2 marked; modified from MacLeod et al. (1995). The age abbreviations are H for Holocene, PE for Pleistocene, and PL for Pliocene.

21699356, 2025, 2, Downloaded from https://agupubs.onlinelibrary.wiley.com/doi/10.1029/2024JB030213 by Cochrane France, Wiley Online Library on [28/01/2025]. See the Terms and Conditions (https://onlinelibrary.wiley.com/terms-and-conditions) on Wiley Online Library for rules of use; OA articles are governed by the applicable Creative Commons License

Conflict of Interest

The authors BF and GM are funded by AltaRock Energy who also provided five cores for this study from the GEO N-2 well, a well located near to and relevant for the Newberry EGS Demonstration Project run by AltaRock Energy. The frictional properties of their samples have implications for the potential of induced seismicity related to the Newberry EGS Demonstration Project, an issue of concern for AltaRock Energy. Similarly, SG is employed by the Geological Survey of Canada who are actively investigating the geothermal potential of the Mount Meager Volcanic Complex and provided five cores for this study.

Data Availability Statement

The raw data files, the MATLAB scripts used to treat them, and the resulting data summaries have been made available online for the samples from the Lesser Antilles Volcanic Arc (Fryer et al., 2024b) and the Cascade Volcanic Arc (Fryer et al., 2024a).

Acknowledgments
BF and GM acknowledge funding from AltaRock Energy. MV acknowledges support by the European Research Council Starting Grant project 757290-BEFINE. The authors would like to thank Laurent Morier, Michael Monnet, Michel Teuscher, Laurent Gastaldo, and Carolina Giorgetti for their help and guidance with the mechanical aspects of the HighSTEPS apparatus, and Felix Aeschimann and Lukas Koepfli for their help with the HighSTEPS software. Lionel Sofia is thanked for performing the granulometric analysis. Youness Zangui and Thin Section Lab are thanked for their careful preparation of the thin sections. Amaury Annoye and Yasser Tahiri are thanked for their help in the grinding of five of the samples. Grégiore Baroz and Daniel Beaufort are acknowledged for their help in using the SEM at EPFL and the Université de Poitiers, respectively. The Geological Survey of Canada, AltaRock Energy, Geoffrey Garrison, and Bernard Sanjuan are recognized for their willingness to provide samples. Quaise Energy and Carlos Araque are acknowledged. Randy Hughes is thanked for help providing data for the Mount Meager geological map and Corentin Noël is thanked for his helping prepare it. XRD analyses were performed on the instruments from the Mineralogy platform of the Institut des Sciences de la Terre (ISTerre—Grenoble, France), which is part of Labex OSUG@2020 (ANR10-LABX56). The two reviewers, Brett Carpenter and Telemaco Tesei, and an anonymous associate editor are thanked for their insightful comments and feedback.

References

Adachi, J., Detournay, E., & Peirce, A. (2010). Analysis of the classical pseudo-3D model for hydraulic fracture with equilibrium height growth across stress barriers. *International Journal of Rock Mechanics and Mining Sciences*, *47*(4), 625–639. https://doi.org/10.1016/j.ijrmms.2010.03.008

Ashman, I., & Faulkner, D. (2023). The effect of clay content on the dilatancy and frictional properties of fault gouge. *Journal of Geophysical Research: Solid Earth*, *128*(4), e2022JB025878. https://doi.org/10.1029/2022JB025878

Ayling, B., Rose, P., Petty, S., Zemach, E., & Drakos, P. (2012). QEMSCAN (quantitative evaluation of minerals by scanning electron microscopy): Capability and application to fracture characterization in geothermal systems. In *Proceedings: Thirty-Seventh workshop on geothermal reservoir engineering*. Stanford University.

Barcelona, H., Yagupsky, D., & Agusto, M. (2019). The layered model of the Copahue geothermal reservoir, Argentina. *Geothermal Energy*, *7*(1), 7. https://doi.org/10.1186/s40517-019-0124-9

Bargar, K., & Keith, T. (1999). Hydrothermal mineralogy of core geothermal drill holes at newberry volcano, oregon (No. 1578).

Beauchamps, G., Ledésert, B., Hébert, R., Navelot, V., & Favier, A. (2019). The characterisation of an exhumed high-temperature paleo-geothermal system on Terre-de-Haut Island (the Les Saintes archipelago, Guadeloupe) in terms of clay minerals and properties. *Geothermal Energy*, *7*(1), 6. https://doi.org/10.1186/s40517-019-0122-y

Berthé, D., Choukroune, P., & Jegouzo, P. (1979). Orthogneiss, mylonite and non coaxial deformation of granites: The example of the South Armorican shear zone. *Journal of Structural Geology*, *1*, 31–42. https://doi.org/10.1016/0191-8141(79)90019-1

Blanpied, M., Lockner, D., & Byerlee, J. (1991). Fault stability inferred from granite sliding experiments at hydrothermal conditions. *Geophysical Research Letters*, *18*(4), 609–612. https://doi.org/10.1029/91GL00469

Bos, B., & Spiers, C. (2000). Effect of phyllosilicates on fluid-assisted healing of gouge-bearing faults. *Earth and Planetary Science Letters*, *184*(1), 199–210. https://doi.org/10.1016/S0012-821X(00)00304-6

Bos, B., & Spiers, C. (2001). Experimental investigation into the microstructural and mechanical evolution of phyllosilicate-bearing fault rock under conditions favoring pressure solution. *Journal of Structural Geology*, *23*(8), 1187–1202. https://doi.org/10.1016/S0191-8141(00)00184-X

Bouchot, V., Sanjuan, B., Traineau, H., Guillou-Frottier, L., Thinon, I., Baltassat, J., et al. (2010). Assessment of the Bouillante Geothermal Field (Guadeloupe, French West Indies): Toward a conceptual model of the high temperature geothermal system. In *Proceedings world geothermal congress 2010*.

Boulton, C., Carpenter, B., Toy, V., & Marone, C. (2012). Physical properties of surface outcrop cataclastic fault rocks, Alpine Fault, New Zealand. *Geochemistry, Geophysics, Geosystems*, *13*(1), Q01018. https://doi.org/10.1029/2011GC003872

Brown, K., Kopf, A., Underwood, M., & Weinberger, J. (2003). Compositional and fluid pressure controls on the state of stress on the Nankai subduction thrust: A weak plate boundary. *Earth and Planetary Science Letters*, *214*(3–4), 589–603. https://doi.org/10.1016/S0012-821X(03)00388-1

Browne, P. (1978). Hydrothermal alteration in active geothermal fields. *Annual Review of Earth and Planetary Sciences*, *6*(1), 229–250. https://doi.org/10.1146/annurev.ea.06.050178.001305

Brudy, M., Zoback, M., Fuchs, K., Rummel, F., & Baumgärtner, J. (1997). Estimation of the complete stress tensor to 8 km depth in the KTB scientific drill holes: Implications for crustal strength. *Journal of Geophysical Research*, *102*(B8), 18453–18475. https://doi.org/10.1029/96JB02942

Byerlee, J. (1968). Brittle-ductile transition in rocks. *Journal of Geophysical Research*, *73*(14), 4741–4750. https://doi.org/10.1029/JB073i014p04741

Cameli, G., Dini, I., & Liotta, D. (1993). Upper crustal structure of the Larderello geothermal field as a feature of post-collisional extensional tectonics (Southern Tuscany, Italy). *Tectonophysics*, *224*(4), 413–423. https://doi.org/10.1016/0040-1951(93)90041-H

Carpenter, B., Collettini, C., Viti, C., & Cavallo, A. (2016a). The influence of normal stress and sliding velocity on the frictional behaviour of calcite at room temperature: Insights from laboratory experiments and microstructural observations. *Geophysical Journal International*, *205*(1), 548–561. https://doi.org/10.1093/gji/ggw038

Carpenter, B., Ikari, M., & Marone, C. (2016b). Laboratory observations of time-dependent frictional strengthening and stress relaxation in natural and synthetic fault gouges. *Journal of Geophysical Research: Solid Earth*, *121*(2), 1183–1201. https://doi.org/10.1002/2015JB012136

Carpenter, B., Marone, C., & Saffer, D. (2011). Weakness of the San Andreas Fault revealed by samples from the active fault zone. *Nature Geoscience*, *4*, 251–254. https://doi.org/10.1038/NGEO1089

Cathelineau, M., & Izquierdo, G. (1988). Temperature - Composition relationships of authigenic micaceous minerals in the Los Azufres geothermal system. *Contributions to Mineralogy and Petrology*, *100*(4), 418–428. https://doi.org/10.1007/BF00371372

21699356, 2025, 2, Downloaded from https://agupubs.onlinelibrary.wiley.com/doi/10.1029/2024JB030213 by Cochrane France, Wiley Online Library on [28/01/2025]. See the Terms and Conditions (https://onlinelibrary.wiley.com/terms-and-conditions) on Wiley Online Library for rules of use; OA articles are governed by the applicable Creative Commons License

Chen, J., Verberne, B., & Spiers, C. (2015). Effects of healing on the seismogenic potential of carbonate fault rocks: Experiments on samples from the Longmenshan Fault, Sichuan, China. *Journal of Geophysical Research: Solid Earth*, *120*(8), 5479–5506. https://doi.org/10.1002/2015JB012051

Church, B., Jessop, A., Bell, R., & Pettipas, A. (1990). *Tertiary outlier studies: Recent investigations in the Summerland Basin, South Okanagan area, B.C. (82E/12)* (pp. 163–170). Geological Fieldwork.

Cladouhos, T., Petty, S., Nordin, Y., Moore, M., Grasso, K., Uddenberg, M., & Swyer, M. (2013). Stimulation results from the Newberry VolcanoVolcano EGS demonstration. *Geothermal Resources Council - Transactions*, *37*, 133–140.

Cladouhos, T., Petty, S., Swyer, M., Uddenberg, M., Grasso, K., & Nordin, Y. (2016). Results from Newberry VolcanoVolcano EGS demonstration, 2010-2014. *Geothermics*, *63*, 44–61. https://doi.org/10.1016/j.geothermics.2015.08.009

Collettini, C., Tesei, T., Scuderi, M., Carpenter, B., & Viti, C. (2019). Beyond Byerlee friction, weak faults and implications for slip behavior. *Earth and Planetary Science Letters*, *519*, 245–263. https://doi.org/10.1016/j.epsl.2019.05.011

Correia, H., Sigurdsson, O., Sanjuan, B., Tulinius, H., & Lasne, E. (2000). Stimulation of a high-enthalpy geothermal well by cold water injection. *Geothermal Resources Council - Transactions*, *24*, 129–136.

Curewitz, D., & Karson, J. (1997). Structural settings of hydrothermal outflow: Fracture permeability maintained by fault propagation and interaction. *Journal of Volcanology and Geothermal Research*, *79*(3–4), 149–168. https://doi.org/10.1016/S0377-0273(97)00027-9

DeMets, C., Gordon, R., & Argus, D. (2010). Geologically current plate motions. *Geophysical Journal International*, *181*, 1–80. https://doi.org/10.1111/j.1365-246X.2009.04491x

Deng, J., & Sykes, L. (1995). Determination of Euler pole for contemporary relative motion of Caribbean and North American plates using slip vectors of interplate earthquakes. *Tectonics*, *14*(1), 39–53. https://doi.org/10.1029/94TC02547

Dieterich, J. (1972). Time-dependent friction in rocks. *Journal of Geophysical Research*, *77*, 3690–3697. https://doi.org/10.1007/BF00876539

Dieterich, J. (1979). Modeling of rock friction 1. Experimental results and constitutive equations. *Journal of Geophysical Research*, *84*(B5), 2161–2168. https://doi.org/10.1029/JB084iB05p02161

Doebelin, N., & Kleeberg, R. (2015). *Profex*: A graphical user interface for the Rietveld refinement program *BGMN*. *Journal of Applied Crystallography*, *48*(5), 1573–1580. https://doi.org/10.1107/S1600576715014685

Dorbath, L., Cuenot, N., Genter, A., & Frogneux, M. (2009). Seismic response of the fractured and faulted granite of Soultz-sous-Forêts (France) to 5 km deep massive water injections. *Geophysical Journal International*, *177*(2), 653–675. https://doi.org/10.1111/j.1365-246X.2009.04030x

Evans, K., Zappone, A., Kraft, T., Deichmann, N., & Moia, F. (2012). A survey of the induced seismic responses to fluid injection in geothermal and CO2 reservoirs in Europe. *Geothermics*, *41*, 30–54. https://doi.org/10.1016/j.geothermics.2011.08.002

Fang, Y., den Hartog, S., Elsworth, D., Marone, C., & Cladouhos, T. (2016). Anomalous distribution of microearthquakes in the newberry geothermal reservoir: Mechanisms and implications. *Geothermics*, *63*, 62–73. https://doi.org/10.1016/j.geothermics.2015.04.005

Favier, A., Lardeaux, J., Corsini, M., Verati, C., Navelot, V., Géraud, Y., et al. (2021a). Characterization of an exhumed high-temperature hydrothermal system and its application for deep geothermal exploration: An example from Terre-de-Haut Island (Guadeloupe archipelago, Lesser Antilles volcanic arc). *Journal of Volcanology and Geothermal Research*, *418*, 107256. https://doi.org/10.1016/j.jvolgeores.2021.107256

Favier, A., Lardeaux, J., Legendre, L., Verati, C., Philippon, M., Corsini, M., et al. (2019). Tectono-metamorphic evolution of shallow crustal levels within active volcanic arcs. Insights from the exhumed Basal Complex of Basse-Terre (Guadeloupe, French West Indies). *Earth Science Bulletin*, *190*, 10. https://doi.org/10.1051/bsgf/2019011

Favier, A., Lardeaux, J., Verati, C., Corsini, M., Münch, P., & Ventalon, S. (2021b). The concept of exhumed analogue for characterization of high-energy geothermal reservoir: An example from Les Saintes Island (Guadeloupe Archipelago, Lesser Antilles) and consequences for exploration. In *Proceedings world geothermal congress 2020+1*.

Fenner, C. (1934). Hydrothermal metamorphism in geyser-basins of Yellowstone Park, as shown by deep drilling. *Eos, Transactions American Geophysical Union*, *15*, 240–243. https://doi.org/10.1029/TR015i001p00240-2

Fetterman, J., & Davatzes, N. (2011). Evolution of porosity in fractures in the Newberry Volcano geothermal system, Oregon, USA: Feedback between deformation and alteration. *Geothermal Resources Council - Transactions*, *35*, 339–346.

Frolova, J., Ladygin, V., & Rychagov, S. (2006). Petrophysical indicators of argillization zone in geothermal fields. *Geothermal Resources Council - Transactions*, *30*, 909–912.

Frolova, J., Ladygin, V., & Rychagov, S. (2010). Petrophysical alteration of volcanic rocks in hydrothermal systems of the Kuril-Kamchatka Island Arc. In *Proceedings world geothermal congress 2010*.

Frolova, J., Ladygin, V., Rychagov, S., & Zukhubaya, D. (2014). Effects of hydrothermal alterations on physical and mechanical properties of rocks in the Kuril-Kamchatka island arc. *Engineering Geology*, *183*, 80–95. https://doi.org/10.1016/j.enggeo.2014.10.011

Fryer, B., Jermann, F., Patrier, P., Lanson, B., Jelavic, S., Meyer, G., et al. (2024a). Data Set for "Alteration's control on frictional behavior and the depth of the ductile shear zone in geothermal reservoirs in volcanic arcs" I: Cascade Volcanic Arc [Dataset]. *Zenodo*. https://doi.org/10.5281/zenodo.10964935

Fryer, B., Jermann, F., Patrier, P., Lanson, B., Jelavic, S., Meyer, G., & Violay, M. (2024b). Data Set for "Alteration's control on frictional behavior and the depth of the ductile shear zone in geothermal reservoirs in volcanic arcs" I: Lesser Antilles Volcanic Arc [Dataset]. *Zenodo*. https://doi.org/10.5281/zenodo.10912444

Gadalia, A., Baltassat, J., Bouchot, V., Caritg, S., Coppo, N., Gal, F., et al. (2014). *Compléments d'exploration géothermique en Martinique: Conclusions et recommandations pour les zones de la Montagne Pelée*. des Anses-d'Arlet, des Pitons du Carbet et du Lamentin.

Gadalia, A., Bouchot, V., Calcagno, P., Caritg, S., Courrioux, G., Darnet, M., et al. (2019). Multimodal geothermal exploration in the lesser Antilles arc at the Lamentin lowland (Martinique). *Iop conf. series: Earth and environmental science*, *249*, 012001. https://doi.org/10.1088/1755-1315/249/1/012001

Genter, A., Traineau, H., Degouy, M., Correia, H., Mas, A., Patrier, P., et al. (2002). Preliminary geological results of recent exploratory drillings in a geotheral fractured reservoir at Lamentin (French West Indies, Martinique). In *Proceedings: Twenty-Seventh workshop on geothermal reservoir engineering Stanford University, Stanford, California, January 28-30, 2002*.

Ghomshei, M., Sanyal, S., MacLeod, K., Henneberger, R., Ryder, A., Meech, J., & Fainbank, B. (2004). *Status of the South Meager geothermal project British Columbia, Canada: Resource evaluation and plans for development* (Vol. 28, pp. 339–344). Geothermal Resources Council Transactions.

Giacomel, P., Ruggieri, R., Scuderi, M., Spagnuolo, E., Di Toro, G., & Collettini, C. (2021). Frictional properties of basalt experimental faults and implications for volcano-tectonic settings and geo-energy sites. *Tectonophysics*, *881*, 228883. https://doi.org/10.1016/j.tecto.2021.228883

Giorgetti, C., Carpenter, B., & Collettini, C. (2015). Frictional behavior of talc-calcite mixtures. *Journal of Geophysical Research: Solid Earth*, *120*(9), 6614–6633. https://doi.org/10.1002/2015JB011970

21699356, 2025, 2, Downloaded from https://agupubs.onlinelibrary.wiley.com/doi/10.1029/2024JB030213 by Cochrane France, Wiley Online Library on [28/01/2025]. See the Terms and Conditions (https://onlinelibrary.wiley.com/terms-and-conditions) on Wiley Online Library for rules of use; OA articles are governed by the applicable Creative Commons License

Global Volcanism Program. (2024). *Volcanoes of the world*. Smithsonian Institution, compiled by Venzke. https://doi.org/10.5479/si.GVP.VOTW5-2024.5.2

Goko, K. (2000). Structure and hydrology of the Ogiri field, West Kirishima geothermal area, Kyushu, Japan. *Geothermics*, *29*(2), 127–149. https://doi.org/10.1016/S0375-6505(99)00055-3

Grasby, S., Ansari, S., Bryant, R., Calahorrano-DiPatre, A., Chen, Z., Craven, J., et al. (2020). Garibaldi geothermal energy project - Mount Meager 2019 field program (No. 2020-09).

Grasby, S., Calahorrano-Di Patre, A., Chen, Z., Dettmer, J., Gilbert, H., Hanneson, C., et al. (2022). Geothermal resource potential of the Garibaldi volcanic Belt, southwestern British Columbia (part of NTS 092J): Phase 2. In *Geoscience BC summary of activities 2021: Energy and water, geoscience BC, report 2022-02* (pp. 75–80). Geoscience BC.

Griggs, D. (1936). Deformation of rocks under high confining pressures: I. Experiments at room temperature. *The Journal of Geology*, *44*(5), 541–577. https://doi.org/10.1086/624455

Häring, M., Schanz, U., Ladner, F., & Dyer, B. (2008). Characterisation of the Basel 1 enhanced geothermal system. *Geothermics*, *37*(5), 469–495. https://doi.org/10.1016/j.geothermics.2008.06.002

Harrison, E., Kieschnick, W., & McGuire, W. (1954). The mechanics of fracture induction and extension. *Petroleum Transactions*, *201*(01), 252–263. https://doi.org/10.2118/318-g

Heap, M., Troll, V., Kushnir, A., Gilg, A., Collinson, A., Deegan, F., et al. (2019). Hydrothermal alteration of andesitic lava domes can lead to explosive volcanic behaviour. *Nature Communications*, *10*(1), 5063. https://doi.org/10.1038/s41467-019-13102-8

Hormozzade Ghalati, F., Craven, J., Motazedian, D., Grasby, S., Roots, E., Tschirhart, V., et al. (2023). Analysis of fluid flow pathways in the Mount Meager Volcanic Complex, Southwestern Canada, utilizing AMT and petrophysical data. *Geochemistry, Geophysics, Geosystems*, *24*(3), e2022GC010814. https://doi.org/10.1029/2022GC010814

Ikari, M., Carpenter, B., & Marone, C. (2016). A microphysical interpretation of rate- and state-dependent friction for fault gouge. *Geochemistry, Geophysics, Geosystems*, *17*(5), 1660–1677. https://doi.org/10.1002/2016GC006286

Ikari, M., Marone, C., & Saffer, D. (2011). On the relation between fault strength and frictional stability. *Geology*, *39*(1), 83–86. https://doi.org/10.1130/G31416.1

Ikari, M., Saffer, D., & Marone, C. (2007). Effect of hydration state on the frictional properties of montmorillonite-based fault gouge. *Journal of Geophysical Research*, *112*(B6), B06423. https://doi.org/10.1029/2006JB004748

Ikari, M., Saffer, D., & Marone, C. (2009). Frictional and hydrologic properties of clay-rich fault gouge. *Journal of Geophysical Research*, *114*(B5), B05409. https://doi.org/10.1029/2008JB006089

Imber, J., Holdsworth, R., Butler, C., & Strachan, R. (2001). A reappraisal of the Sibson-Scholz fault zone model: The nature of the frictional to viscous ("brittle-ductile") transition along a long-lived crustal-scale fault, Outer Hebrides, Scotland. *Tectonics*, *20*(5), 601–624. https://doi.org/10.1029/2000TC001250

IRD. (2014). Les ressources en eau de surface de la Martinique. A set of 9 map sheets. In *Scale of 1:100000. Date of publication: 1974-1975. Project NumeriSud SPHAERA-GEO*.

Jacques, D., & Maury, R. (1988). L'archipel des Saintes (Guadeloupe, Petites Antilles): Géologie et pétrologie. *Géologie de la France*, *2*, 89–99.

Jaud, P., & Lamethe, D. (1985). Les installations géothermiques de Bouillante. *La Houille Blanche*, *71*(3–4), 347–352. https://doi.org/10.1051/lhb/1985025

Jeppson, T., Lockner, D., Beeler, N., & Moore, D. (2023). Time-dependent weakening of granite at hydrothermal conditions. *Geophysical Research Letters*, *50*(21), e2023GL105517. https://doi.org/10.1029/2023GL105517

Jessop, A. (2008). Review of the national geothermal energy program phase 2 - geothermal potential of the Cordillera (No. 5906).

Jolie, E., Scott, S., Faulds, J., Chambefort, I., Axelsson, G., Gutiérrez-Negrín, L., et al. (2021). Geological controls on geothermal resources for power generation. *Nature Reviews Earth & Environment*, *2*(5), 324–339. https://doi.org/10.1038/s43017-021-00154-y

Keefer, D. (1984). Rock avalanches caused by earthquakes: Source characteristics. *Science*, *223*(4642), 1288–1290. https://doi.org/10.1126/science.223.4642.1288

Kim, K., Ree, J., Kim, Y., Kim, S., Kang, S., & Seo, W. (2018). Assessing whether the 2017 M_W 5.4 Pohang earthquake in South Korea was an induced event. *Science*, *360*(6392), 1007–1009. https://doi.org/10.1126/science.aat6081

Knipe, R., & McCaig, A. (1994). Microstructural and microchemical consequences of fluid flow in deforming rocks. In J. Parnell (Ed.), *Geofluids: Origin, migration and evolution of fluids in sedimentary basins* (pp. 99–111). Geological Society.

Kohlstedt, D., Evans, B., & Mackwell, S. (1995). Strength of the lithosphere: Constraints imposed by laboratory experiments. *Journal of Geophysical Research*, *100*(B9), 17587–17602. https://doi.org/10.1029/95JB01460

Kolawole, F., Johnston, C., Morgan, C., Chang, J., Marfurt, K., Lockner, D., et al. (2019). The susceptibility of Oklahoma's basement to seismic reactivation. *Nature Geoscience*, *12*(10), 839–844. https://doi.org/10.1038/s41561-019-0440-5

Koroknai, B., Árkai, P., Horváth, P., & Balogh, K. (2008). Anatomy of a transitional brittle-ductile shear zone developed in a low-T meta-andesite tuff: A microstructural, petrological and geochronological case study from the Bükk Mts. (NE Hungary). *Journal of Structural Geology*, *30*(2), 159–176. https://doi.org/10.1016/j.jsg.2007.10.007

Kry, P., & Gronseth, J. (1983). In-situ stresses and hydraulic fracturing in the Deep Basin. *Journal of Canadian Petroleum Technology*, *22*(06). https://doi.org/10.2118/83-06-02

Kutz, M. (2009). *Eshbach's handbook of engineering fundamentals*. John Wiley & Sons, Inc.

Li, Y., Wang, J., Jung, W., & Ghassemi, A. (2012). Mechanical properties of intact rock and fractures in welded tuff from Newberry Volcano. In *Proceedings, thirty-seventh workshop on geothermal reservoir engineering*. Stanford Universiy.

Logan, J., Dengo, C., Higgs, N., & Wang, Z. (1992). Fabrics of experimental fault zones: Their development and relationship to mechanical behavior. *International Geophysics*, *51*, 33–67. https://doi.org/10.1016/S0074-6142(08)62814-4

Logan, J., & Rauenzahn, K. (1987). Frictional dependence of gouge mixtures of quartz and montmorillonite on velocity, composition and fabric. *Tectonophysics*, *144*(1–3), 87–108. https://doi.org/10.1016/0040-1951(87)90010-2

Lucchitta, I. (1990). Role of heat and detachment in continental extension as viewed from the eastern Basin and Range Province in Arizona. *Tectonophysics*, *174*(1–2), 77–114. https://doi.org/10.1016/0040-1951(90)90385-L

Lucier, A., Zoback, M., Gupta, N., & Ramakrishnan, T. (2006). Geomechanical aspects of CO2 sequestration in a deep saline reservoir in the Ohio River Valley region. *Environmental Geosciences*, *13*(2), 85–103. https://doi.org/10.1306/eg.11230505010

Lupini, J., Skinner, A., & Vaughan, P. (1981). The drained residual strength of cohesive soils. *Géotechnique*, *31*(2), 181–213. https://doi.org/10.1680/geot.1981.31.2.181

MacLeod, N., & Sammel, E. (1982). Newberry Volcano, Oregon: A cascade range geothermal prospect. *Oregon Geology*, *44*, 123–131.

MacLeod, N., & Sherrod, D. (1988). Geologic evidence for a magma chamber beneath Newberry Volcano, Oregon. *Journal of Geophysical Research*, *93*(B9), 10067–10079. https://doi.org/10.1029/JB093iB09p10067

21699356, 2025, 2, Downloaded from https://agupubs.onlinelibrary.wiley.com/doi/10.1029/2024JB030213 by Cochrane France, Wiley Online Library on [28/01/2025]. See the Terms and Conditions (https://onlinelibrary.wiley.com/terms-and-conditions) on Wiley Online Library for rules of use; OA articles are governed by the applicable Creative Commons License

MacLeod, N., Sherrod, D., Chitwood, L., & Jensen, R. (1995). Geologic map of Newberry Volcano, Deschutes, Klamath, and lake Counties, Oregon.

Manga, M., Hornbach, M., Le Friant, A., Ishizuka, O., Stroncik, N., Adachi, T., et al. (2012). Heat flow in the lesser Antilles island arc and adjacent back arc Grenada basin. *Geochemistry, Geophysics, Geosystems*, *13*(8), Q08007. https://doi.org/10.1029/2012GC004260

Marone, C. (1998). Laboratory-derived friction laws and their application to seismic faulting. *Annual Review of Earth and Planetary Sciences*, *26*(1), 643–696. https://doi.org/10.1146/annurev.earth.26.1.643

Marone, C., & Kilgore, B. (1993). Scaling of the critical slip distance for seismic faulting with shear strain in fault zones. *Nature*, *362*(6421), 618–621. https://doi.org/10.1038/362618a0

Marone, C., Raleigh, C., & Scholz, C. (1990). Frictional behavior and constitutive modeling of simulated fault gouge. *Journal of Geophysical Research*, *95*(B5), 7007–7025. https://doi.org/10.1029/JB095iB05p07007

Mas, A., Guisseau, D., Patrier, P., Beaufort, D., Genter, A., Sanjuan, B., & Girard, J. (2006). Clay minerals related to the hydrothermal activity of the Bouillante geothermal field (Guadeloupe). *Journal of Volcanology and Geothermal Research*, *158*(3–4), 380–400. https://doi.org/10.1016/j.jvolgeores.2006.07.010

Mas, A., Patrier, P., Beaufort, D., & Genter, A. (2003). Clay-mineral signatures of fossil and active hydrothermal circulations in the geothermal system of Lamentin Plain, Martinique. *Journal of Volcanology and Geothermal Research*, *124*(3–4), 195–218. https://doi.org/10.1016/S0377-0273(03)00044-1

Maza, S., Collo, G., Morata, D., Lizana, C., Camus, E., Taussi, M., et al. (2018). Clay mineral associations in the clay cap from the Cerro Pabellón blind geothermal system, Andean Cordillera, Northern Chile. *Clay Minerals*, *53*(2), 117–141. https://doi.org/10.1180/clm.2018.9

Meller, C., & Kohl, T. (2014). The significance of hydrothermal alteration zones for the mechanical behavior of a geothermal reservoir. *Geothermal Energy*, *2*(1), 12. https://doi.org/10.1186/s40517-014-0012-2

Melosh, G., Cumming, W., Benoit, D., Wilmarth, M., Colvin, A., Winick, J., et al. (2010). Exploration results and resource conceptual model of the Tolhuaca Geothermal Field, Chile. In *Proceedings world geothermal congress 2010*.

Meng, M., Frash, L., Li, W., Welch, N., Carey, J., Morris, J., et al. (2022). Hydro-mechanical measurements of sheared crystalline rock fractures with applications for EGS Collab Experiments 1 and 2. *Journal of Geophysical Research: Solid Earth*, *127*. https://doi.org/10.1029/2021JB023000

Meyer, G., Brantut, N., Mitchell, T., & Meredith, P. (2019). Fault reactivation and strain partitioning across the brittle-ductile transition. *Geology*, *47*(12), 1127–1130. https://doi.org/10.1130/G46516.1

Meyer, G., & Violay, V. (2023). Bounding the localized to ductile transition in porous rocks: Implications for geo-reservoirs. *Geophyscial Journal International*, *235*(3), 2361–2371. https://doi.org/10.1093/gji/ggad377

Michel, F., Allen, D., & Grant, M. (2002). Hydrogeochemistry and geothermal characteristics of the white lake basin, South-central British Columbia, Canada. *Geothermics*, *31*(2), 169–194. https://doi.org/10.1016/S0375-6505(01)00009-8

Monger, J., & Irving, E. (1980). Northward displacement of north-central British Columbia. *Nature*, *285*(5763), 289–294. https://doi.org/10.1038/285289a0

Montgomery, D., & Runger, G. (2011). *Applied statistics and probability for engineers* (5th ed.). John Wiley & Sons, Inc.

Moore, D., & Lockner, D. (2004). Crystallographic controls on the frictional behavior of dry and water-saturated sheet structure minerals. *Journal of Geophysical Research*, *109*(B3), B03401. https://doi.org/10.1029/2003JB002582

Moore, D., & Lockner, D. (2007). Friction of the smectite clay montmorillonite. In T. Dixon & C. Moore (Eds.), *The seismogenic zone of subduction thrust faults* (pp. 317–345). Columbia University Press.

Moore, D., Lockner, D., Shengli, M., Summers, R., & Byerlee, J. (1997). Strengths of serpentinite gouges at elevated temperatures. *Journal of Geophysical Research*, *102*, 14787–14801. https://doi.org/10.1029/97JB00995

Morrow, C., Moore, D., & Lockner, D. (2000). The effect of mineral bond strength and absorbed water on fault gouge frictional strength. *Geophysical Research Letters*, *27*(6), 815–818. https://doi.org/10.1029/1999GL008401

Morrow, C., Radney, B., & Byerlee, J. (1992). Frictional strength and the effective pressure law of Montmorillonite and Illite clays. *International Geophysics*, *51*, 69–88. https://doi.org/10.1016/S0074-6142(08)62815-6

Navelot, V., Géraud, Y., Favier, A., Diraison, M., Corsini, M., Lardeaux, J., et al. (2018). Petrophysical properties of volcanic rocks and impacts of hydrothermal alteration in the Guadeloupe Archipelago (West Indies). *Journal of Volcanology and Geothermal Research*, *360*, 1–21. https://doi.org/10.1016/j.jvolgeores.2018.07.004

Niemeijer, A., & Spiers, C. (2006). Velocity dependence of strength and healing behaviour in simulated phyllosilicate-bearing fault gouge. *Tectonophysics*, *427*(1–4), 231–253. https://doi.org/10.1016/j.tecto.2006.03.048

NOAA National Centers for Environmental Information. (2022). ETOPO 2022 15 arc-second global Relief model. https://doi.org/10.25921/fd45-gt74

Noël, C., Baud, P., & Violay, M. (2021). Effect of water on sandstone's fracture toughness and frictional parameters: Brittle strength constraints. *International Journal of Rock Mechanics and Mining Sciences*, *147*, 104916. https://doi.org/10.1016/j.ijrmms.2021.104916

Noël, C., Fryer, B., Baud, P., & Violay, V. (2024a). Water weakening and the compressive brittle strength of carbonates: Influence of fracture toughness and static friction. *Intenrational Journal of Rock Mechanics and Mining Sciences*, *177*, 105736. https://doi.org/10.1016/j.ijrmms.2024.105736

Noël, C., Giorgetti, C., Collettini, C., & Marone, C. (2024b). The effect of shear strain and shear localization on fault healing. *Geophysical Journal International*, *236*(3), 1206–1215. https://doi.org/10.1093/gji/ggad486

Noël, C., Giorgetti, C., Scuderi, M., Collettini, C., & Marone, C. (2023). The effect of shear displacement and wear on fault stability: Laboratory constraints. *Journal of Geophysical Research: Solid Earth*, *128*(4), e2022JB026191. https://doi.org/10.1029/2022JB026191

Obermann, A., Kraft, T., Larose, E., & Weimer, S. (2015). Potential of ambient seismic noise techniques to monitor the St. Gallen geothermal site (Switzerland). *Journal of Geophysical Research: Solid Earth*, *120*(6), 4301–4316. https://doi.org/10.1002/2014JB011817

Orellana, L., Scuderi, M., Collettini, C., & Violay, M. (2018). Frictional properties of Opalinus Clay: Implications for nuclear waste storage. *Journal of Geophysical Research: Solid Earth*, *123*(1), 157–175. https://doi.org/10.1002/2017JB014931

Paterson, M. (1958). Experimental deformation and faulting in Wombeyan marble. *Geological Society of America Bulletin*, *69*(4), 465–476. https://doi.org/10.1130/0016-7606(1958)69[465:EDAFIW]2.0.CO;2

Paterson, M., & Wong, T. (2005). *Experimental rock deformation - the brittle field*. Springer-Verlag.

Patrier, P., Beaufort, D., Bril, H., Bonhomme, M., Fouillac, A., & Aumâitre, R. (1997). Alteration-mineralization at the Bernardan U Deposit (Western Marche, France): The contribution of alteraion petrology and crystal chemistry of secondary phases to a new genetic model. *Economic Geology*, *92*(4), 448–467. https://doi.org/10.2113/gsecongeo.92.4.448

Phillips, N., Belzer, B., French, M., Rowe, C., & Ujiie, K. (2020). Frictional strengths of subduction thrust rocks in the region of shallow slow earthquakes. *Journal of Geophysical Research: Solid Earth*, *125*(3), e2019JB018888. https://doi.org/10.1029/2019JB018888

21699356, 2025, 2, Downloaded from https://agupubs.onlinelibrary.wiley.com/doi/10.1029/2024JB030213 by Cochrane France, Wiley Online Library on [28/01/2025]. See the Terms and Conditions (https://onlinelibrary.wiley.com/terms-and-conditions) on Wiley Online Library for rules of use; OA articles are governed by the applicable Creative Commons License

Pozzi, G., Collettini, C., Scuderi, M., Tesei, T., Marone, C., Amodio, A., & Cocco, M. (2023). Fabric controls fault stability in serpentinite gouges. *Geophysical Journal International*, *235*(2), 1778–1797. https://doi.org/10.1093/gji/ggad322

Pozzi, G., Scuderi, M., Tinti, E., Nazzari, M., & Collettini, C. (2022). The role of fault rock fabric in the dynamics of laboratory faults. *Journal of Geophysical Research: Solid Earth*, *127*(6), e2021JB023779. https://doi.org/10.1029/2021JB023779

Pramono, B., & Colombo, D. (2005). Microearthquake characteristics in Darajat geothermal field, Indonesia. In *Proceedings world geothermal congress 2005*.

Ranalli, G., & Rybach, L. (2005). Heat flow, heat transfer and lithosphere rheology in geothermal area: Features and examples. *Journal of Volcanology and Geothermal Research*, *148*(1–2), 3–19. https://doi.org/10.1016/j.jvolgeores.2005.04.010

Read, P. (1979). Geology, meager Creek geothermal area, British Columbia. *Geological Survey of Canada, Open File*, *603*(1). https://doi.org/10.4095/129507

Rejeki, S., Rohrs, D., Nordquist, G., & Fitriyanto, A. (2010). Geologic conceptual model update of the Darajat geothermal field, Indonesia. In *Proceedings world geothermal congress 2010*. Bali.

Revil, A., & Gresse, M. (2021). Induced polarizatin as a tool to assess alteration in geothermal systems: A review. *Minerals*, *11*(9), 962. https://doi.org/10.3390/min11090962

Rice, J., & Ruina, A. (1983). Stability of steady frictional slipping. *Journal of Applied Mechanics*, *50*(2), 343–349. https://doi.org/10.1115/1.3167042

Richards, J. (2011). Magmatic to hydrothermal metal fluxes in convergent and collided margins. *Ore Geology Reviews*, *40*, 1–26. https://doi.org/10.1016/j.oregeorev.2011.05.006

Ruina, A. (1983). Slip instability and state variable friction laws. *Journal of Geophysical Research*, *88*(B12), 10359–10370. https://doi.org/10.1029/JB088iB12p10359

Rutter, E. (1986). On the nomenclature of mode of failure transitions in rocks. *Tectonophysics*, *122*(3–4), 381–387. https://doi.org/10.1016/0040-1951(86)90153-8

Saffer, D., Lockner, D., & McKiernan, A. (2012). Effects of smectite to illite transformation on the frictional strength and sliding stability of intact marine mudstones. *Geophysical Research Letters*, *39*(11), L11304. https://doi.org/10.1029/2012GL051761

Saffer, D., & Marone, C. (2003). Comparison of smectite- and illite-rich gouge frictional properties: Application to the updip limit of the seismogenic zone along subduction megathrusts. *Earth and Planetary Science Letters*, *215*(1–2), 219–235. https://doi.org/10.1016/S0012-821X(03)00424-2

Sanchez-Alfaro, P., Reich, M., Arancibia, G., Pérez-Flores, P., Cembrano, J., Driesner, T., et al. (2016). Physical, chemical and mineralogical evolution of the Tolhuaca geothermal system, southern Andes, Chile: Insights into the interplay between hydrothermal alteration and brittle deformation. *Journal of Volcanology and Geothermal Research*, *324*, 88–104. https://doi.org/10.1016/j.jvolgeores.2016.05.009

Sanjuan, B., Genter, A., Correia, H., Girard, J., Roig, J., & Brach, M. (2002a). Travaux scientifiques associés à la réalisation des trois puits d'exploration géothermique dans la plaine du Lamentin (Martinique) (No. BRGM/RP-51671-FR).

Sanjuan, B., Traineau, H., Genter, A., Correia, H., Brach, M., & Degouy, M. (2002b). Geochemical investigations during a new geothermal exploration phase in the Lamentin Plain (French West Indies, Martinique). In *Proceedings: Twenty-Seventh workshop on geothermal reservoir engineering stanford University, Stanford, California, January 28-30, 2002*.

Scholz, C. (2019). *The mechanics of earthquakes and faulting*. Cambridge University Press. https://doi.org/10.1017/9781316681473

Scott, D., Marone, C., & Sammis, C. (1994). The apparent friction of granular fault gouge in sheared layers. *Journal of Geophysical Research*, *99*(B4), 7231–7246. https://doi.org/10.1029/93JB03361

Segall, P., & Rice, J. (1995). Dilatancy, compaction, and slip instability of a fluid-infiltrated fault. *Journal of Geophysical Research*, *100*(B11), 22155–22171. https://doi.org/10.1029/95JB02403

Shea, W., & Kronenberg, A. (1992). Rheology and deformation mechanisms of an isotropic mica schist. *Journal of Geophysical Research*, *97*(B11), 15201–15237. https://doi.org/10.1029/92JB00620

Shreedhara, S., Ikari, M., Wood, C., Saffer, D., Wallace, L., & Marone, C. (2022). Frictional and lithological controls on shallow slip at the Northern Hikurangi Margin. *Geochemistry, Geophysics, Geosystems*, *23*, e2021GC010107. https://doi.org/10.1029/2021GC010107

Siebert, L. (1984). Large volcanic debris avalanches: Characteristics of source areas, deposits, and associated eruptions. *Journal of Volcanology and Geothermal Research*, *22*(3–4), 163–197. https://doi.org/10.1016/0377-0273(84)90002-7

Sillitoe, R. (2010). Porphyry copper systems. *Economic Geology*, *105*(1), 3–41. https://doi.org/10.2113/gsecongeo.105.1.3

Skarbek, R., & Savage, H. (2019). RSFit3000: A MATLAB GUI-based program for determining rate and state frictional parameters from experimental data. *Geosphere*, *15*(5), 1665–1676. https://doi.org/10.1130/GES02122.1

Skempton, A. (1964). Long-term stability of clay slopes. *Géotechnique*, *14*(2), 77–102. https://doi.org/10.1680/geot.1964.14.2.77

Stelling, P., Shevenell, L., Hinz, N., Coolbaugh, M., Melosh, G., & Cumming, W. (2016). Geothermal systems in volcanic arcs: Volcanic characteristics and surface manifestations as indicators of geothermal potential and favorability worldwide. *Journal of Volcanology and Geothermal Research*, *324*, 57–72. https://doi.org/10.1016/j.jvolgeores.2016.05.018

Stimac, J., Goff, F., & Goff, C. (2015). Intrusion-related geothermal systems. In H. Sigurdsson (Ed.), *The encyclopedia of volcanoes* (pp. 799–822). Academic Press.

Stimac, J., Nordquist, G., Suminar, A., & Sirad-Azwar, L. (2008). An overview of the Awibengkok geothermal system, Indonesia. *Geothermics*, *37*(3), 300–331. https://doi.org/10.1016/j.geothermics.2008.04.004

Summers, R., & Byerlee, J. (1977). A note on the effect of fault gouge composition on the stability of frictional sliding. *International Journal of Rock Mechanics and Mining Sciences & Geomechanics Abstracts*, *14*(3), 155–160. https://doi.org/10.1016/0148-9062(77)90007-9

Tembe, S., Lockner, D., & Wong, T. (2010). Effect of clay content and mineralogy on frictional sliding behavior of simulated gouges: Binary and ternary mixtures of quartz, illite, and montmorillonite. *Journal of Geophysical Research*, *115*(B3), B03416. https://doi.org/10.1029/2009JB006383

Tesei, T., Carpenter, B., Giorgetti, C., Scuderi, M., Sagy, A., Scarlato, P., & Collettini, C. (2017). Friction and scale-dependent deformation processes of large experimental carbonate faults. *Journal of Structural Geology*, *100*, 12–23. https://doi.org/10.1016/j.jsg.2017.05.008

Tesei, T., Collettini, C., Carpenter, B., Viti, C., & Marone, C. (2012). Frictional strength and healing behavior of phyllosilicate-rich faults. *Journal of Geophysical Research*, *117*(B9), B09402. https://doi.org/10.1029/2012JB009204

Teufel, L. (1989). Influence of lithology and geologic structure on in situ stress: Examples of stress heterogeneity in reservoirs (No. DE89 014692).

Townend, J., & Zoback, M. (2000). How faulting keeps the crust strong. *Geology*, *28*(5), 399–402. https://doi.org/10.1130/0091-7613(2000)28<399:HFKTCS>2.0.CO;2

Verati, C., Lardeaux, J., Favier, A., Corsini, M., Philippon, M., & Legendre, L. (2018). Arc-related metamorphism in the Guadeloupe archipelago (Lesser Antilles active island arc): First report and consequences. *Lithos*, *320*, 592–598. https://doi.org/10.1016/j.lithos.2018.08.005

21699356, 2025, 2, Downloaded from https://agupubs.onlinelibrary.wiley.com/doi/10.1029/2024JB030213 by Cochrane France, Wiley Online Library on [28/01/2025]. See the Terms and Conditions (https://onlinelibrary.wiley.com/terms-and-conditions) on Wiley Online Library for rules of use; OA articles are governed by the applicable Creative Commons License

Verati, C., Mazabraud, Y., Lardeaux, J., Corsini, M., Schneider, D., Voitus, E., & Zami, F. (2016). Tectonic evolution of Les Saintes archipelago (Guadeloupe, French west Indies): Relation with the lesser Antilles arc system. *Bulletin de la Societe Geologique de France*, *187*(1), 3–10. https://doi.org/10.2113/gssgfbull.187.1.3

Verati, C., Patrier-Mas, P., Lardeaux, J., & Bouchot, V. (2014). Timing of geothermal activity in an active island-arc volcanic setting: First $^{40}Ar/^{39}Ar$ dating from Bouillante geothermal field (Guadeloupe, French West Indies). In F. Jourdan, D. Mark, & C. Verati (Eds.), *Advances in $^{40}Ar/^{39}Ar$ dating: From archeology to planetary Sciences* (pp. 285–295). Geological Society.

Violay, M., Gibert, B., Mainprice, D., Evans, B., Dautria, J., Azais, P., & Pezard, P. (2012). An experimental study of the brittle-ductile transition of basalt at oceanic crust pressure and temperature conditions. *Journal of Geophysical Research*, *117*(B3), B03213. https://doi.org/10.1029/2011JB008884

Violay, M., Giorgetti, C., Cornelio, C., Aeschiman, F., Di Stefano, G., Gastaldo, L., & Wiemer, S. (2021). HighSTEPS: A high strain temperature pressure and speed apparatus to study earthquake mechanics. *Rock Mechanics and Rock Engineering*, *54*(4), 2039–2052. https://doi.org/10.1007/s00603-021-02362-w

Volpe, G., Collettini, C., Taddeucci, J., Marone, C., & Pozzi, G. (2024). Frictional instabilities in clay illuminate the origin of slow earthquakes. *Science Advances*, *10*(26). https://doi.org/10.1126/sciadv.adn0869

Volpe, G., Pozzi, G., & Collettini, C. (2022). Y-B-P-R or S-C-C'? Suggestion for the nomenclature of experimental brittle fault fabric in phyllosilicate-granular mixtures. *Journal of Structural Geology*, *165*, 104743. https://doi.org/10.1016/j.jsg.2022.104743

Walkey, W., & Swanberg, C. (1990). Newberry Volcano, Oregon: New data supports conceptual hydrologic model. *Geothermal Resources Council - Transactions*, *14*, 743–748.

Wang, J., Jung, W., Li, Y., & Ghassemi, A. (2016). Geomechanical characterization of newberry tuff. *Geothermics*, *63*, 74–96. https://doi.org/10.1016/j.geothermics.2016.01.016

Wileveau, Y., Cornet, F., Desroches, J., & Blumling, P. (2007). Complete in situ stress determination in an argillite sedimentary formation. *Physics and Chemistry of the Earth*, *32*(8–14), 866–878. https://doi.org/10.1016/j.pce.2006.03.018

Wong, I., Pezzopane, S., Dober, M., & Terra, F. (2010). Evaluations of induced seismicity/seismic hazards and risk for the Newberry Volcano EGS Demonstration.

Wyering, L., Villeneuve, M., Wallis, I., Siratovich, P., Kennedy, B., Gravley, D., & Cant, J. (2014). Mechanical and physical properties of hydrothermally altered rocks, Taupo Volcanic Zone, New Zealand. *Journal of Volcanology and Geothermal Research*, *288*, 76–93. https://doi.org/10.1016/j.jvolgeores.2014.10.008

Yagupsky, D., Barcelona, H., Vigide, N., & Lossada, A. (2023). Effects of structural zonation on fluids circulation of the Copahue geothermal system. *Journal of South American Earth Sciences*, *125*, 104310. https://doi.org/10.1016/j.jsames.2023.104310

Yamaya, Y., Alanis, P., Takeuchi, A., Cordon, J., Mogi, T., Hashimoto, T., et al. (2013). A large hydrothermal reservoir beneath taal volcano (Philippines) revealed by magnetotelluric resistivity survey: 2D resistivity modeling. *Bulletin of Volcanology*, *75*(7), 729. https://doi.org/10.1007/s00445-013-0729-y

Zaiss, R. (2014). *Project NumeriSud SPHAERA-GEO, Géoréférencement et mosaïquage des cartes de l'IRD*. Bondy.

Zhang, F., Huang, R., An, M., Min, K., Elsworth, D., Hofmann, H., & Wang, X. (2022). Competing controls on effective stress variation and chloritization on friction and stability of faults in granite: Implications for seismicity triggered by fluid injection. *Journal of Geophysical Research: Solid Earth*, *127*(8), e2022JB024310. https://doi.org/10.1029/2022JB024310

Zoback, M., & Townend, J. (2001). Implications of hydrostatic pore pressures and high crustal strength for the deformation of intraplate lithosphere. *Tectonophysics*, *336*(1–4), 19–30. https://doi.org/10.1016/S0040-1951(01)00091-9

Zoback, M., Townend, J., & Grollimund, B. (2002). Steady-state failure equilibrium and deformation of intraplate lithosphere. *International Geology Review*, *44*(5), 383–401. https://doi.org/10.2747/0020-6814.44.5.383

21699356, 2025, 2, Downloaded from https://agupubs.onlinelibrary.wiley.com/doi/10.1029/2024JB030213 by Cochrane France, Wiley Online Library on [28/01/2025]. See the Terms and Conditions (https://onlinelibrary.wiley.com/terms-and-conditions) on Wiley Online Library for rules of use; OA articles are governed by the applicable Creative Commons License